Shape Coexistence in the Highly Neutron-Deficient Nuclei ^{175}Au and ^{179}Au.

PhD thesis

Thesis submitted in accordance with the requirements of the University of Liverpool for the degree of Doctor in Philosophy.

Faye Patricia Wearing

Acknowledgements

I would like to thank my supervisor Prof. David Joss for allowing me to work on such an interesting project and for all the words of encouragement along the way. Thank you also to my secondary supervisor Prof. Robert Page for always having the time to chat when I needed an opinion or explanation, not only during my PhD but throughout my degree.

Thank you to the STFC for providing funding without which this work could not have been completed. Thanks also to all of the collaborators in this work who helped with the experiments, and who offered advice during the analysis. Also, thank you to the physics staff at the University of Jyväskylä for ensuring the experiments ran smoothly and who were always happy to answer my many questions about the apparatus.

Thanks to Dr. Amina Patel for being an amazing friend, constantly making me laugh and making some of the tough times easier. Thank you for all of the great conversations and for eating all of the desserts with me. Thanks to Dr. Alex Gredley for your company, critical eye for catching mistakes, and willingness to go for a pint, especially when we were away on experiments.

I would also like to thank those in the Oliver Lodge who made my time in the office what it was. Thanks especially to Emily Higgins, Lucy McAreavey, Calvin Wraith, Dr. Kārlis Dreimanis and Dr. Samantha Colosimo who all helped to make the office a great place to be.

Thank you to Flynn for putting up with me throughout my PhD and especially towards the end for looking after me when I was so focussed on thesis writing. You kept me sane and I couldn't have done it without you.

Finally, thank you to my mum and dad for your unwavering support, I owe all I have achieved to you. Your belief in me has known no bounds and I am so thankful.

Abstract

Excited states in neutron-deficient isotopes ^{179}Au and ^{175}Au have been populated following ^{100}Ru(^{82}Kr,$p2n$) and ^{92}Mo(^{86}Sr,$p2n$) fusion evaporation reactions, respectively. Both experiments were performed at the University of Jyväskylä Accelerator Laboratory. γ-rays detected in the JUROGAM and GREAT germanium detectors were correlated with the isotopes of interest via their characteristic α-decays following a recoil implantation in the GREAT DSSD detector.

Four collective structures have been identified comprising approximately 40 γ rays. These have been unambiguously assigned to the decay of ^{175}Au considerably extending the previously reported level scheme. Specifically these γ rays have been interpreted to decay into the known isomeric α-decaying state of ^{175}Au. The structures have been interpreted in terms of proton-hole and proton-intruder configurations. Nine new γ rays associated with the ground-state α decay of ^{175}Au have been identified via a correlation with ^{171}Ir, the daughter of ^{175}Au.

Approximately 30 γ rays have been assigned to ^{179}Au confirming previous studies on this nucleus. The γ rays have been ordered into four collective bands and their structure has been interpreted as $\pi i_{13/2}$, $\pi h_{9/2}$ and $\pi f_{7/2} \otimes h_{9/2}$ prolate configurations. Additionally two new γ rays associated with ^{179}Au have been identified and are observed to decay from an isomeric state.

Contents

Chapter 1

Introduction

The nucleus is an ensemble of strongly interacting protons and neutrons. Its properties arise from the interplay of single-particle degrees of freedom and collective excitations arising from the interactions of many (or all) nucleons. It is a goal of nuclear theories to provide a unified means of predicting observable properties, however such a complicated system makes developing such theories challenging and essentially requires a solution the nuclear many-body problem.

Attempts have been made to describe the nucleus analytically using *ab initio* approaches that calculate nuclear properties from the nucleon-nucleon interaction. However, due to the considerable computing power needed for the *ab initio* method, it has so far only been successful in describing nuclei up to $A \approx 40$. An alternative approach assumes that a nucleon moves in a mean field potential assuming an effective interaction. This potential can be used in the Schrödinger equation $\hat{H}(\psi) = E(\psi)$ to predict nuclear energy levels. An experimental approach to understanding the nucleus is to measure the decay properties of the nuclear energy levels to provide a means of constraint on the form of the mean field potential.

Nuclear theories can be tested by measuring nuclear properties such as the

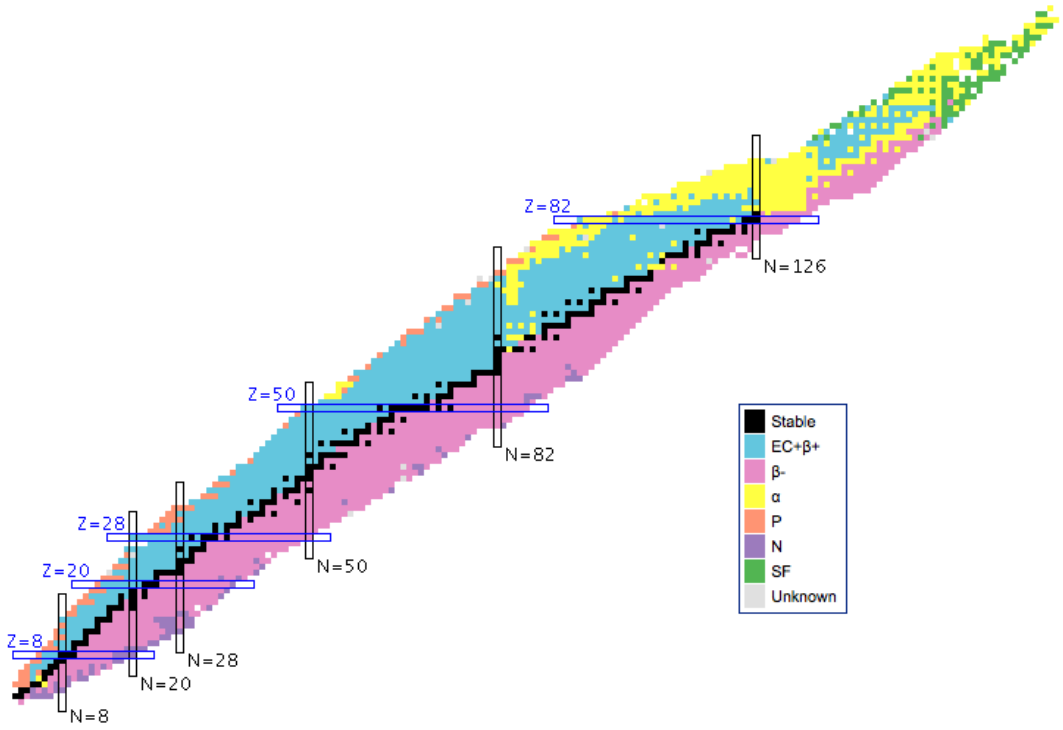

Figure 1.1: The complete Segré chart.

excitation energy and angular momentum, and observing how these vary as a function of proton and neutron number. This can be achieved by investigating the approximately 300 stable nuclei, which can occur in nature and the several thousand more that can be synthesised in an accelerator laboratory. Figure 1.1 illustrates all known proton and neutron combinations where those in black are stable. Figure 1.1 also indicates the locations of the closed shells or magic numbers. Single-particle excitations dominate spectra in nuclei near closed shells while collective behaviour between valence nucleons dominates near midshell regions. However, single-particle and collective degrees of freedom cannot be completely decoupled from each other and the arrangement of nucleons amongst orbitals can lead to the coexistence of collective bands based on different underlying deformations in the same nucleus.

The nuclei in the mass region near $Z = 82$ are an ideal testing ground

to examine the interplay between single-particle and collective motion. Shape coexistence was first identified by measuring sudden changes in charge distribution in ^{185}Hg and ^{187}Hg using optical hyperfine spectroscopy [1]. Following this, in-beam experiments confirmed excited 0^+ states in the even-mass $180 \leqslant A \leqslant 190$ Hg isotopes which have been interpreted in terms of weakly deformed oblate ground states and prolate deformed intruder configurations [2]. The intruder states are based on proton-pair excitations across the $Z = 82$ shell gap. Recent Coulomb excitation measurements using accelerated radioactive ion beams have confirmed the character of the coexisting states [3].

Nuclei in this region have proton numbers close to the $Z = 82$ shell closure while the neutron numbers tend to be near to the neutron midshell. Thus the stabilising effects of the proton shell structure that promote spherical symmetry compete against increases in correlation energy due to the residual interactions between neutrons, which favour deformed shapes. These two effects can give rise to shape coexistence, a phenomenon where a nucleus exhibits several shape configurations at low-excitation energy. Identifying the various shape structures within a nucleus can give single-particle information and can also provide an insight into the collective motion of the nucleus.

The excitation energies of intruder structures in even-Z nuclei have been observed to vary smoothly as a parabola with varying mass number. One way to probe such changes is to examine odd-Z nuclei which are expected to have coexisting structures based on proton-intruder and proton-hole excitations coupled to Pt and Hg cores, respectively. Studying these neutron-deficient nuclei presents challenges since the parabolas mentioned cross the point at which the proton separation energy changes sign and the nucleus becomes proton unbound. Nuclei at the limits of stability are also produced with low cross sections, usually along with high amounts of background radiation arising from

fission and higher cross section fusion-evaporation products. Recoil-decay tagging (RDT) can be employed as a means of separating the nuclei of interest from unwanted background radiation [43]. The efficiency of RDT for background suppression can be seen in recent work on ^{177}Au where a variety of structures were observed from proton-intruder and proton-hole type excitation [56].

This thesis is concerned with Au ($Z = 79$) nuclei, which are close to the $Z = 82$ proton shell closure and near the neutron midshell at $N = 104$. This work presents new data for the neutron-deficient gold nuclei ^{175}Au and ^{179}Au. The Au isotopes can be considered as a proton coupled to a Pt core or hole states coupled to a Hg core. Both nuclei studied in this work have an odd proton which can be rearranged into orbitals $s_{1/2}$, $d_{3/2}$, and $h_{11/2}$ orbitals below the shell gap and the $h_{9/2}$, $f_{7/2}$, and $i_{13/2}$ intruder orbitals above. This work aims to understand the relative excitation energies of these states in order to constrain nuclear models incorporating mean field potentials.

The experiments were carried out at the University of Jyväskylä Accelerator Laboratory where the JUROGAM array was coupled with the RITU gas-filled separator and the GREAT focal plane spectrometer. This complex set-up allows for high selectivity of the data. The techniques employed to select data are detailed in this work. This analysis has allowed an extension of the ^{175}Au level scheme to include four new collective band structures associated with the $h_{11/2}$ isomer. Ground-state decays were also identified for ^{175}Au via a mother-daughter correlation method, which led to the potential discovery of a new ^{171}Ir α decay. This work also reports the discovery of γ rays depopulating a new isomeric state in ^{179}Au.

Chapter 2

Nuclear Theory

The atomic nucleus is a unique arrangement of strongly interacting fermions, which form a complex system of which there is an incomplete understanding. Nucleons interact strongly with their nearest neighbours but weakly with those at a greater distance than ≈1 fm. These complexities arise because the nucleus is a many-body system that can comprise hundreds of nucleons rendering it impossible to accurately describe heavy nuclei analytically. The computational power needed to calculate the interactions between all nucleons is far greater than anything available today. However it is the interactions between a nucleus' protons and neutrons that are the basis for its measurable properties.

The best workable solution has been to develop nuclear models which describe observed phenomena as closely as possible. Most of these models were developed by examining the behaviour of nuclei close to the line of stability, however advances in detector technology have provided an ideal testing ground for the models in the form of nuclei far from stability.

Exotic nuclei make for an ideal testing ground to vigorously test nuclear models because they are so far from the stable isotopes on which the models were built. Nuclei close to the drip lines are often produced with large amounts

of deformation; an ideal setting for new phenomena to occur.

2.1 Nuclear Models

With the current limits on computational power, the only way to understand the nuclear many-body problem is to rely on nuclear models to describe experimental observations and to use these models to make predictions about nuclei that are not yet well understood. Two of these models are described in the following sections.

2.1.1 Liquid Drop Model

The Liquid Drop Model (LDM) is the first theoretical model which has been able to describe nuclear properties and has its basis in the analogous description of a charged drop of incompressible nuclear matter. It was introduced in 1937, and was the first semi-classical macroscopic model describing the atomic nucleus.

The idea first came about when the nucleus was observed to exhibit a saturation of nuclear forces, for example in the binding energy per nucleon as a function of mass number [4]. If every particle in the nucleus interacts with every other, then the binding energy per nucleon would be approximately proportional to the square of the number of nucleons present in the nucleus, however the value peaks at around iron, and then starts to decrease gradually towards uranium. The formations of the LDM enabled development of the semi-empirical mass formula [5][6], which expresses the binding energy in terms of the geometry, charge and quantum effects such that

$$B_E(A,Z) = a_v A - a_s A^{\frac{2}{3}} - a_c Z^2 A^{-\frac{1}{3}} - a_i (A-2Z)^2 A^{-1} \pm \delta, \tag{2.1}$$

where coefficients a_v, a_s, a_c and a_i are related to volume, surface, Coulomb and asymmetry, respectively. The pairing term is denoted as δ and can take a positive, zero or negative value for even-even, odd-even and odd-odd nuclei, respectively.

The LDM does a good job of describing bulk nuclear properties, however it does not predict the structure of some especially well-bound nuclei. It is observed experimentally that nuclei with certain neutron and proton numbers (2,8,20,28,50,82) have a higher binding energy per nucleon than expected. These neutron and proton numbers are known as magic numbers. The LDM cannot explain these features nor the existence of superheavy nuclei but it does hint at an underlying shell structure.

2.1.2 Shell Model

During the 1940's, many unexplained features of nuclei were observed including relative isotopic abundances, proton and neutron separation energies and absorption cross section among other things. It was also observed that at particular proton and neutron numbers, there are decreases in the experimentally observed masses compared with the expectations from fitting bulk properties. The evidence available pointed not only to independent particle motion within the nucleus but also to the nucleus exhibiting a shell structure analogous to atomic structure with certain numbers of nucleons being especially stable and referred to as magic. [8]

A shell model to explain nuclei was ideal given the success such a model

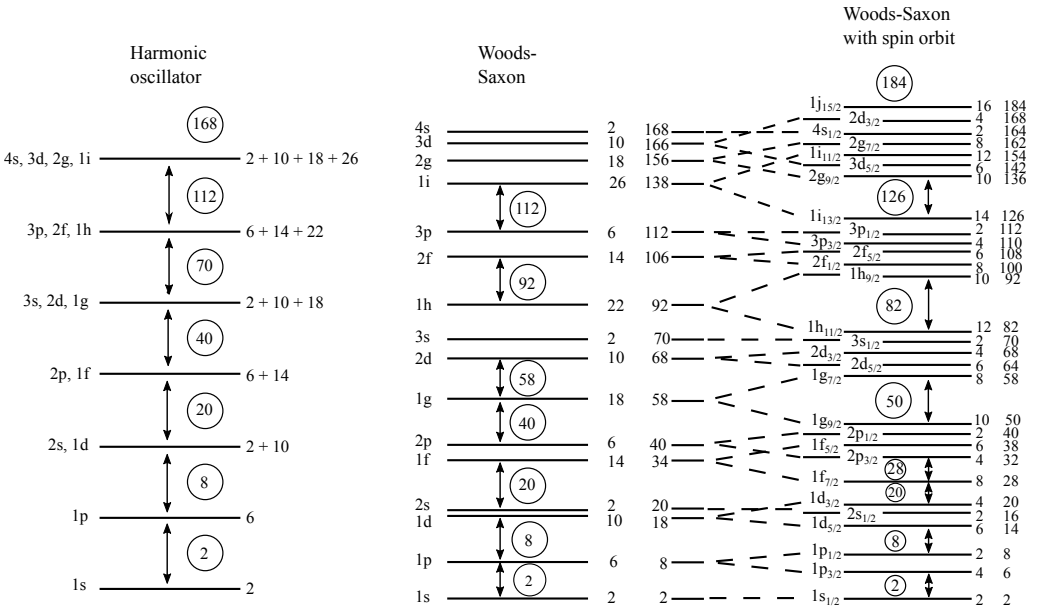

Figure 2.1: Schematic recreated from Ref. [7] showing the energy levels calculated using three different potentials: harmonic oscillator, Woods-Saxon and Woods-Saxon with added spin orbit term. The capacity of each level of the Woods-Saxon with spin-orbit term is indicated to its right, with a cumulative total of nucleons to the far right. The large gaps between some shells are interpreted as closed shells or magic numbers. The right side of the diagram shows the effect of the spin-orbit interaction which splits levels with $l > 0$ into two.

had explaining atomic features; this type of model allows one to simplify the nucleus to a core plus a number of valence nucleons. The nuclear shell model was developed independently by Mayer [9], and Haxel *et.al* [10] in the late 1940s. The model is based on a mean field where only the interactions of the valence nucleons are considered, the remainder nucleons which make up the core are approximated to a single averaged potential $V(r)$. This reduces the core from a many body problem to an effective one-body problem.

It can be harder to imagine nucleons confined to orbitals within the tiny nucleus than it is to imagine electrons arranged in orbitals in the much larger space outside of the nucleus. Nucleons are large compared to electrons and are confined in a much smaller space. However, consider a collision between two

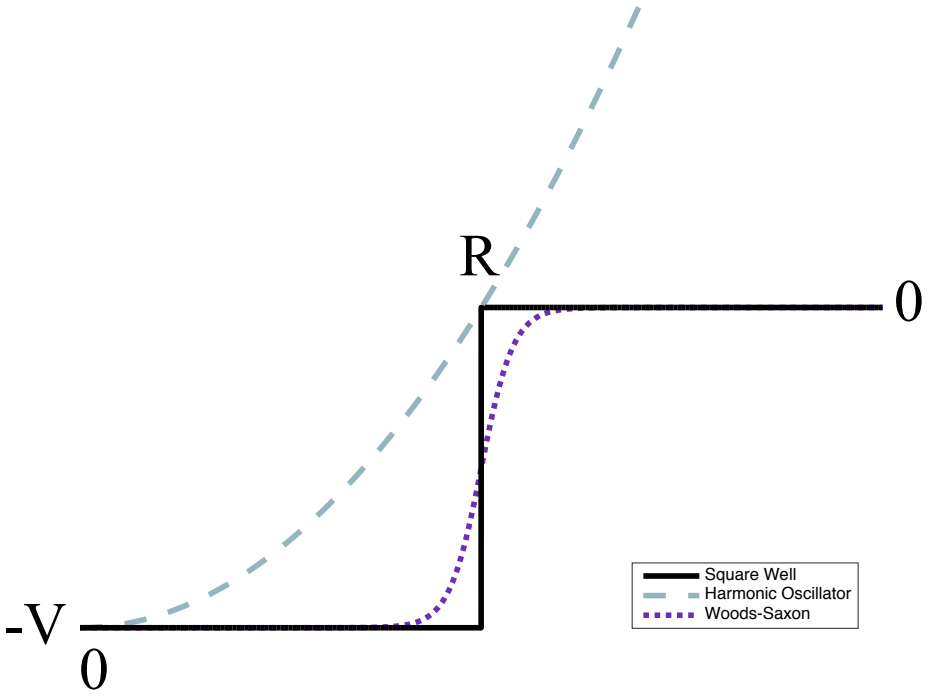

Figure 2.2: A comparison of the potential wells as described in text. Shown are the square well, harmonic oscillator and Woods-Saxon potentials.

nucleons at the bottom of a potential well. The energy transferred during the collision would not be sufficient to free either particle from the well and there are no available states in which to scatter into above the level at which they are constrained. This is due to the Pauli exclusion principle which forbids two or more identical fermions from occupying the same quantum state within a system. Therefore the collision cannot occur and the nucleons can share an orbit [7].

The first step in developing the shell model was the choice of potential; it must recreate the magic numbers observed experimentally and is therefore of great importance. Three commonly considered potentials are the square-well, harmonic oscillator and Woods-Saxon potentials which can be compared in figure 2.2.

The square well potential is defined as

$$V(r) = \begin{cases} V_0 & r \leqslant R \\ 0 & r > R \end{cases} \tag{2.2}$$

where r is the distance from the centre of the nucleus, R is the radius of the nucleus and V_0 is the depth of the well. This potential is only able to recreate the first two magic numbers. The flat bottom of the square well, seen in figure 2.2, represents the short range of the nuclear force fairly well, however the sharp corners do not adequately describe the interactions at the nuclear surface.

Consider the harmonic oscillator potential, defined as

$$V(r) = \begin{cases} -V_0[1 - (\frac{r}{R})^2] & r \leqslant R \\ 0 & r > R \end{cases} \tag{2.3}$$

Here the sharp edges of the square well are replaced with smoothly varying edges, which gives a more realistic description of the nuclear surface and so is an improvement on the square well potential, reproducing the first three magic numbers. However the gradually increasing potential from the nuclear centre looks more like a long range rather than a short range force like the strong force. The harmonic oscillator potential implies that all nucleons would be attracted to the centre of the nucleus, which is not the case. Neither of these potentials are good enough to model heavier nuclei and so some improvements must be made. The Woods-Saxon is an example of an improved potential and is defined as

$$V(r) = \frac{-V_0}{1 + \exp[\frac{r-R}{a}]}, \tag{2.4}$$

where a is the surface diffuseness term [11]. This potential has a flat base similar to the square well potential, seen in figure 2.2, which is accurate in

describing the uniform short range force that acts on all nucleons which are not at the surface. Those at the surface feel less attraction due to the decreased number of nuclei surrounding them, which is reflected in the curved corners of the harmonic oscillator potential. As with the harmonic oscillator, the Woods-Saxon potential is able to reproduce the first three magic numbers only, and so further modifications are needed.

It was found that the introduction of a spin-orbit coupling term could successfully recreate the proper separation of the subshells and appearance of magic numbers [10]. The spin-orbit modification can be written as

$$V(r) \Rightarrow V(r) + V_{so}(r)\vec{l} \cdot \vec{s}, \tag{2.5}$$

where $V_{so}(r)$ is the strength of the spin-orbit interaction, l is the orbital angular momentum and s is the spin quantum number. The coupling leads to a term for total angular momentum of $j = l \pm \frac{1}{2}$. The effect of this term in recreating experimentally observed shell levels is shown in figure 2.1.

2.2 Deformation and Rotation

Nuclear structure is largely described in terms of the single-particle and collective motions of the nucleus. Collective motion is based on the liquid drop model and treats the nucleus as approximately spherical and of uniform density. It encompasses mass nuclear effects such as deformation, rotation and vibration. Single-particle motion can be described by the shell model, but only includes particles near to the Fermi surface which are all thought of as independent of each other. Current nuclear structure physics aims to consolidate these two ideas by understanding how the interplay between the collective and single-particle motion leads to the effects observed experimentally.

2.2.1 Nuclear Deformation

Nuclei are spherical at and around closed shells, however when a nucleus has valence nucleons outside a closed shell, there is an increase in correlation energy due to the residual interactions between valence nucleons. The correlation energy increase drives the nucleus to deformation, which relieves the degeneracy of the shell model states and the nucleus adopts ellipsoidal shapes rather than spherical.

The nuclear surface may be described generally in spherical harmonics with time-dependent shape parameters as coefficients by the following expansion

$$R(\theta,\phi) = C(\alpha_{\lambda\mu})R_0\left[1+\sum_{\lambda=0}^{\infty}\sum_{\mu=-\lambda}^{\lambda}\alpha_{\lambda\mu}Y_{\lambda}^{\mu}(\theta,\phi)\right], \tag{2.6}$$

where R_0 is the radius of a sphere and is equal to $r_0A^{\frac{1}{3}}$ where A is the mass number and r_0 is determined to be approximately 1.20 fm. The coefficient $C(\alpha_{\lambda\mu})$ ensures the nucleus has a constant volume and $\alpha_{\lambda\mu}$ are the Hill-Wheeler coordinates, which describe distortion from a spherical shape. The multipolarity of the deformation is described by λ and μ is an integer indicating the order of the expansion, μ can have a range of $-\lambda$ to λ. The expansion and contraction of the nuclear surface are represented by $\lambda = 0$ and $\lambda = 1$, and $\lambda = 2, 3, 4$ correspond to quadrupole, octupole and hexadecapole deformations, respectively.

For axially symmetric nuclei equation 2.6 may be expanded to

$$R(\theta) = CR_0\left[1+\sqrt{\frac{5}{4\pi}}\beta_2P_2(cos\theta)+\sqrt{\frac{9}{4\pi}}\beta_4P_4(cos\theta)\right] \tag{2.7}$$

where $P_2(cos\theta)$ and $P_4(cos\theta)$ are Legendre polynomials and β_2 and β_4 are quadrupole deformation parameters, which are related to the Hill-Wheeler

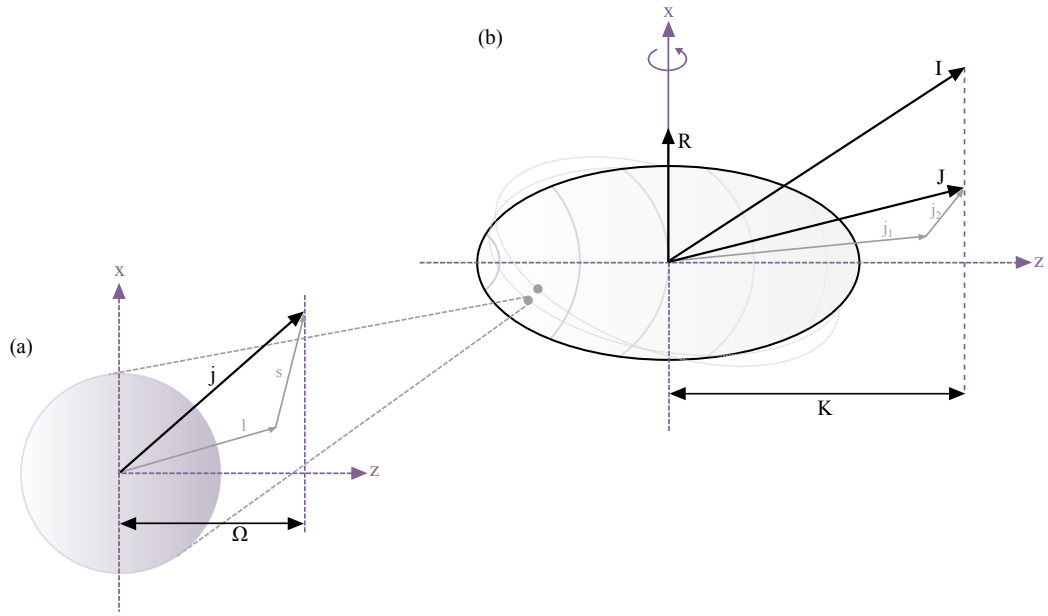

Figure 2.3: A schematic illustration of a nucleus and it's valence nucleons. (a) shows an example of a valence nucleon and how its total angular momentum j is the vector sum of its orbital angular momentum l and intrinsic spin s. (b) shows how the valence nucleon fits in with the rest of the nucleus and how the individual j components from valence nuclei, in addition to the angular momentum of the core R, impact upon the total angular momentum of the nucleus and hence the projection onto the symmetry axis K.

coordinates.

2.2.2 Nuclear Rotation

The components involved in the spin of a nucleus can be understood by thinking of the nucleus as a core with valence nucleons orbiting around it. The valence nucleons have a total angular momentum j equal to the vector sum of the single-particle intrinsic spin s, and the orbital angular momentum l, schematically represented in figure 2.3. Also shown in figure 2.3 is how the valence nucleons interact with the core to affect the total angular momentum of the nucleus. The total angular momentum of the nucleus is found by vectorially summing the angular momentum of the rotating core R to the sum of

the total angular momenta of the valence nucleons J, where $J = \sum_i j_i$. K is the sum of the individual single-particle projections, Ω, on the symmetry axis. If a nucleus has a large K value, i.e. a large projection onto the symmetry axis, it is said to be deformation aligned. A small value of K means that the nucleus is rotation aligned.

The expression relating the angular momentum and energy of a rotating axially deformed nucleus is

$$E_{rot}(I) = \frac{\hbar^2}{2\Im^0} I(I+1), \tag{2.8}$$

where $\Im^0$ is the nuclear moment of inertia, which is constant in a perfect rigid rotor but should vary slowly within rotational bands in nuclei [12]. Equation 2.8 exemplifies how the rotational excitation energies increase proportionally to $I(I+1)$.

2.2.3 Deformed Shell Model

The shell model works well to describe nuclei at or near to a closed shell using a spherical potential, however most nuclei are not near a closed shell and therefore are anticipated to have some level of deformation. A new potential was therefore needed for deformed nuclei. The Nilsson model was introduced in 1955 by Sven G. Nilsson which is a modified harmonic oscillator potential [13]. In this model, the energy of the single particle is calculated and plotted as a function of quadrupole deformation. An example of this for protons in the $Z = 82$ region is shown in figure 2.4 and is known as a Nilsson diagram. The conventional way to label Nilsson orbitals is

$$\Omega^{\pi} \left[N n_z \Lambda \right], \tag{2.9}$$

where Ω is the projection of total angular momentum of the nucleon onto the symmetry axis as shown in figure 2.3, π is the parity of the state, N is the principal quantum number, n_z is the number of nodes in the wavefunction in the z-direction and Λ is the projection of the orbital angular momentum onto the symmetry axis. Each Nilsson orbital may be occupied by two degenerate nucleons in time-reversed orbits of projections $\pm\Omega$.

As a consequence of the Pauli Exclusion Principle, it is forbidden for two states with the same quantum numbers to cross. The states can come together but as they get closer they repel each other. The point at which they would have crossed is known as the inflection point and a substantial amount of wavefunction mixing happens at this point. For prolate shapes ($\epsilon_2 > 0$), the low-Ω projections have the largest overlap with the core and are lowered in energy. For oblate shapes ($\epsilon_2 < 0$), the opposite is true. Orbitals with high-j are lowered by the spin-orbit interaction and so can intrude into the shell below. These are often referred to as intruder states and will be discussed in more detail in the following section.

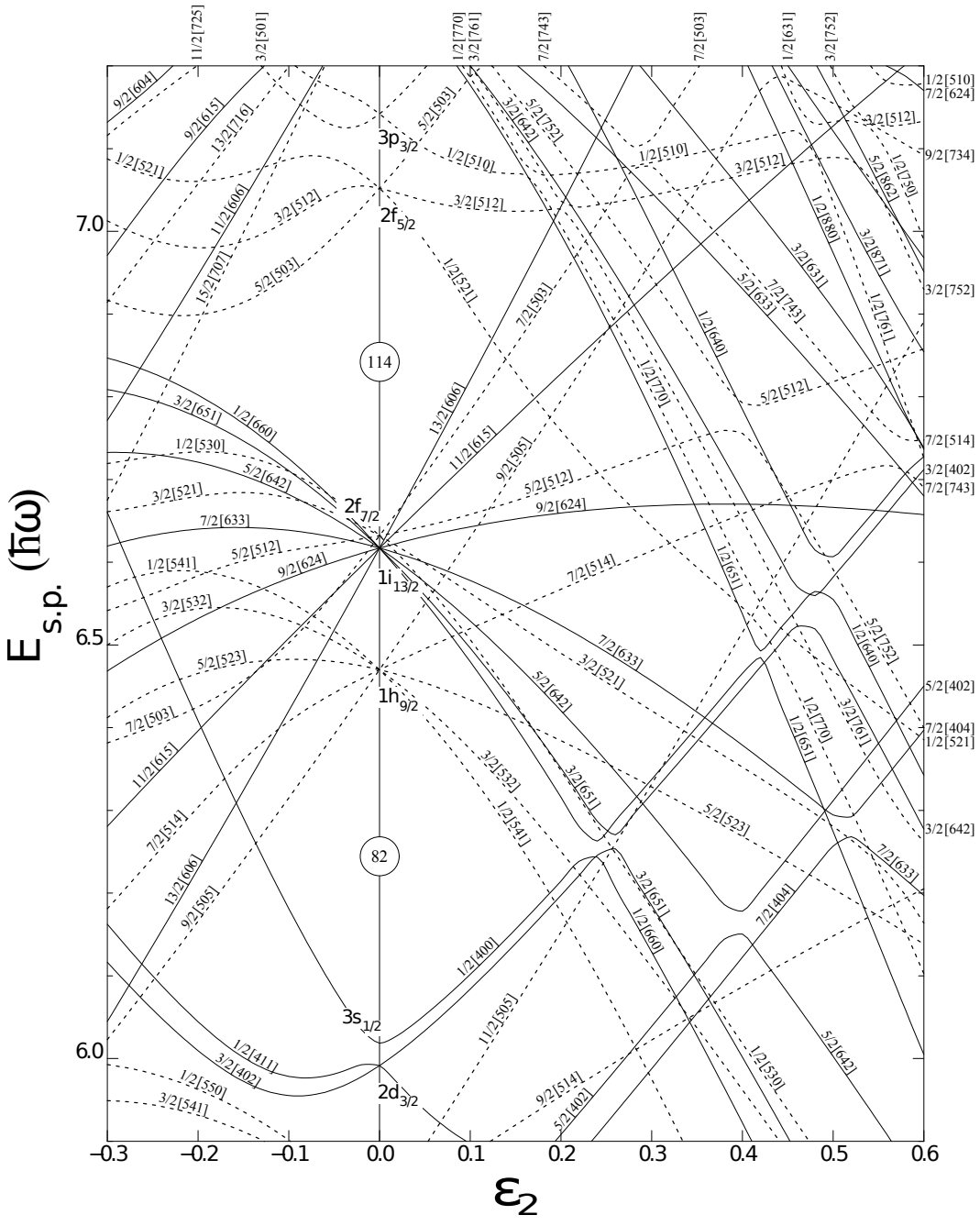

Figure 2.4: A Nilsson diagram showing single-proton states in the $Z = 82$ region. The diagram shows how the single-particle energy changes with quadrupole deformation ϵ_2 and as such, relieves the degeneracy of the spherical shell model states.

2.3 Shape Coexistence and Intruder States

Shape coexistence can be described as the ability of a nucleus to exhibit several different deformations within a very narrow range of excitation energies. The phenomenon has been of vital importance in explaining the origin of multiple deformed configurations observed in nuclei near the $Z = 82$ shell gap. Shape coexistence is a phenomenon that has been firmly established in even-Z nuclei around the Z = 82 shell gap and the neutron midshell, N = 104. Shape coexistence was first observed in this region in 1972 in Hg isotopes by hyperfine spectroscopic measurements [1]. These measurements revealed a large isotope shift in nuclei such as Pb [14][15], Hg [1][3], Pt [16] and Os [17][18].

The effect has been theorised to arise from the interplay between two opposing effects, the first of which is the stabilising effect of nearby closed shells and subshells, which encourages the spherical nuclear shape and increases the cost in energy to redistribute protons and neutrons into an excited state. The residual interactions between protons and neutrons act in opposition to this tendency, which results in an increase in correlation energy and that drives the nucleus into a deformed shape. [2]

The deformed shapes can be interpreted as being built upon intruder states, which arise as the result of a particle-hole excitations across a shell gap. The basic assumption underlying this interpretation of shape coexistence is that the nucleons are considered to form an approximately spherical core with fully occupied shells and sub shells. The nucleons that are surplus to those needed to form a closed shell are considered to orbit the nucleus independently due to the field generated by the core nucleons.

2.4 Electromagnetic Transitions

Heavy-ion fusion evaporation reactions can produce nuclei in highly excited states with huge amounts of angular momenta that must be removed. There are two electromagnetic processes which can de-excite nuclei; γ-ray emission and internal conversion, both detailed below.

2.4.1 γ-ray Transitions

Gamma rays are a valuable probe into the structure of the nucleus. They have energies of the order 0.1-10 MeV. Since the energy of the recoiling nucleus is assumed to be negligible, the γ-ray energy can be taken as indicative of the energy difference between nuclear states such that

$$E_\gamma = E_i - E_f, \tag{2.10}$$

where E_i and E_f are the energies of the initial and final states, respectively. An excited nucleus with angular momentum I and parity π may decay from an initial state I_i^π to a final state I_f^π by emission of a γ ray. The decay must adhere to angular momentum conservation such that

$$\vec{L} = \vec{I_i} - \vec{I_f}, \tag{2.11}$$

where $\vec{I_i}$ and $\vec{I_f}$ are the angular momentum of the initial and final states and $\vec{L}$ is the angular momentum removed by the γ-ray transition (also called the multipolarity). Since $\vec{L}$, $\vec{I_i}$ and $\vec{I_f}$ must form a closed vector triangle, there are limited values that $\vec{L}$ is able to take. Consequently the angular momentum available to the γ ray is restricted by selection rule

$$|I_i - I_f| \leqslant L \leqslant I_i + I_f. \tag{2.12}$$

Moreover, parity must be conserved leading to further selection rules

$$\Delta\pi(ML) = (-1)^{L+1}, \tag{2.13}$$

$$\Delta\pi(EL) = (-1)^{L}, \tag{2.14}$$

where

$$\begin{aligned} \Delta\pi &= 1 = no, \\ \Delta\pi &= -1 = yes, \end{aligned} \tag{2.15}$$

and where M and E represent magnetic and electric transitions, respectively. It can be seen from equations 2.13 and 2.14 that $E1, M2, E3, M4, ...$ multipolarity transitions result in a parity change, while $M1, E2, M3, E4, ...$ do not. Although for one decay there may be many transitions of different multipolarities available to a γ ray, the lower multipole orders are generally favoured due to their larger transition probabilities.

Theoretical lifetimes of γ-decaying states have been approximated by Weisskopf [19] based on the assumption that the cause of the γ radiation is a transition of one single proton moving independently between levels within a spherical, hard-edged nucleus. Weisskopf defined the total transition probability as

$$T^{\sigma L}_{i\to f} = \frac{8\pi}{\hbar}\frac{L+1}{L[(2L+1)!!]^2}\left(\frac{E_\gamma}{\hbar c}\right)^{2L+1} B(\sigma L; I_i \to I_f), \tag{2.16}$$

where σ denotes magnetic or electric character, and $B(\sigma L; I_i \to I_f)$ is the reduced transition probability, defined as

L	T_{el}(s)	T_{mag}(s)
1	$6.73A^{-2/3}E_{\gamma}^{-3} \times 10^{-14}$	$2.24A^{0}E_{\gamma}^{-3} \times 10^{-14}$
2	$9.37A^{4/3}E_{\gamma}^{-5} \times 10^{-9}$	$3.12A^{-2/3}E_{\gamma}^{-5} \times 10^{-8}$
3	$1.98A^{-2}E_{\gamma}^{-7} \times 10^{-2}$	$6.60A^{-4/3}E_{\gamma}^{-7} \times 10^{-2}$
4	$6.30A^{-8/3}E_{\gamma}^{-9} \times 10^{-4}$	$2.1A^{-2}E_{\gamma}^{-9} \times 10^{5}$
5	$2.83A^{-10/3}E_{\gamma}^{-11} \times 10^{11}$	$9.43A^{-8/3}E_{\gamma}^{-11} \times 10^{11}$

Table 2.1: Weisskopf estimates for the first five orders of multipolarity. Values taken from reference [20]. T_{el} and T_{mag} are the half-lives of electric and magnetic transitions, respectively. A is the mass number and E_{γ} is the γ-ray energy in MeV.

$$B(\sigma L; I_i \rightarrow I_f) = \frac{1}{2I_i + 1} \left| \langle I_f \left| M(\sigma L) \right| I_i \rangle \right|^2, \tag{2.17}$$

where $\left| \langle I_f \left| M(\sigma L) \right| I_i \rangle \right|^2$ is the reduced matrix element. The Weisskopf estimates for the first five orders of multipolarity are shown in table 2.1. The Weisskopf estimates have been somewhat useful in this work when attempting to constrain the multipolarities of γ rays based on their lifetimes.

2.4.2 Internal Conversion

In the electromagnetic decay of an excited nucleus, internal conversion can compete with γ-ray emission [21], and in the case of $0^+ \rightarrow 0^+$ transitions, internal conversion is the only possible mode of de-excitation since these E0 transitions cannot proceed by γ-ray emission. In this process the wavefunction of the nucleus overlaps with the wavefunction of an atomic electron resulting in a de-excitation of the nucleus via electron emission. The nuclear excitation energy E_{ex} is transferred directly to the orbital electron, which is then emitted with energy

$$E_{e^-} = E_{ex} - E_b, \tag{2.18}$$

where E_b is the binding energy of the electron's original shell. The binding energy value varies depending on the electronic orbital. The ejected electron leaves a vacancy which is subsequently filled by a higher energy electron leading to the emission of an X-ray. The ratio between the instances of internal conversion and γ-ray emission is known as the conversion coefficient and is defined by

$$\alpha = \frac{N_e}{N_\gamma}. \tag{2.19}$$

The conversion coefficient can give some information with regards to the multipolarity of the transition.

2.4.3 Electric Monopole (E0) Transitions

Electric monopole (E0) transitions are a particular type of internal conversion that take place between states of the same spin and parity ($I^\pi \rightarrow I^\pi$). These types of transitions do not carry any angular momentum. If a nucleus has configurations which vary in deformation, and they mix, one would expect to observe enhanced electric monopole transitions [22]. Therefore this type of transition is enhanced between states of different shapes and for this reason E0 transitions are particularly important in the study of shape coexistence.

2.5 α Decay

α decay is a radioactive decay process in which the parent nucleus decays via emission of a ^{4}He nucleus. The daughter is the name given to the resultant nucleus. Since its discovery, α decay has been widely used as a probe of nuclear structure. Spontaneous α emission can be represented by the following process

$$ {}^{A}_{Z}\mathrm{X}_{N} \rightarrow {}^{A-4}_{Z-2}\mathrm{X}'_{N-2} + \alpha + Q, \tag{2.20} $$

where X is the mother nucleus and X' is the daughter nucleus. For the α particle the intrinsic spins of each of the nucleons are cancelled out and the $1s$ shells for both protons and neutrons are fully occupied leading to a high binding energy per nucleon. This makes α emission a favourable decay mode as a way to lose as much kinetic energy with the smallest mass.

2.5.1 α-decay Q-value

To understand the α-decay process one must study the conservation of energy. Assuming that the mother nucleus is at rest the energy of the initial system is the rest energy $m_X c^2$. If the kinetic energy of the decay fragments are represented by E, then conservation of energy gives

$$ m_X c^2 = m_{X'} c^2 + E_{X'} + m_\alpha c^2 + E_\alpha. \tag{2.21} $$

Rearranging the above expression gives

$$ (m_X - m_{X'} - m_\alpha)c^2 = E_{X'} + E_\alpha, \tag{2.22} $$

where the right hand side of this expression is equal to the net energy released in the α emission, called the Q value. An α decay will only occur spontaneously in nature if $Q > 0$. If the mother nucleus is taken to be at rest before the α decay, then the conservation of linear momentum requires that the daughter and emitted α particle move with equal and opposite momentum such that

$$ p_\alpha = p_{X'}, \tag{2.23} $$

where p is the momentum. A typical α decay releases ≈ 5 MeV and so can be assumed to be non-relativistic. Therefore the kinetic energy in terms of the momentum can be written as

$$E = \frac{p^2}{2m}. \tag{2.24}$$

An equation for the energy of the α decay in terms of the Q value can be reached using equations 2.23 and 2.24 and the fact that $Q = E_{X'} + E_\alpha$ such that

$$E_\alpha = \frac{Q}{(1 + m_\alpha/m_{X'})}. \tag{2.25}$$

The mass ratio can be written as $4/(A-4)$, giving

$$E_\alpha = Q(1 - 4/A), \tag{2.26}$$

where A is the mass number of the daughter nucleus.

2.5.2 Theory of α Emission

Theories to explain of α emission were developed at almost the same time by Gamow [23] and Gurney and Condon [24] in 1928. The theory describes α emission in terms of quantum mechanics and assumes that the α particle is preformed within the nucleus. Figure 2.5 shows a potential well where R_0 is the radius of the nucleus and R_e is a classically permitted region outside of the nucleus. Between these two regions lies a potential barrier where the height of the barrier is greater than the energy of the α particle. At $r < R_0$, the α particle can move but not escape. The quantum mechanical explanation for α emission states that each time the α decay presents itself at the barrier there is

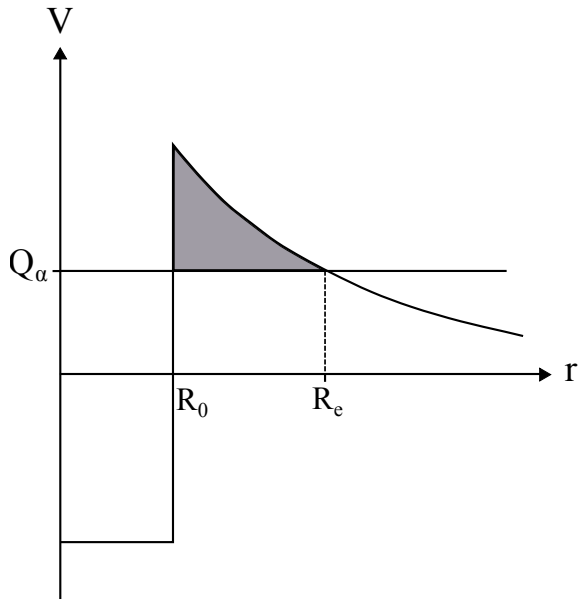

Figure 2.5: A schematic illustration of a Coulomb barrier. The potential energy felt by a particle is labelled as V, and is plotted as a function of r, the distance from the centre of the nucleus. R_0 represents the nuclear radius, and R_e the distance at which the α particle has escaped the nucleus. The shaded region represents the barrier through which the α particle must travel to escape.

a finite probability that it will quantum tunnel through it. The disintegration constant of an α-emitter can be expressed as

$$\lambda = fP, \tag{2.27}$$

where f is the frequency with which the α particle presents itself to the potential barrier and P is the probability of transmission through the barrier. The presence of the barrier prevents the α decay from happening immediately and leads to a half-life, which depends on the structure of the nucleus.

2.5.3 α-decay Selection Rules

The ^{4}He nucleus has two protons and two neutrons, which all occupy $1s$ states. The protons and neutons are paired with their spins coupled to zero, which

means the α particle carries a spin of zero. The total angular momentum carried away by an α particle is therefore purely orbital in character. The angular momentum and parity must be conserved during an α decay and so in a decay from initial state I_i to final state I_f

$$\vec{l} = \vec{I_i} - \vec{I_f}. \tag{2.28}$$

This leads to selection rules for α decays similar to those discussed earlier for γ decays. These can be expressed as

$$|I_i^{\pi_i} - I_f^{\pi_f}| \leqslant l \leqslant I_i^{\pi_i} + I_f^{\pi_f}, \tag{2.29}$$

where

$$\pi_f = \pi_i(-1)^l \quad \text{and} \quad \pi_i = (-1)^l. \tag{2.30}$$

Therefore α decays may only occur when the initial and final state have same parity and l is even, or when the initial and final state have different parity and l is odd.

Chapter 3

Experimental Apparatus

The two experiments reported in this thesis use data that were collected at the Accelerator Laboratory at the University of Jyväskylä. These data sets were collected with different target-position detector arrays - JUROGAM and SAGE. Both experiments used the RITU gas-filled separator and the GREAT focal-plane detection system. The spectrometer systems used in these experiments are capable of measuring many types of radiation and will be discussed in this chapter.

3.1 JUROGAM

The first experiment used the JUROGAM spectrometer array at the target position. JUROGAM comprises 43 EUROGAM-type [25] Compton-suppressed coaxial germanium detectors [26][27]. The detectors are arranged into six rings at angles of 157.6°, 133.57°, 107.94°, 94.16°, 85.84°and 72.05° with respect to the beam direction. The crystals are tapered over the front 3 cm of their length to reduce low electric field regions and are arranged in a honeycomb pattern.

The array is made up of two hemispheres that open to allow access to the target chamber. The target position is located at the focal point of the spectrometer array. If any γ ray scatters out of the detector and does not deposit its full energy in the germanium crystal it should be discarded. For this reason, all 43 detectors are equipped with a bismuth germanate (BGO) Compton-suppression shield, which are used to veto any γ ray that is in coincidence with both the BGO and the germanium crystal.

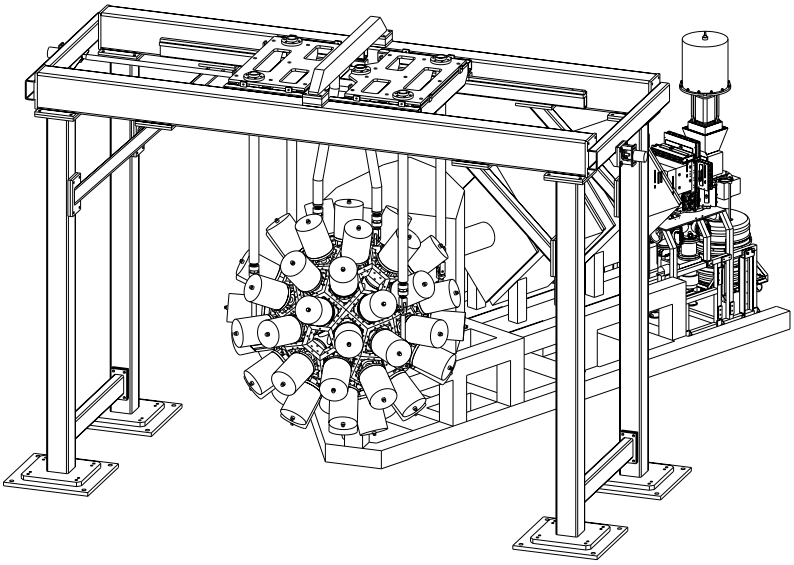

Figure 3.1: Line drawing of the JUROGAM array coupled to RITU and GREAT. The drawing shows the frame to which the detector array is mounted and which enables the 'ball' of detectors to be pulled apart in the middle to allow access to the target. Image courtesy of Dave Seddon.

3.2 SAGE Spectrometer

SAGE is an array of JUROGAM-type germanium detectors combined with an electron solenoid spectrometer. SAGE was commissioned at the beginning of 2010 [28] and was built to enable the simultaneous detection of γ rays and conversion electrons at the target position [29]. The ability to detect γ rays in conjunction with electrons means that there is the possibility to observe electric monopole (E0) transitions through the presence of conversion electrons in coincidence with γ-ray transitions. E0 transitions can be a signature of shape coexistence due to the increased likelihood of an E0 transition between two states with differing deformation. The ability to measure γ rays and electrons in coincidence also means that the conversion coefficients for decays can be measured [29].

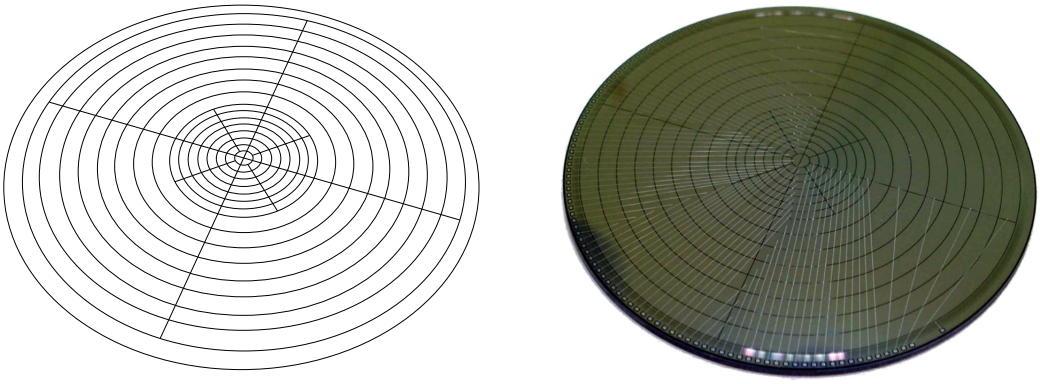

Figure 3.2: Left: A schematic illustrating the pixel layout of SAGE. Right: A photograph of the annular silicon detector within SAGE. The detector segmentation is visible in the photograph.

3.2.1 Conversion Electron Detection

In addition to the germanium array, SAGE also incorporates a small annular silicon detector. The detector is segmented into 90 individual pixels varying in size as shown in figure 3.2. It is 1 mm thick and has a diameter of 48 mm. Despite the highly segmented nature of the detector, its total active area is approximately 96% of the detector area [30].

The detector is located in a backward angle with respect to the beam direction. It is positioned 95.5 cm upstream of the target position and is offset from the beam axis at an angle of 3.2°. Figure 3.3 shows a simplified diagram of this orientation. Unlike germanium detectors, silicon detectors are sensitive to all charged particles including α particles, protons and delta electrons, which contribute to a significant background. Placing the silicon detector further away from the target than the germanium detectors helps to reduce the unwanted background. Another advantage to placing the detector upstream of the target is that delta electrons are preferentially emitted in the forward direction. Delta electrons are low-energy electrons produced when the beam and target particles collide. A high-voltage barrier with a potential of up

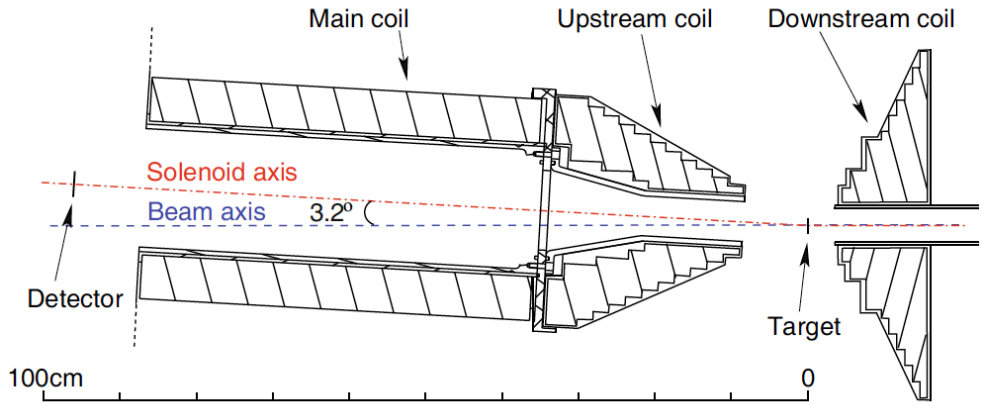

Figure 3.3: A schematic drawing to illustrate the geometry of the SAGE solenoid coils and silicon detector as seen from above [28].

to 50 kV can be applied to reflect most low-energy delta electrons. As a result of the detector being set back from the target, the conversion electrons must be transported to the detector via a system of solenoid coils with a maximum field of 0.8 T downstream of the target and an average value of 0.6 T upstream of the target. Figure 3.4 shows the coils along with the high-voltage barrier.

3.2.2 γ-ray Detection in SAGE

For γ-ray detection an array of 34 hyper-pure germanium (HPGe) detectors are used: 10 EUROGAM phase-I type Compton-suppressed germanium detectors [31] as described in section 3.1 and 24 four-fold segmented EUROGAM Clover detectors [27][32]. The detectors are arranged into three rings; one ring of EUROGAM phase-I type detectors at an angle of 134°and two rings of EUROGAM Clover detectors at angles of 75.5°and 104.5° with respect to the beam line.

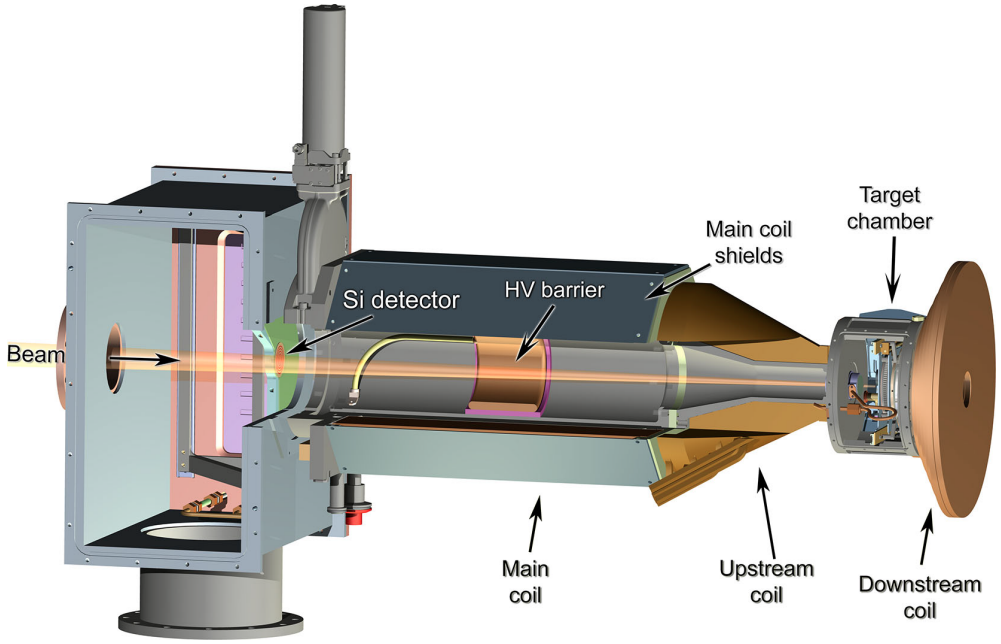

Figure 3.4: A close-up technical drawing of the SAGE electron detector. The location of the coils and the high-voltage barrier can be seen in relation to the silicon detector and target position. The beam is labelled and enters from the left [28].

The phase-I and Clover detectors are coaxial n-type semiconductor crystal detectors. The phase-I detectors are single HPGe crystals and the Clovers are four-fold segmented. The four crystals in the Clover detectors are mounted in a single cryostat and the segmentation is advantageous if a γ ray scatters between neighbouring crystals, depositing a portion of its energy in each segment. The full energy may be recovered by adding together the energies deposited in adjacent crystals using an in-code technique called add-back. The add-back technique looks for two or more γ rays detected in adjacent Clover crystals simultaneously. An assumption is made that these two γ rays are in fact the same γ ray that has scattered out of one crystal and into the adjacent crystal. The energy deposited in both crystals is added together and in this way the full energy of the γ ray is recovered.

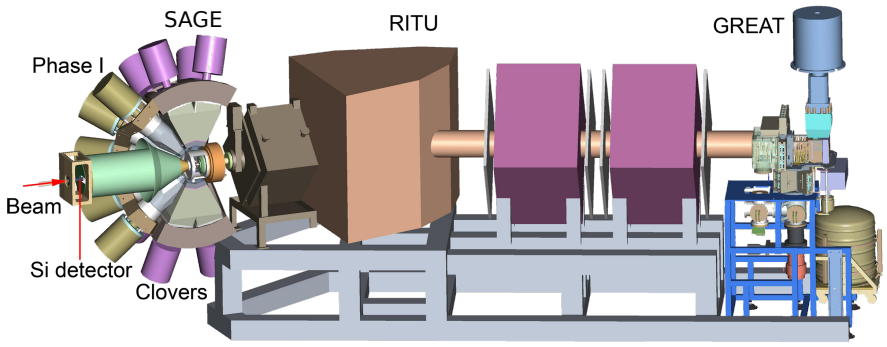

Figure 3.5: An artist's impression of the experimental apparatus at the University of Jyväskylä with JUROGAM on the left-hand side, the RITU gas-filled separator in the centre, and the GREAT spectrometer on the right-hand side [34].

3.3 RITU Separator

RITU is a gas-filled recoil separator used to separate unreacted beam from evaporation residues created at the target position [33]. RITU extends from the target position to the focal plane and uses three quadrupole magnets and a dipole magnet in the formation QDQQ. It separates the fusion evaporation residues, known as recoils[1] from unreacted beam and focuses them at the focal plane. The positioning of RITU can be seen in figure 3.5; it is situated between the target position and the focal-plane spectrometer.

Recoils are separated from the unreacted beam in the dipole magnet according to their different magnetic rigidities defined as

$$B_p = \frac{mv}{eq_{ave}}, \tag{3.1}$$

where B_p is magnetic rigidity, m is mass, v is velocity, and q_{ave} is the average charge state. The average charge state can also be expressed as

[1]Hereafter the term 'recoil' is used to refer to recoiling fusion evaporation residues.

$$q_{ave} = \frac{v}{v_0} Z^{1/3} \tag{3.2}$$

where v_0 is the Bohr velocity of 2.19 $\times$ 10^6 ms^{-1}. Therefore

$$B_p = 0.0277 A/Z^{1/3}. \tag{3.3}$$

From this equation it can be observed that the magnetic rigidity varies with the A:$Z^{1/3}$ ratio. This ratio increases on average with increasing nuclear mass, and so the magnetic rigidity also increases with increasing nuclear mass. Since the unreacted beam is usually a lighter mass species with a lower magnetic rigidity, it experiences a more sharply curved path. This makes RITU a highly effective device for suppressing unreacted beam.

The use of a gas-filled separator results in a loss of mass resolution due to the charge-exchange collisions in the field region that result in recoils travelling in the same average charge state. This means that RITU is not capable of mass separation but tends to have a much higher transmission efficiency than vacuum-mode recoil separators. Since the mass resolution of RITU is insufficient to separate isotopes by mass, the identification of the reaction products is normally based on their correlations with subsequent radioactive decay chains. The GREAT spectrometer based at the RITU focal plane is designed to detect recoil implantations and their subsequent emissions in a holistic manner.

3.4 GREAT Spectrometer

The GREAT spectrometer is used to identify recoils and their subsequent decays. It is an assembly of detectors depicted in figure 3.6. Each detector sub-system is used to detect different emissions [35]. The recoils created at

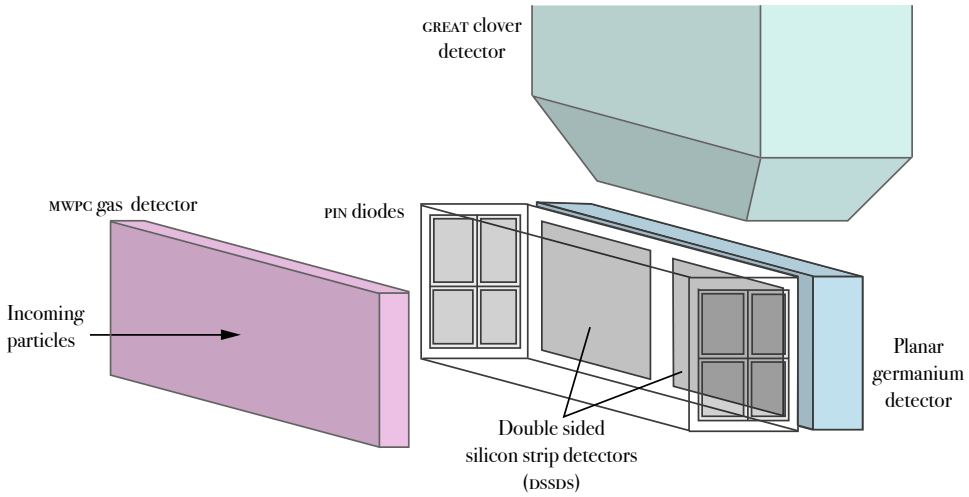

Figure 3.6: A schematic diagram representing the layout of the GREAT detector components. In the experiment described in this text there were two additional Clover detectors covering the left- and right-hand sides of the PIN diodes, DSSDs and planar germanium detector.

the target position arrive at the focal plane after a time equal to the flight time through RITU that depends on the mass and energy with which they are created. The typical time-of-flight is approximately 0.5 μs.

At the entrance of the GREAT spectrometer there is a transmission multiwire proportional counter (MWPC) with thin Mylar foil entrance and exit windows and an aperture of 131 mm $\times$ 50 mm. The MWPC is filled with isobutane gas, which provides an energy signal when recoiling reaction products traverse the gas. However, a radioactive decay such as an α particle from recoils implanted in the DSSDs will leave no trace in the gas and in this way energy loss in the MWPC can be used to distinguish recoils from α particles.

After travelling through the MWPC, the recoils are implanted into the double-sided silicon strip detectors (DSSDs). There are two DSSDs each with an active area of 60 mm $\times$ 40 mm and a thickness of 300 μm. The strip pitch is 1 mm in the horizontal and vertical directions giving 4800 pixels in total. Approximately 85% of all recoils are collected by the DSSDs where

their position and energy can be measured. Using the positional information radioactive decays can be attributed to particular recoil. If an α particle or an electron is detected in the same pixel as a recoil within an appropriate time interval, it may be assumed that the decay came from the recoil.

The implanted recoil in the DSSD detector may undergo internal conversion with some probability of the electron being emitted in the backwards direction. The PIN array is situated upstream of the DSSD detectors to measure conversion electron energies. The array consists of 28 silicon PIN diodes, each with an active area of 28 mm $\times$ 28 mm and a thickness of 500 μm. The efficiency of the array for detecting a full-energy peak is approximately 20% at 200 keV [36].

A planar double-sided germanium strip detector is located downstream from the DSSDs. The planar Ge detector is able to measure X-rays and low-energy γ rays emitted by the decay of the recoil. The planar detector has an active area of 120 mm $\times$ 60 mm, a thickness of 15 mm and a strip pitch of 5 mm. It is approximately 10 mm away from the DSSD detector and has a thin beryllium entrance window.

The planar detector has a high efficiency at low energies, however, because its thin construction results in a low γ-ray detection efficiency above 500 keV. This introduces the need for additional larger volume detectors detailed below.

The GREAT spectrometer also contains Clover detectors. These detectors are used to measure γ rays up to around 1 MeV, which is beyond the capability of the planar detectors. There is one large Clover detector situated above the planar germanium detector and two smaller ones to the left and right of the planar Ge detector. The smaller Clovers are the same size as those used in SAGE, however the larger Clover, known as the GREAT Clover, is much bigger with each of its four crystals being 105 mm long and 70 mm in diameter. The

crystals are tapered at an angle of 15°and each has a further four-fold electronic segmentation.

Chapter 4

Experimental Methodology

4.1 Synthesis of Exotic Nuclei

The nuclei studied in this work were produced using accelerated ion beams and stationary targets. In the first experiment the beam was ^{86}Sr and the target ^{92}Mo, and the second experiment used a beam of ^{82}Kr and a target of ^{100}Ru. Such collisions can result in fusion of the two nuclei creating a heavy neutron-deficient compound nucleus. This type of reaction is known as a heavy-ion fusion evaporation reaction and is ideal for creating proton-rich nuclei such as ^{179}Au due to the tendency for the nuclear chart to curve under the N=Z line. The compound nucleus is often produced with a huge surplus of energy and angular momentum and can be unstable to particle emission.

In order to lose angular momentum and energy and return to its ground state, the compound nucleus must first emit nucleons and α-particles. At this stage particle emission is favoured over γ emission as a more efficient way to dissipate excitation energy. These are known as evaporated particles and may only be emitted until the nucleus is within the nucleon separation energy ($\sim$8 MeV) of the yrast line. The yrast line represents the maximum

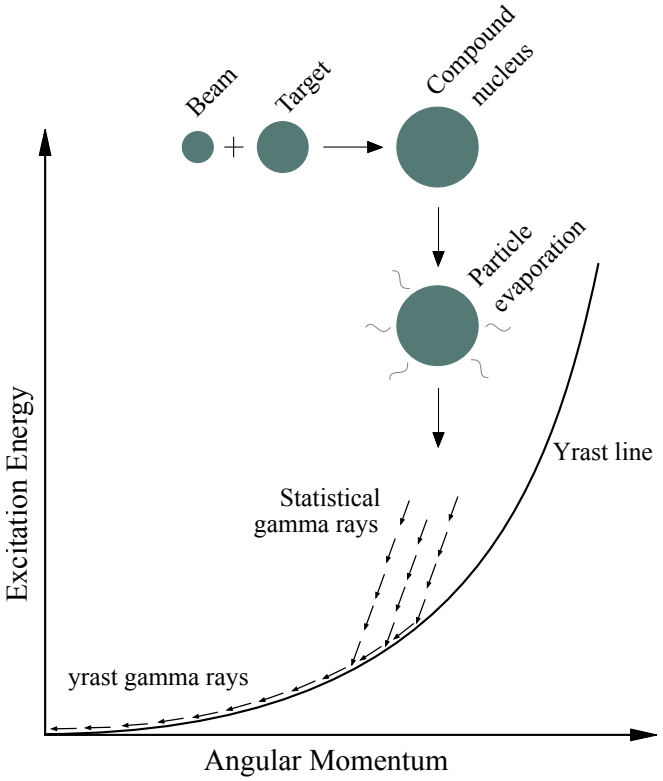

Figure 4.1: A schematic of the stages in a heavy-ion fusion-evaporation reaction.

angular momentum for a given excitation energy. Fusion-evaporation reactions preferentially populate states along the yrast line. Figure 4.1 illustrates the decay modes of the compound nucleus following a fusion-evaporation reaction.

4.2 Total Data Readout (TDR)

The Total Data Readout (TDR) is a triggerless data collection method, which was developed for the GREAT spectrometer [37]. Before TDR, recoil-decay tagging experiments relied on a hardware trigger to begin reading out data. Depending on the lifetimes of the nuclei of interest, a gate was set that defines how far back in time to look for events that are thought to be in delayed

coincidence with the focal-plane activity. In the study of nuclei with isomeric states it is often desirable to select time intervals of the order of several microseconds. During readout the focal-plane electronics are dead and unable to process events. There is also common dead time arising from the gate widths of different detector sub-systems. Dead time can quickly become a problem especially with the often large amount of activity produced in fusion-evaporation reactions, which can lead to events being missed.

TDR allows all data to be collected independently and timestamped from a global 100-MHz clock. Events can then be reconstructed in the event builder, using spatial and temporal correlations. This method is now feasible due to the ever increasing power of commercially available CPUs [37].

In the event builder, the user can set conditions to pick out correlations and reconstruct events. A simple example is to take one recoil event and look backwards in time over a period of roughly the time of flight through RITU. One can then observe γ ray rays detected by the JUROGAM array and consider that these γ rays are in delayed coincidence with the recoil. The recoil can also be correlated with an α decay should one occur later in the same DSSD pixel within the expected lifetime of the decay. Such correlations allow decays detected at the focal plane to be linked to γ-ray emissions at the target position.

4.2.1 GRAIN Software Package

GRAIN is a Java-based software package that allows users to reconstruct the output from the event builder [38]. The raw data stream can be interpreted by a user with an appropriate Java sort code. The user is able to pick out relevant data from the stream of information recorded and to make correlations between decay information from the target position and the focal plane. The output

can be seen in Grain's user interface.

4.3 Calibrations

Calibrations were required to ensure that the energies recorded in the detectors corresponded to the energies of the incident radiation. These calibrations will be detailed in the following sub-sections.

4.3.1 Energy Calibrations

The output signals of the detectors used in this work are directly proportional to the energy deposited in the detector by the incident radiation. There are a large number of detectors used in this set-up, with slight differences in their crystals or with a slightly differing bias voltages across them. For this reason, calibration is necessary to compensate for the differences between detectors. Calibrating involves aligning channel numbers with their correct energy so that each signal received has some meaning with regards to energy deposited.

For the germanium detectors at the focal plane and those that make up the JUROGAM array, an external calibration, that is an calibration using external ^{152}Eu and ^{133}Ba sources, must be completed. A calibration is necessary so that the electrical output of the detector crystals can be matched to the known energy values for these sources. The ^{152}Eu and ^{133}Ba sources in particular are useful because they have very well known peak energies across a broad energy range; the ^{152}Eu source emits γ rays from 121-1408 keV while the ^{133}Ba source provides useful low-energy calibration (80-384 keV) where the efficiency of JUROGAM varies considerably.

The same calibration method is also used to calibrate the remaining detectors however a different calibration source will be needed in each case depend-

ing on what type of radiation is measured by the detector. For example an electron emitter is required to calibrate the silicon detector in SAGE and for the PIN diodes.

The DSSDs require both and external and an internal calibration. First an external calibration is carried out using a source containing three α-decaying nuclei, specifically ^{241}Am, ^{239}Pu and ^{244}Cm, which produce α particles with energies 5388 keV, 5456 keV and 5763 keV, respectively. However the DSSD strips have a dead layer in which some of the α-particle's energy is deposited and so is not associated with a signal. The energy loss in the dead layer can be $\approx$80 keV. To rectify this an internal calibration from the experimental data is required that involves using α decays following a recoil implantation. In this method the energies in the α-spectrum can be identified and then corrected to their known literature values.

4.3.2 Doppler Correction

The products of the fusion evaporation reaction are created at high recoil speeds in these experiments ($\sim$4% of the speed of light). They de-excite by γ-ray emission in flight and so the γ-ray energies recorded in the target position germanium detectors are Doppler shifted away from their true values. The target position germanium arrays have several rings of detectors each at different polar angles with respect to the beam direction. Therefore γ rays that are emitted in the direction of the beam (forward direction) are detected with an energy greater than their true energy. Similarly γ rays emitted in the backward direction will be measured with lower energies.

The effects of Doppler shift can be seen in Figure 4.2. When each ring is plotted separately, the shifts in energy can be seen clearly, and if a summed spectrum should be taken from these rings it would result in wide peaks at

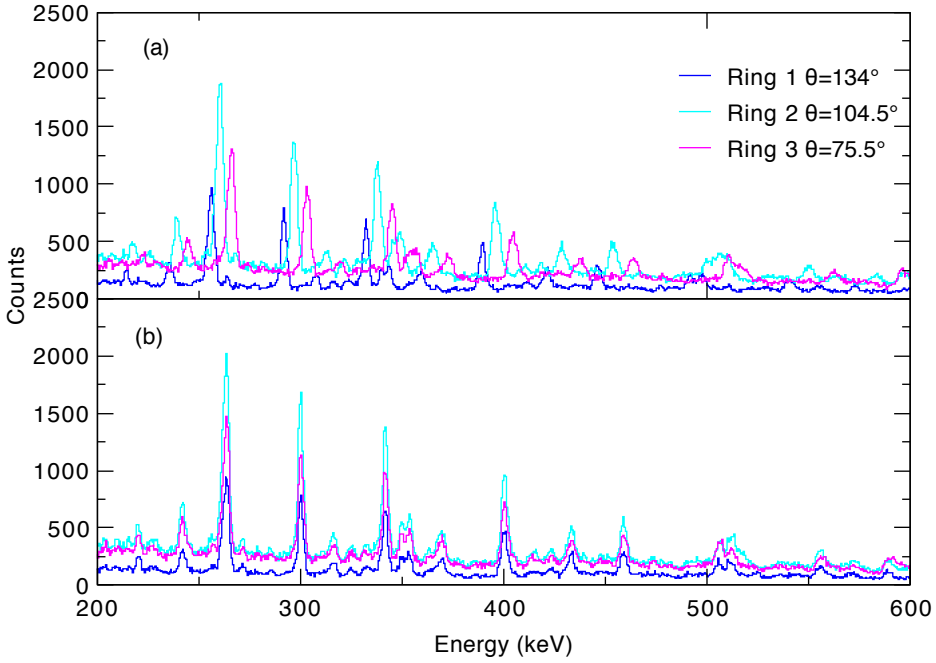

Figure 4.2: (a) Three rings of detectors from the SAGE array without any correction. (b) The same rings after Doppler correction applied. The polar angles in the legend correspond to the angle of the detectors with respect to the beam direction.

incorrect energies. Applying a Doppler correction leads to much sharper peaks at the correct energies.

The Doppler correction formula to first order is

$$E = E_0 \left(1 + \frac{v}{c} cos\theta\right), \tag{4.1}$$

where E is the energy detected at a specific angle in JUROGAM, E_0 is the true energy, v/c is the velocity of the reaction product as a fraction of the speed of light and θ is the angle between the beam axis and the detectors.

4.3.3 Efficiency Calibrations

To be able to make any meaningful comment on absolute emission rates of γ rays or electrons it is necessary to correct for the detector's ability to detect radiation of different energies. The efficiency of a detector is the amount of radiation detected compared with the total amount of radiation emitted. The efficiency calibrations for the SAGE germanium and silicon detectors are outlined in the following sections.

Germanium Array Efficiency

To measure the efficiency of the detectors that make up the JUROGAM and SAGE germanium arrays, ^{152}Eu and ^{133}Ba sources were used. The number of counts for each peak was recorded and compared with the number of counts expected for that peak using the equation

$$\eta = \frac{N}{AtI}, \tag{4.2}$$

where η is the absolute efficiency of the detector, A is the activity of the ^{152}Eu or ^{133}Ba calibration sources, t is the amount of time the spectrum was collected for and I is the intensity of the γ ray from the literature [39]. The measured efficiency data points are then fit using the Radware software package (EFFIT) [40]. The fitted function is defined as

$$\ln(\varepsilon) = \left\{(A + Bx + Cx^2)^{-G} + (D + Ey + Fy^2)^{-G}\right\}^{-1/G}, \tag{4.3}$$

where

$$x = \ln\left(\frac{E_\gamma}{100}\right), \tag{4.4}$$

$$y = \ln\left(\frac{E_\gamma}{1000}\right), \tag{4.5}$$

ε is the efficiency, and the γ-ray energy E_γ is in keV. A,B,C,D,E,F and G are variables that are extracted from fits to the data with EFFIT. The resultant efficiency curves are shown in figure 4.3 along with the measured data points.

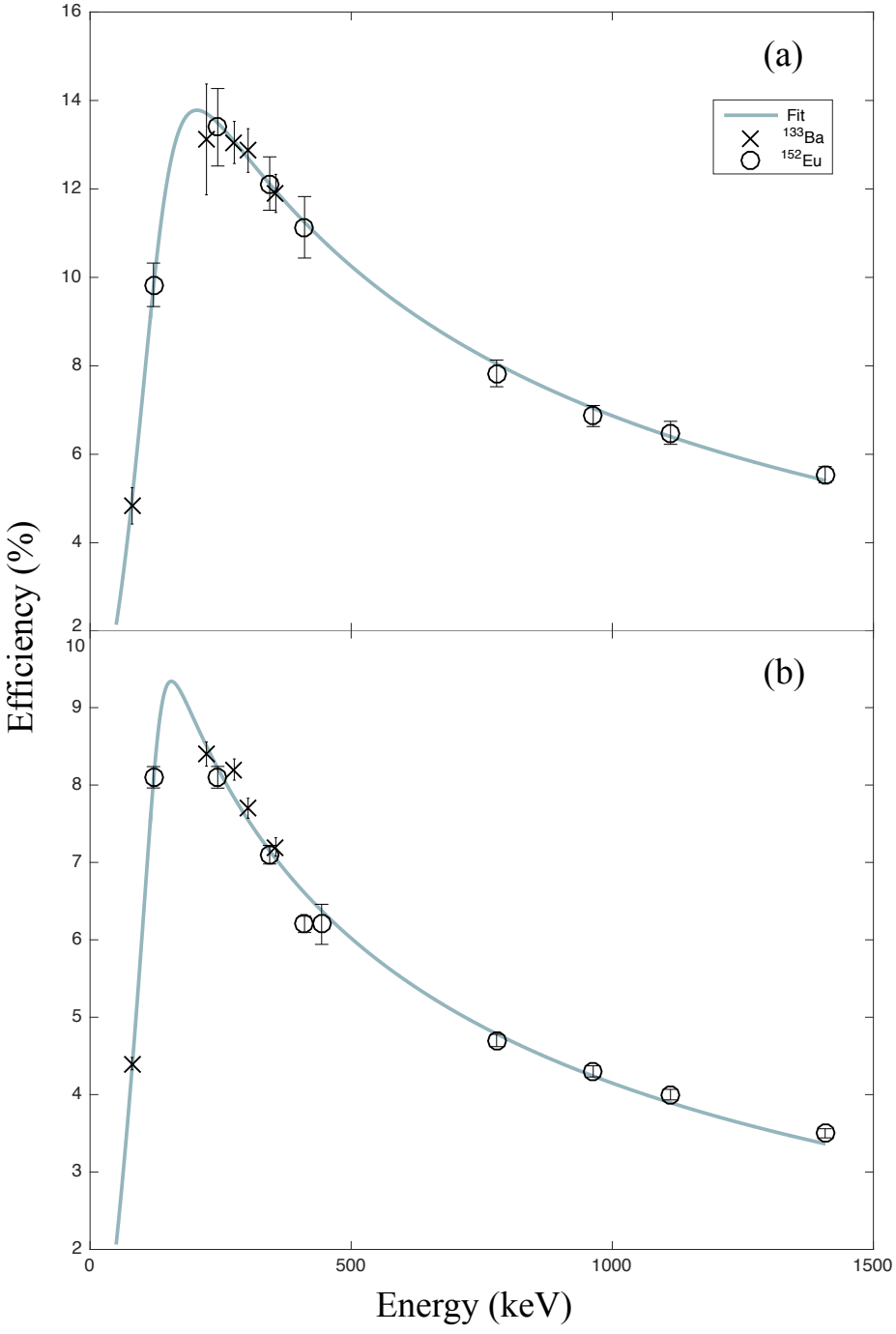

Figure 4.3: Absolute efficiency plots as a function of energy for (a) the JUROGAM array and (b) the SAGE germanium detectors.

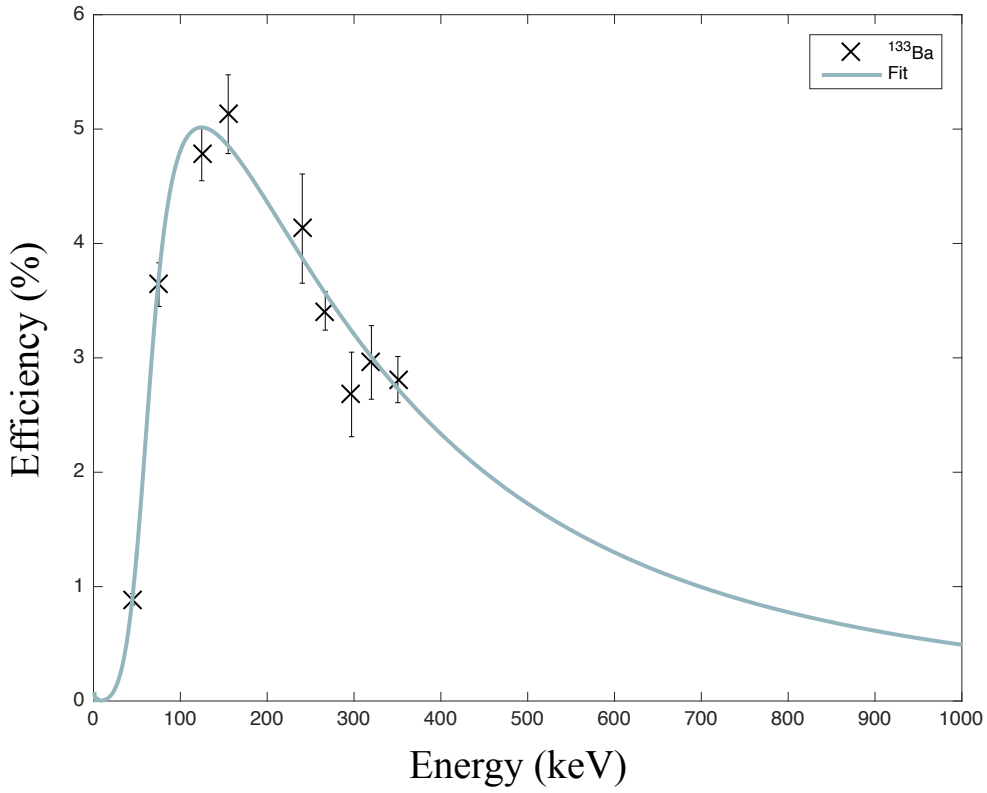

Figure 4.4: The efficiency of the SAGE silicon detectors as a function of energy.

SAGE Silicon Detector Efficiency

The ^{152}Eu and ^{133}Ba sources used in the last section are closed sources. To measure the detection efficiency of the SAGE silicon detectors an open ^{133}Ba source is required to ensure electrons are emitted without being absorbed or attenuated by any casing. For this reason the exact activity of the source is not known. However, since the open ^{133}Ba source is placed at the target position and barium emits both γ rays and electrons, a γ-ray spectrum can be recorded using the SAGE germanium detectors simultaneously with an electron spectrum using the silicon detector.

The SAGE germanium efficiency can then be calculated again with the open source. Since the efficiency of the germanium detectors is already known

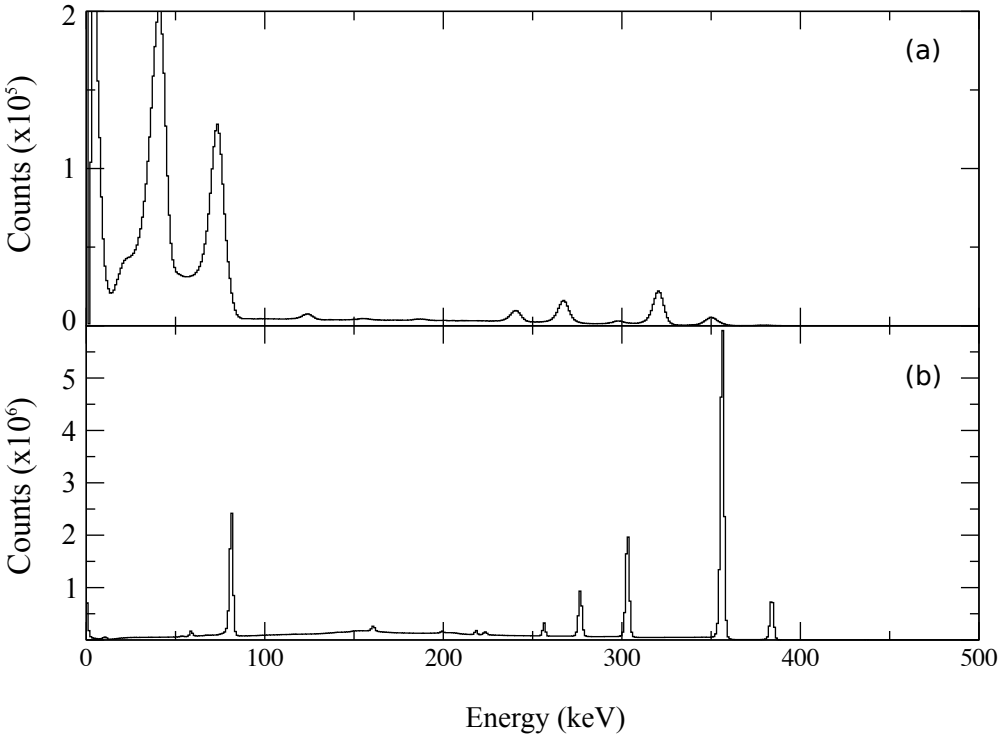

Figure 4.5: Spectra taken while a ^{133}Ba source was at the target position. (a) shows an electron spectrum taken with the annular silicon detector. (b) a γ-ray spectrum taken using the germanium detector array.

absolutely, the activity of the open source can be guessed and varied until the efficiency matches the value calculated previously using the closed source. Once the activity of the open ^{133}Ba source is established, the absolute efficiency of the silicon detectors can be calculated as before using equation 4.2 and fitted with EFFIT.

Evaluating Measured Efficiency

An advantage of having both silicon and germanium detectors at the target position is that the conversion coefficient, α, for a transition can be measured directly. Net areas of the electron peaks and the corresponding γ-ray peaks are measured and used to determine the conversion coefficients using equation

4.6

$$\alpha = \frac{N_e \varepsilon_{Ge}}{N_\gamma \varepsilon_{Si}}, \tag{4.6}$$

where N_{e} and N_γ are the number of counts in the electron and γ-ray peaks respectively, and ε_{Ge} and ε_{Si} are the measured absolute efficiencies of the germanium and silicon detectors, respectively.

Using the calibration source ^{133}Ba, which emits both electrons and photons, the conversion coefficients could be measured and compared to the literature values thereby indicating whether the calculated efficiency values are correct. The electron and γ-ray spectra are shown in 4.5. Literature values for comparison were found in the Nuclear Data Sheets [41] and BrIcc [42]. The measured conversion coefficients are listed along with the literature values in Tables 4.1 and 4.2 and graphically in Figure 4.6.

Energy(keV)	Multipolarity	M1	E2	Measured
79.6	M1 + E2	1.623	2.366	1.563 *14*
80.0	M1 + E2	1.600	2.333	1.199 *269*
160.6	M1 + E2	0.226	0.272	0.173 *12*
223.2	M1 + E2	0.0911	0.0937	0.0920 *80*
276.4	E2	0.0516	0.0475	0.0476 *5*
302.9	M1 + E2	0.0406	0.0357	0.0401 *19*
356.0	E2	0.0267	0.0218	0.0243 *1*
383.8	E2	0.0220	0.0175	0.0226 *17*

Table 4.1: Internal conversion coefficients for ^{133}Ba K-shell transitions. The M1 and E2 values are taken from BrIcc [42] and the measured values are determined as detailed in the text. The energy here refers to the transition energy.

Energy(keV)	Multipolarity	BrIccM1	BrIccE2	Measured
79.6	M1 + E2	0.2188	1.572	0.2434 *110*
80.0	M1 + E2	0.2156	1.536	0.2134 *1926*
160.6	M1 + E2	0.02975	0.07382	0.0548 *40*
223.2	M1 + E2	0.01203	0.01994	-
276.4	E2	0.00677	0.00896	0.00881 *457*
302.9	M1 + E2	0.00531	0.00645	0.00523 *11*
356.0	E2	0.00348	0.00369	0.00449 *23*
383.8	E2	0.00286	0.00287	0.00333 *17*

Table 4.2: Internal conversion coefficients for ^{133}Ba L-shell transitions. The M1 and E2 values are taken from BrIcc [42] and the measured values are determined as detailed in the text. The energy here refers to the transition energy.

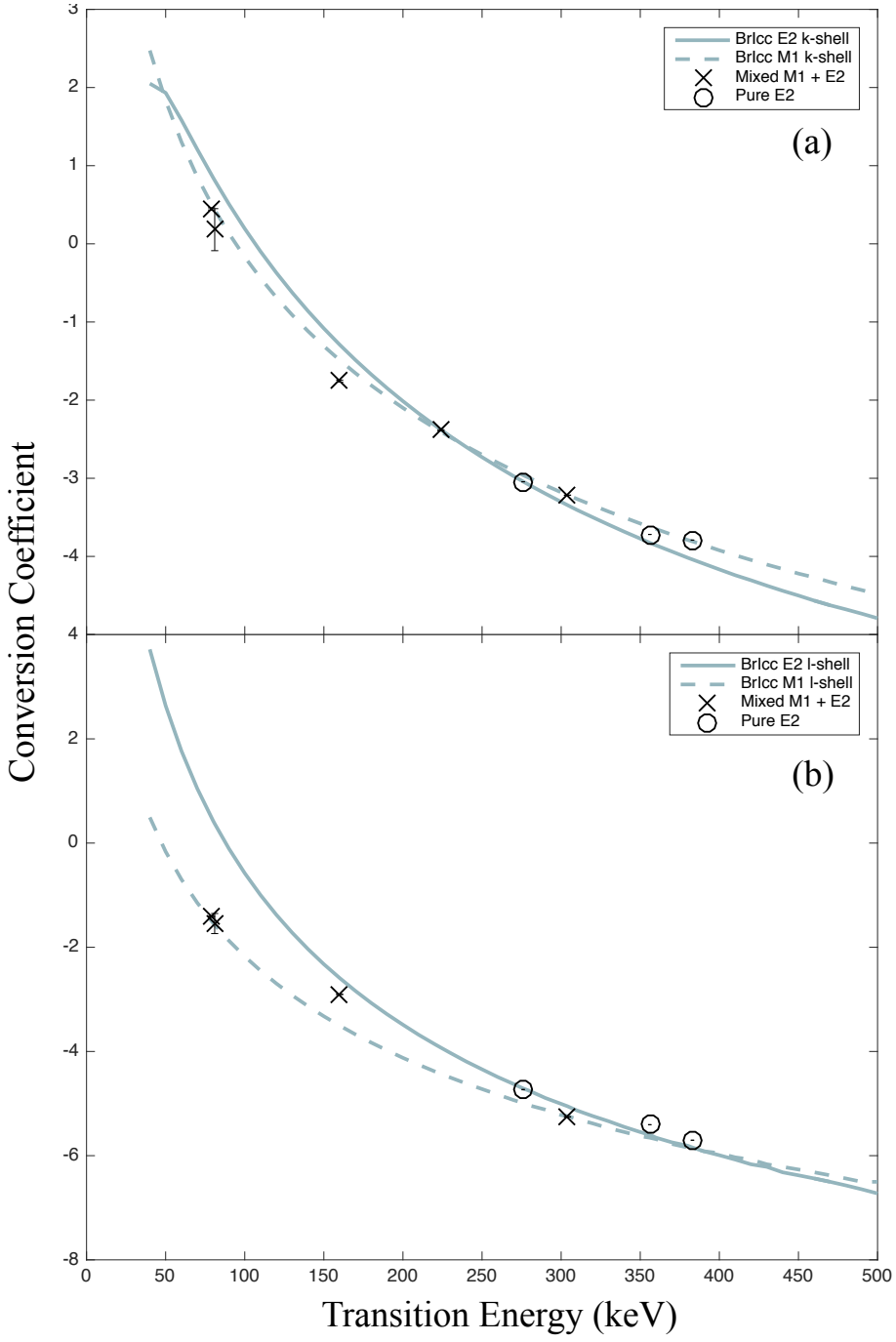

Figure 4.6: Conversion coefficients plotted as a function of transition energy for ^{133}Ba. Lines are plotted using theoretical data taken from BrIcc [42], the cross and circle points show the measured conversion coefficients for mixed M1 + E2 and pure E2 transitions, respectively. (a) Data for K-shell electron transitions. (b) Data for L-shell transitions.

4.4 Correlation Methods

Although it is possible to adjust the beam energy to optimise the yield of particular exit channels from fusion evaporation reactions, there will always be several open reactions channels. These channels can often have reaction cross sections that are much larger than the desired nucleus of interest. Thus when studying neutron-deficient nuclei with low cross sections there is likely to be a high γ-ray background arising from other fusion evaporation channels and, in heavy nuclei, fission. These problems can be mitigated by using the target-position germanium detectors (and silicon detector in the case of SAGE) in conjunction with the RITU separator, the GREAT focal plane detectors and the triggerless timestamping data acquisition system. With a time-stamped data stream it is possible to utilise correlation methods to minimise the backgrounds arising for other sources.

4.4.1 Recoil Identification

Some scaterred unreacted beam will reach the focal-plane detectors since the beam and target nuclei only fuse with some finite probability. The recoils result from the fusion of beam and target nuclei so they will be more massive than the unreacted beam and therefore will move slower in the filling gas resulting in a longer time-of-flight through RITU. The recoils will usually have a higher Z, meaning they are more ionising than unreacted beam in the MWPC.

Recoils can be discriminated from unreacted beam by creating a two-dimensional matrix of the energy deposited in the MWPC against the time-of-flight extracted from timing signals between the MWPC and the DSSDs. This makes it possible to separate the recoils from the unreacted beam by means of a two-dimensional gate as shown in figure 4.7. This is often referred to as the

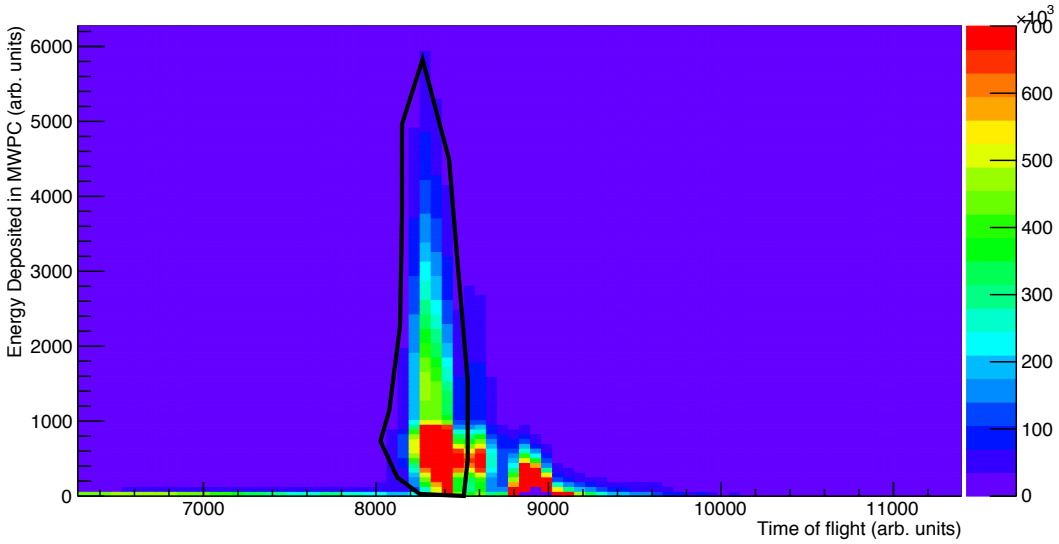

Figure 4.7: Flight time of nuclei through RITU plotted against the energy deposited in the GREAT MWPC. The black line is an example of a two-dimensional gate that is used to select recoils.

tof-de gate, as an abbreviation for the time of flight versus energy deposited.

4.4.2 Correlating Recoils and Prompt γ Rays

Once the recoils have been identified, they can be correlated with γ rays detected at the target position germanium detectors by taking into account the flight time of the recoils through RITU. A similar method to that outlined above is employed. A two-dimensional matrix of the recoil time-of-flight between the MWPC and the DSSD detectors versus the time difference between γ rays detected at the target position and a recoil in the DSSD detectors can be used. This enabled the identification of recoils, which have a sensible time-of-flight through RITU and are in delayed coincidence with γ rays at the target position. The matrix is shown in 4.8.

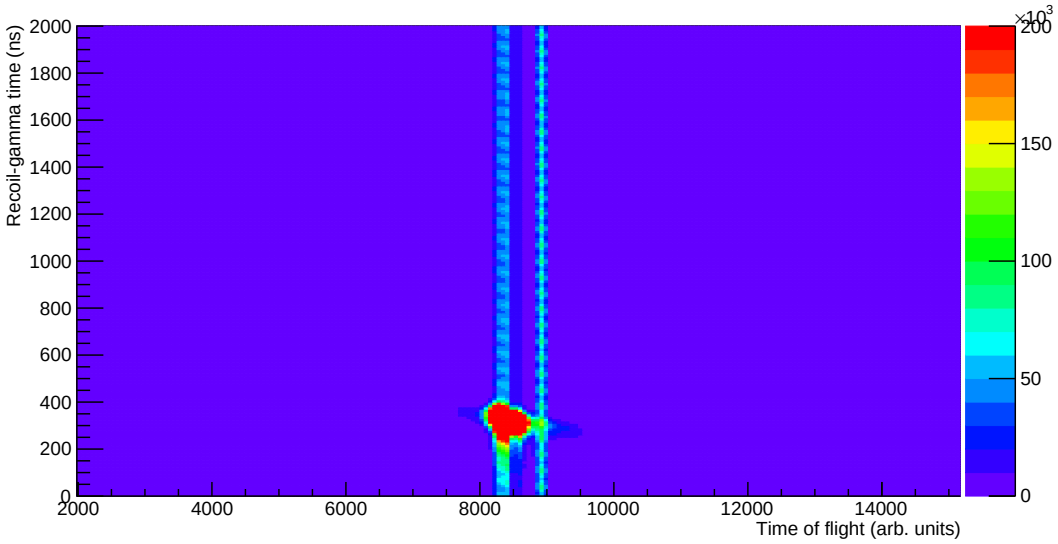

Figure 4.8: Time of flight of recoils between the GREAT MWPC and DSSD detectors plotted against the time difference between the detection of a γ ray at the target position and a recoil at the DSSD detectors.

4.4.3 Recoil-decay Tagging Technique (RDT)

The recoil-decay tagging technique (RDT) [43] can be used to identify γ rays from a specific nucleus. This involves using spatial and temporal correlations between a recoil implantation in a DSSD pixel with its subsequent characteristic radioactive decay. The DSSD is pixellated, which enables a spatial correlation between recoils and any subsequent decays. The RDT technique relies on the recoil and ensuant α decay being in the same pixel for correlation. In addition to spatial correlation there is a temporal condition. A suitable correlation time between recoil and α particle detection is chosen based on the half life of the nucleus being studied. The time chosen is normally up to four half-lives depending on the recoil implantation rate.

4.4.4 Isomer-tagging Technique

In the data set analysed in this work using SAGE there are contaminants with overlapping α-decay energies from products with similar γ-ray energies. For these reasons RDT was not always helpful. Instead γ-ray emissions from known isomers in ^{179}Au [44] detected at the focal plane were employed.

Isomer tagging associates isomer-delayed γ rays detected in the focal plane Clover with a recoil in the DSSDs within a specific time frame. The recoils are then associated with prompt γ rays detected at the target position by way of the two-dimensional matrix outlined in 4.4.2. Consider the case that the fusion-evaporation reaction produces a recoiling nucleus in an excited state. This recoil emits a cascade of γ rays at the target position that feeds an isomeric state with a much longer half-life. The recoiling nucleus is transported to the focal plane in the isomeric state and implanted into one of the DSSDs. The isomer may de-excite some time later at the focal plane by γ emission or through a radioactive decay mode. With isomer tagging, the γ rays detected at the target position can be correlated with the isomer decays at the focal plane and a more complete picture of the decay can be constructed. This correlation with isomer-delayed γ rays can result in a significant reduction in the γ-ray background.

Chapter 5

Shape Coexistence in the Proton Unbound Nucleus ^{175}Au

Excited states in the neutron-deficient nucleus ^{175}Au have been populated following the ^{92}Mo(^{86}Sr, p2n) reaction in an experiment completed at the University of Jyväskylä Accelerator Laboratory. The JUROGAM γ-ray spectrometer detected γ rays produced at the target position, which were correlated with the characteristic α decays of ^{175}Au detected in the GREAT focal plane spectrometer following a recoil implantation. The level scheme above the α-decaying $11/2^-$ isomer in ^{175}Au has been extended by 32 new γ-ray transitions, which have been associated with collective bands and single-particle states. These structures have been interpreted in terms of coexisting proton-hole and proton-intruder type configurations. Correlations with the subsequent α decays of ^{171}Ir, the daughter of α-decaying ^{175}Au have allowed nine newly observed γ rays to be unambiguously assigned as cascades feeding the ground state of ^{175}Au.

5.1 Motivation and Previous Studies

Shape coexistence describes the phenomenon where a nucleus exhibits configurations built on different nuclear shapes within a small range of excitation energies ($\sim 10^2$ keV) compared with the mass scale of heavy nuclei ($\sim 10^2$ GeV). The phenomenon arises from the interplay between the stabilising effect of closed shells and the residual interactions between nucleons, which increases the correlation energy. A nucleus with fully occupied shells tends to have a spherical or near-spherical shape. However a nucleus with a partially filled shell will tend to adopt a deformed shape due to the interaction between these valence nucleons. Coexisting shapes can be interpreted in terms of the shell model or other mean-field theoretical approaches. In terms of the shell model, one can intuitively interpret the structures as arising from multiple particle-hole (mp-nh) excitations of valence nucleons across closed shells leading to collective structures based on these configurations [2][47]. The isotopes studied in this work are in the vicinity of the Z = 82 shell gap and close to the N = 104 midshell making this an ideal region to study shape coexistence.

The nucleus ^{175}Au is only six neutrons heavier than the lightest of the known gold isotopes yet 22 fewer neutrons than the only stable isotope. The discovery of ^{175}Au was published in 1975 by Cabot *et al.* [48]. The isotope was produced in Orsay at the ALICE facility by fusion evaporation reactions. A 40 nA beam of Ca^{13+} ions bombarded ^{141}Pr and ^{150}Sm targets producing excited Au isotopes. The reaction products were identified by their α-decay energies and the unknown α peaks were assigned to isotopes based on comparison with theoretical relative excitation functions [48]. An α peak with energy 6.44 MeV was observed and associated with ^{175}Au.

A level scheme of excited states in ^{175}Au was established with a fusion-

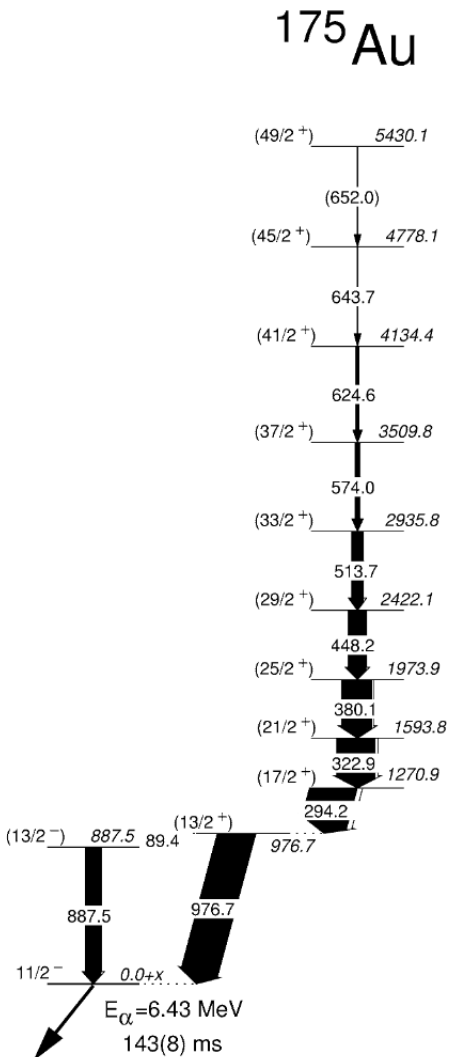

Figure 5.1: The level scheme of ^{175}Au deduced by Kondev *et al.* reproduced from Ref. [45].

evaporation reaction at the ATLAS superconducting linear accelerator facility at Argonne National Laboratory [45]. The reaction involved a beam of ^{84}Sr ions impinging on targets of ^{94}Mo at beam energies of 380 MeV and 385 MeV. The recoil-decay tagging technique, described in section 4.4.3, was employed to correlate γ-ray emissions with the characteristic radioactive decays of ^{175}Au nuclei, leading to the first level scheme of excited states in ^{175}Au shown in Figure 5.1.

Kondev *et al.* made configuration assignments for the underlying struc-

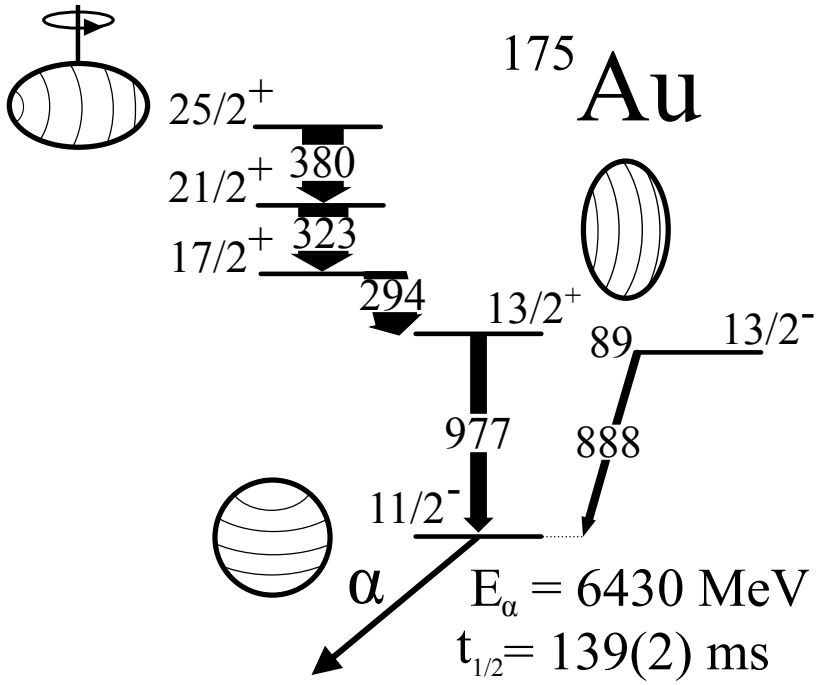

Figure 5.2: Figure illustrating the three known shapes present in ^{175}Au reproduced from reference [46].

tures. The α-decaying state was assigned a spin and parity of $I^{\pi} = 11/2^{-}$ arising from the $11/2^{-}[505]$ ($h_{11/2}$) proton Nilsson configuration. The yrast band in ^{175}Au was assigned to be a prolate $i_{13/2}$ proton intruder band that feeds an oblate $13/2^{+}$ band head [49]. The character of these configurations was probed further in lifetime measurements performed at the University of Jyväskylä by Watkins *et al.* using the Köln plunger device in conjunction with the recoil-decay tagging technique [50]. This study provided evidence to support the configuration assignments made by Kondev *et al.* and confirmed the presence of at least three coexisting nuclear shapes in ^{175}Au. Figure 5.2 illustrates the three known shapes in ^{175}Au.

The ground-state α decay of ^{175}Au was identified in a later study of the correlated α-decay chains of the ground and low-lying isomeric states in ^{179}Tl

performed by Andreyev *et al.* [51]. Andreyev *et al.* established that the α decays from the ground state and $11/2^-$ isomer in ^{175}Au have identical energies within experimental uncertainties at 6433(4) keV and 6432(5) keV, respectively. The extrapolation of Q-value trends for proton and α radioactivity in the Au isotopes reported by Page indicates that the excitation energy of the $11/2^-$ isomer relative to the ^{175}Au ground state is 176(60) keV [52]. This is consistent with measurements for the excitation energy of the $11/2^-[505]$ ($h_{11/2}$) Nilsson configuration in the heavier Au isotopes, which remains remarkably similar as a function of neutron number despite changes in the underlying core deformation from a nearly spherical shape in ^{171}Au [53] to a triaxial rotor in ^{185}Au [54].

Recent recoil-decay tagging experiments focusing on ^{177}Au by Venhart *et al.* [55] and Ali [56] have established proton-hole configurations coupled to excitations of the ^{178}Hg core that coexist with intruder bands based on exciting the odd proton into orbitals across the $Z = 82$ closed shell. The excited 0^+ state excitation energies in the Hg isotopes exhibit a parabolic dependence on neutron number with a minimum at N = 102 near the neutron midshell. However, recent mean-field calculations suggest that this smooth parabolic behaviour may obscure differences in the shape of the underlying potentials from which these states originate [57]. The calculations of Yao *et al.* predict that the relative excitation energies of the oblate and prolate minima could be exchanged in the highly neutron-deficient Hg isotopes. The coexistence of both proton-particle and proton-hole configurations observed in odd-mass neutron-deficient Au isotopes provides an interesting possibility for probing the evolution of such states beyond the proton drip line.

5.2 The Experiment

The K130 cyclotron at the University of Jyväskylä Accelerator Laboratory accelerated a beam of ^{86}Sr ions to 403 MeV, which were directed onto a stationary, 600 μg/cm^2 thick, ^{92}Mo target. The resultant fusion-reaction produced a compound nucleus of ^{178}Hg. Excited states in ^{175}Au were populated via the $p2n$ evaporation channel. The reaction cross section was estimated to be ≈ 0.5 mb. Gamma rays emitted at the target position were detected by the JUROGAM γ-ray spectrometer and the fusion products were transported via the RITU gas-filled separator [33] to the GREAT focal plane spectrometer [35]. RITU separated the reaction products (recoils) from the unreacted primary beam and fission products. The recoils were then implanted into the GREAT DSSDs. Recoils were discriminated from any unreacted scattered beam by way of energy loss measurements in the GREAT multiwire proportional counter and, in conjunction with the GREAT DSSDs [37] time-of-flight measurements. The TDR data acquisition system allowed signals from all detectors to be read out independently in a time-correlated stream [37]. The data were analysed using the Grain [38] and Radware [40] software packages.

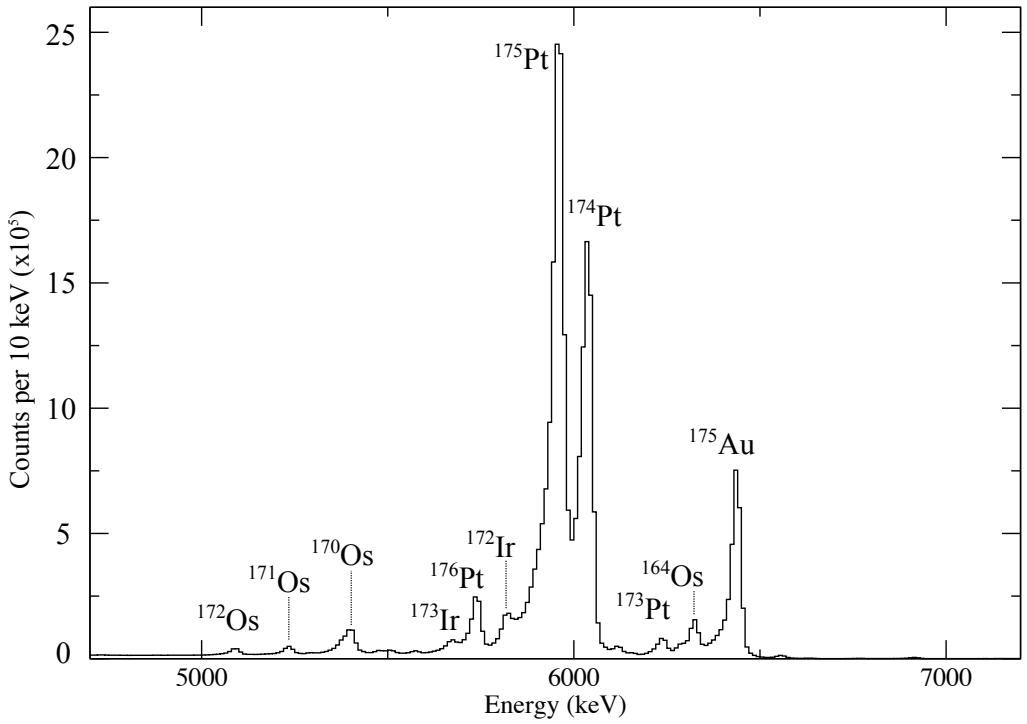

Figure 5.3: Alpha decays following recoil implantation in the same pixel of the GREAT DSSDs within 800ms.

5.3 Results

5.3.1 Recoil-decay Correlations with $\alpha(^{175}\mathrm{Au})$-decay Chains

Figure 5.3 shows an α-decay spectrum which contains α-decays which follow a recoil implantation in the same pixel of the GREAT DSSD detectors. Clearly the fusion evaporation reaction produced a number of open channels, many of which undergo α decay. The α-decay peak from ^{175}Au is well separated from other α decays and does not lie on a significant α-escape background due to its relatively high energy, which is useful for recoil-decay tagging studies. Sufficient statistics were collected during the experiment to identify γ-ray emissions in ^{175}Au at the target position using spatial and temporal correlations with

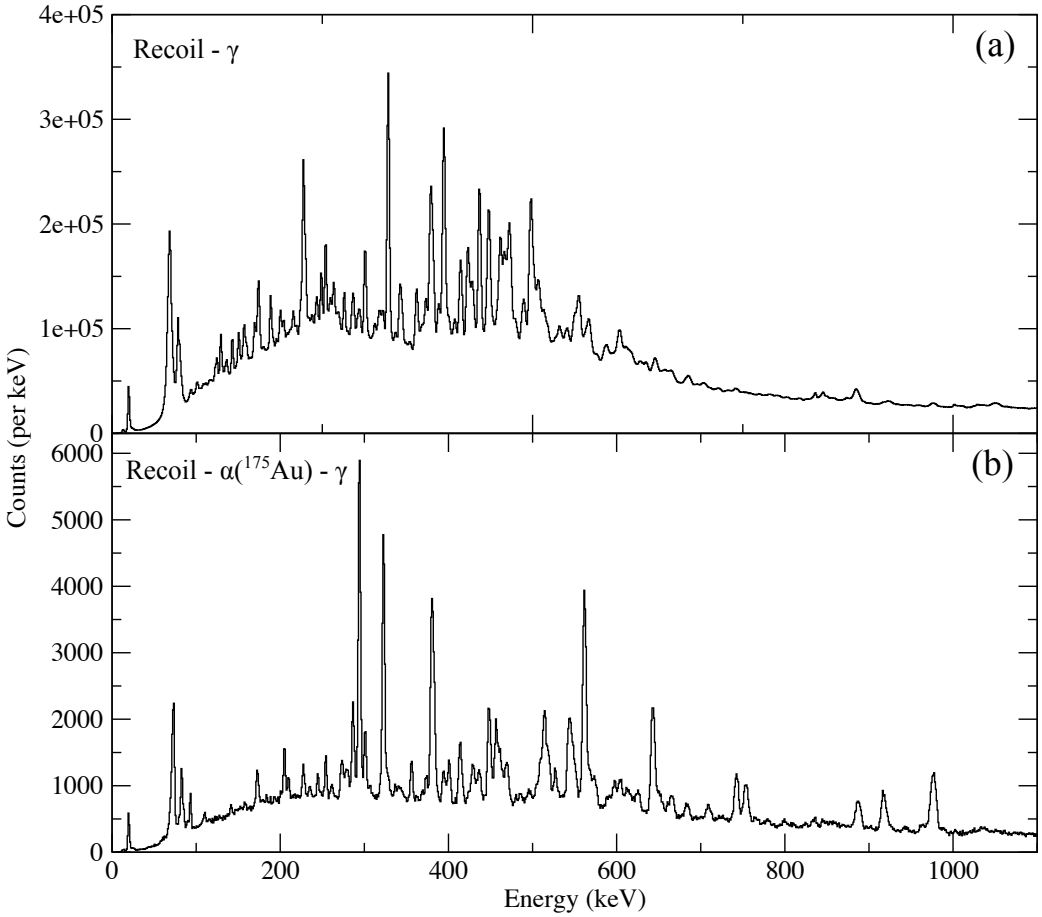

Figure 5.4: Spectra demonstrating the effectiveness of recoil-decay tagging. (a) γ rays in delayed coincidence with recoil implantations in the GREAT DSSDs. (b) γ rays in delayed coincidence with implanted recoils that are followed by a ^{175}Au α decay in the same DSSD pixel. The recoil-decay correlation time was limited to 800 ms.

the characteristic radioactive decays of implanted recoils detected at the focal plane of the recoil separator. A description of the recoil-decay tagging (RDT) technique can be found in section 4.4.3. The RDT method can be used to suppress the high γ-ray backgrounds arising from fission and other fusion products with higher cross sections, allowing weak structures in highly neutron-deficient nuclides to be identified. Nuclei with short half-lives and high decay branching ratios provide the optimal cases for study. The α-decay properties of ^{175}Au are well suited to RDT studies.

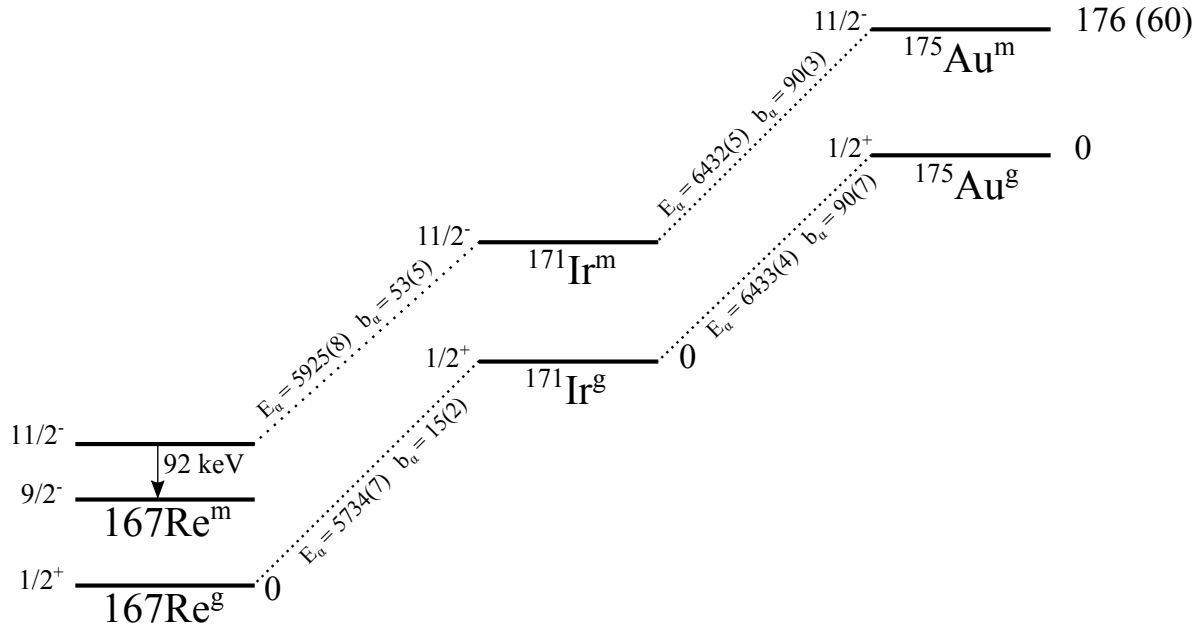

Figure 5.5: A schematic of the α-decay chain from ground and isomeric states in ^{175}Au to ^{167}Re. The subscripts g and m signify the ground and isomeric states, respectively. The decay properties have been taken from reference [51].

The effectiveness of the RDT method is demonstrated in Figure 5.4. Figure 5.4(a) shows γ rays detected in delayed coincidence with recoil implantations detected in the focal-plane DSSDs. The spectrum shows γ rays emitted from several recoiling fusion products. Figure 5.4(b) shows γ rays in delayed coincidence with recoil implantations followed by ^{175}Au α decays within the same DSSD pixel within 800 ms. The γ-ray emissions from contaminants are reduced significantly; for example, the peaks at 887 keV, 918 keV and 977 keV that are buried underneath the background in Figure 5.4(a) are discernible in Figure 5.4(b).

The α decays from ^{179}Tl to ^{175}Au and subsequent decays through the daughter ^{171}Ir to ^{167}Re have been recently measured by Andreyev *et al.* [51]. Figure 5.5 shows a schematic of these and subsequent α decays. Two ^{175}Au α decays have been identified; the first from the $1/2^+$ ground state in ^{175}Au which

feeds the ground state in ^{171}Ir and the second from the isomeric $11/2^-$ state which feeds an isomeric $11/2^-$ state in ^{171}Ir. The ground-state and isomeric α decays are found to have energies 6433(4) keV and 6432(5) keV, respectively. This energy difference is too small to be resolved in the DSSDs used in this experiment therefore the recoil decay correlations shown in Figure 5.4(b) would show γ rays feeding both the ground and isomeric states. However, ^{171}Ir also undergoes α decay from its ground state and low-lying $11/2^-$ isomer and its α decays have distinct energies that are $\approx$ 200 keV apart. A separation of this size is resolvable using the DSSDs. Therefore mother-daughter correlations can be used to identify and distinguish between the γ-ray cascades that feed the two α-decaying states in ^{175}Au. In addition, the ^{171}Ir α decay from the $11/2^-$ isomer feeds a low-lying $11/2^-$ state in the daughter nucleus ^{167}Re, which decays promptly to a $9/2^-$ band head by the emission of a 92-keV γ ray. The 92-keV transition has been observed in prompt coincidence with the $11/2^-$ α decay in previous studies and can be used to validate recoil-decay correlations in this work.

Figure 5.6 shows all second generation α decays that follow recoil implantations correlated with a characteristic ^{175}Au parent α decay within the same DSSD pixel. The correlation time between recoil implantations and the first generation α decay was limited to 800 ms. The half-lives of the ^{175}Au$^{\mathrm{m}}$ and ^{175}Au$^{\mathrm{g}}$ α decays are 138(5) ms and 207(7) ms, respectively. Thus the 800 ms correlation time corresponds to approximately five times the half-life of the ^{175}Au$^{\mathrm{m}}$ α decay and approximately four times the half-life of the ^{175}Au$^{\mathrm{g}}$ α decay. The correlation time between the first and second generation α decays was limited to 10 s such that

$$R \overset{800ms}{\rightarrow} \alpha(^{175}Au) \overset{10s}{\rightarrow} \alpha(ANY), \tag{5.1}$$

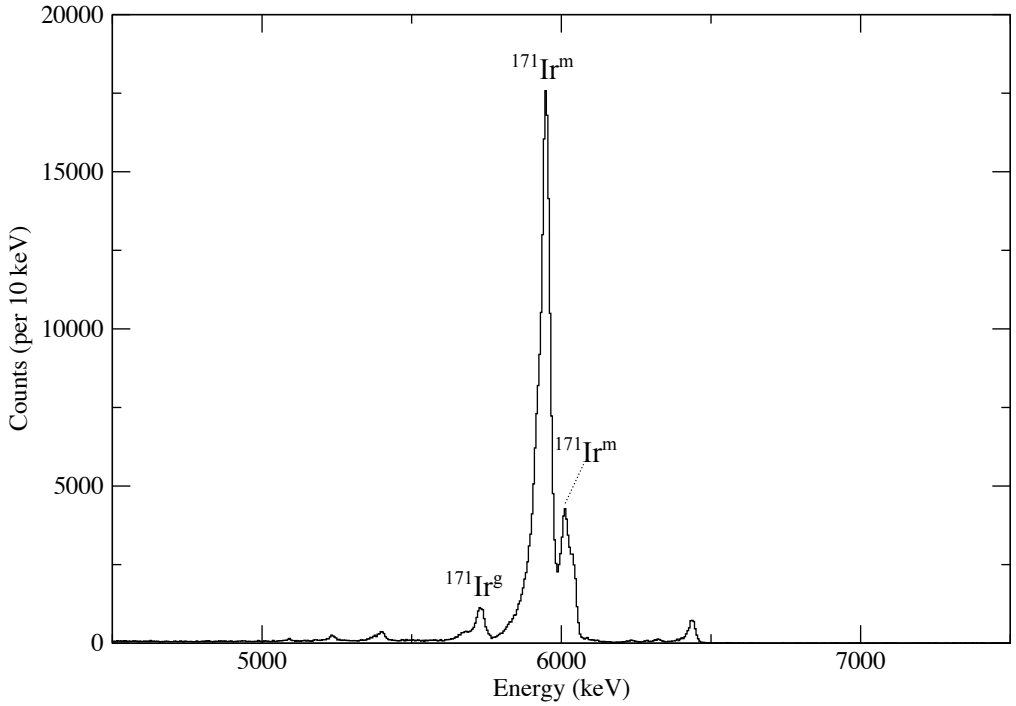

Figure 5.6: A spectrum showing α decays subsequent to the detection of a recoil and a characteristic ^{175}Au α decay in the same DSSD pixel. The correlation time between recoil implantations and the first generation ^{175}Au α decay was limited to 800 ms. The correlation time between ^{175}Au and the next α decay was limited to 10 s. The ^{175}Au α-decay peak at 6433 keV is seen in this spectrum due to random correlations.

where R denotes any recoil. The ^{171}Ir α decays and their subsequent daughters dominate the spectrum shown in Figure 5.6. In addition to the dominant 5925-keV ($11/2^- \rightarrow 11/2^-$) peak there is a significant α decay peak at 6010 keV, which cannot be attributed to ^{171}Ir or any of its subsequent decay chain.

In order to investigate the origin of this peak γ rays detected in the GREAT planar detector in prompt coincidence with α decays following a recoil-α(^{175}Au) correlation were sorted into an $\alpha - \gamma$ coincidence matrix. The time difference between a ^{175}Au α decay and the next α decay was limited to 10 s. Figure 5.7(a) shows γ rays in coincidence with the known ^{171}Ir$^{\mathrm{m}}$ decay at 5925 keV. This spectrum demonstrates a clear coincidence with the 92-keV γ decay in ^{167}Re as expected. Figure 5.7(b) shows the γ rays in coincidence with the

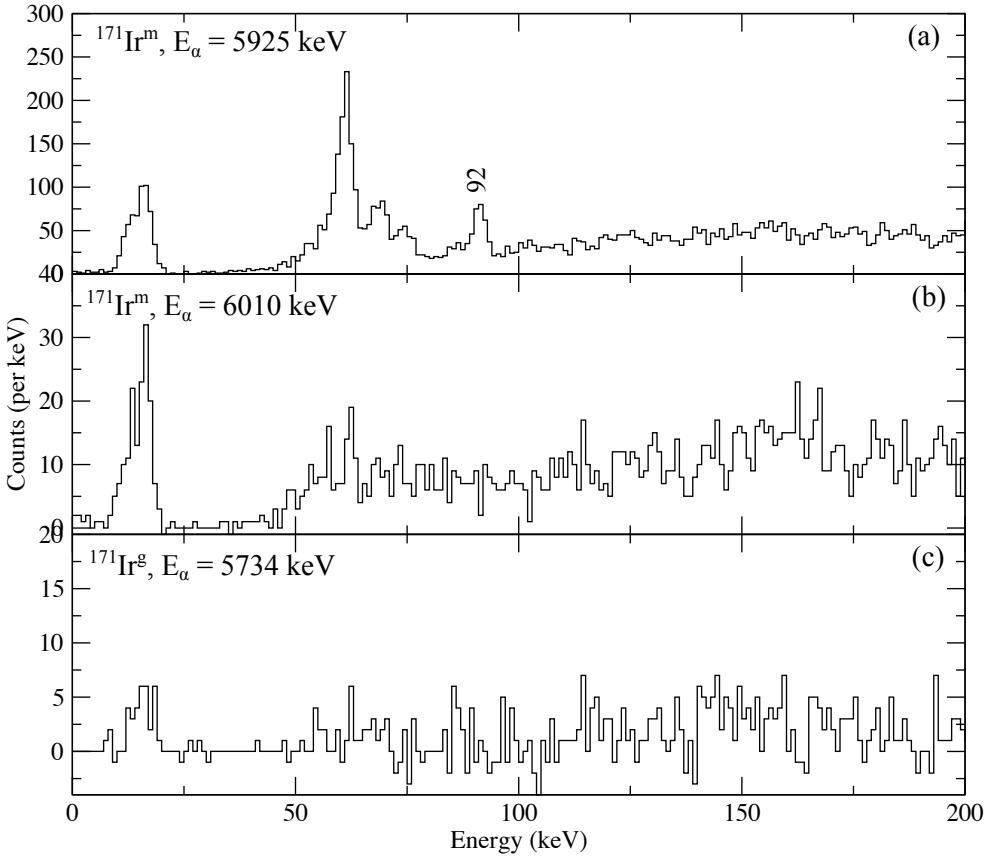

Figure 5.7: The γ rays obtained from an α-γ matrix. The γ rays are those seen in the focal-plane planar detector following a recoil-$\alpha_{(^{175}\mathrm{Au})}$-$\alpha$ correlation. (a) The γ rays seen at the focal plane when tagging on the 5925-keV ^{171}Ir α decay. (b) γ rays associated with the 6010-keV ^{171}Ir α decay. (c) γ rays associated with the 5734-keV ^{171}Ir ground-state α decay.

unidentified peak at 6010 keV and reveals nothing but background. A similar observation is made when demanding coincidences with the known α decay from the ^{171}Ir^{g} state.

There are two possible scenarios to explain the origin of the 6010-keV peak. In the first scenario, the 6010-keV peak could arise from conversion electron summing with the 5925-keV $(11/2^- \rightarrow 11/2^-)$ α decay. The 92-keV transition in ^{167}Re is likely to be a mixed M1/E2 transition and could proceed via the emission of a conversion electron. The binding energies for the ^{167}Re electron

Shell	Electron Binding Energy (keV)
K	71.676
L_1	12.527
L_2	11.959
L_3	10.535
M_1	2.932
M_2	2.682
M_3	2.367
M_4	1.949
M_5	1.883

Table 5.1: Binding energy of electron shells in the Re isotopes. The values are taken from the Table of Isotopes [58].

shells range from 71.676 keV for the K-shell to 1.883 keV for the m_5-shell, Table 5.1 details the binding energies of electrons in the Re isotopes. Therefore the conversion electrons could deposit up to 90 keV added to the 5925-keV α particle. This would result in a peak at a higher energy than the true α peak and may explain the origin of the 6010-keV peak. Moreover, transitions proceeding by internal conversion would not result in a γ-ray transition in the recoil-decay correlations shown in Figure 5.7(b).

Alternatively, the α-decay selection rules permit the possibility of an α decay from the $11/2^-$ state in ^{171}Ir to the $9/2^-$ state in ^{167}Re. In this instance the peak at 6010 keV could be interpreted as fine structure in the $^{171}\mathrm{Ir}^{\mathrm{m}}$ α decay superimposed on the $\alpha(^{171}\mathrm{Ir}^{\mathrm{m}})$-conversion electron sum peak. It is difficult to choose one scenario unambiguously with the present data. A simulation making assumptions about the M1/E2 mixing ratio would be required to reproduce the decay-particle spectrum in Figure 5.6.

5.3.2 Identification of γ Rays in ^{175}Au

The two known α decays of ^{175}Au are so close in energy to be indistinguishable. However, the two known ^{171}Ir daughter states decay with distinct α-particle energies so the ^{171}Ir daughters can be used to distinguish the γ rays feeding the ground state from those that feed the $11/2^-$ isomeric state. A two-dimensional correlation matrix was generated using the second generation α decays following a recoil-α(^{175}Au) correlation against the γ-ray transition energy detected in the JUROGAM spectrometer at the target position. Figure 5.8 shows γ rays detected at the target position that have a delayed coincidence with each of the three α peaks associated with the radioactive decay of ^{171}Ir.

Figure 5.8(a) shows γ rays observed in coincidence with the 5925-keV α decay from $11/2^-$ isomer in ^{171}Ir. The spectrum has many γ rays that were previously identified by Kondev *et al.* [45]. Figure 5.8(b) shows the γ rays in coincidence with the 6010-keV peak. This correlation results in the same peaks observed in Figure 5.8(a). These two spectra confirm that the γ-ray transitions are associated with the the decay of the ^{171}Ir isomeric state irrespective of the true origin of the 6010-keV α peak. There are sufficient statistics in decay correlated γ-ray spectra to create a tagged γ-γ coincidence matrix to deduce the order of these decays and to build a level scheme.

Figure 5.8(c) shows the γ rays in coincidence with the 5734-keV α decay from the ^{171}Ir ground state. The γ rays seen in this spectrum are different from those seen in the previous two spectra. The number of counts is also lower as a fusion evaporation reaction will populate yrast states that preferentially feed the $11/2^-$ yrast trap isomer. Gamma rays at 301 keV, 322 keV, 372 keV, 379 keV, 413 keV, 449 keV, 562 keV, 665 keV and 708 keV are assigned as members of cascades that feed the $1/2^+$ ground state on the basis of these recoil-decay correlations. There are insufficient statistics to allow a γ-γ coin-

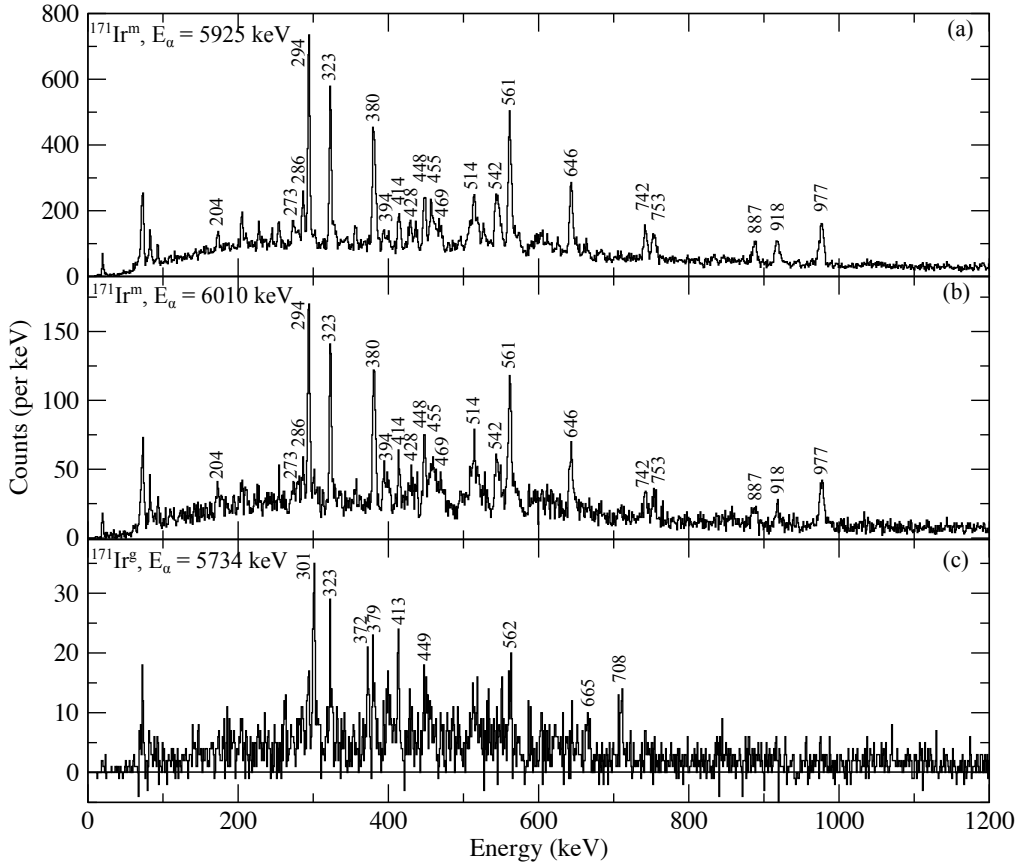

Figure 5.8: Spectra showing γ rays detected at the target position correlated with (a) the 5925-keV α particle, (b) the 6010-keV α decay and (c) the 5734-keV α decay.

cidence analysis and so it is impossible to order these γ rays within the level scheme.

5.3.3 RDT γ-ray Coincidence Analysis

A $\gamma - \gamma$ matrix was generated from γ-ray coincidences that satisfied specific RDT correlation conditions to associate events with ^{175}Au. Gamma rays were associated with recoil implantations in the GREAT DSSD detector that were followed within 500 ms by an α particle of decay energy between 6350 keV and 6470 keV detected in the same pixel. The γ rays measured at the target

position were associated with α decays at the focal plane using the methods described in section 4.4.2. Coincidences were limited to γ rays detected within 150 ns of each other. The level scheme deduced from the coincidence analysis is shown in Figure 5.9. All γ-ray spectra used to deduce the level scheme in this section were generated from this matrix.

5.3.4 Bands 1, 2 & 3 - Structures Associated with the $i_{13/2}$ Band and its Decay

Figure 5.10(a) shows γ rays in coincidence with the 294-keV transition. This spectrum comprises γ-ray transitions from the yrast band (band 1) and its decay paths to the $11/2^-$ isomer. These transitions were first observed by Kondev *et al.* in an experiment at the Argonne National Laboratory using the Gammasphere spectrometer in conjunction with FMA electromagnetic separator [45]. The yrast band was interpreted by Kondev *et al.* as the $\pi i_{13/2}$ intruder band.

Figure 5.10(b) shows a spectrum of γ rays in coincidence with the 977-keV transition. The yrast band is clearly visible in the spectrum but the 91-keV and 887-keV γ rays are absent. The absence of the 91-keV and 887-keV peaks indicates that these γ rays must feed out of the yrast band parallel to the 977-keV transition. This placement is supported in Figure 5.10(c), which shows γ rays in coincidence with the 887-keV transition. The 91-keV γ ray and the transitions in the yrast cascade are clearly in coincidence with the 887-keV γ ray while the 977-keV transition is not. These spectra confirm that the yrast band decays to the $11/2^-$ isomer via two decay branches; a direct 977-keV transition and a two-step decay via the 91-keV and 887-keV transitions as reported by Kondev *et al.* and shown in Figures 5.1 and 5.10.

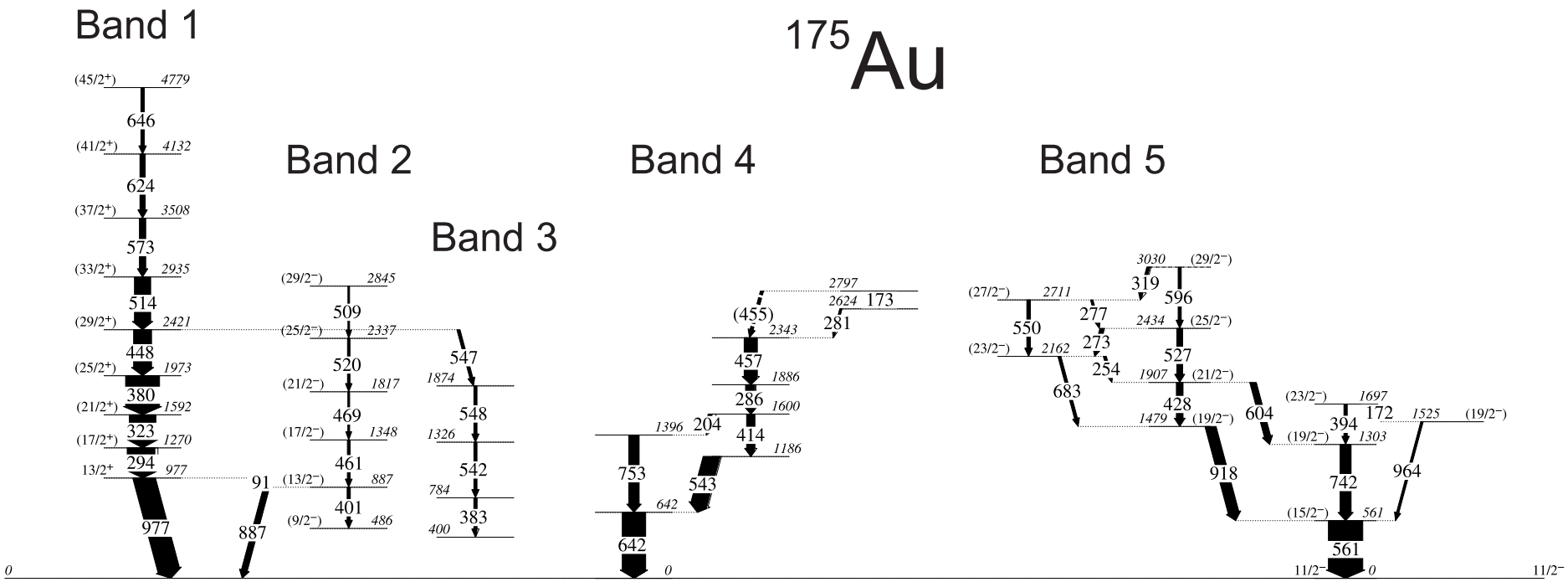

Figure 5.9: Level scheme deduced from this work for ^{175}Au. Bands 1 and 2 were partially known from previous work by Kondev *et al.* [45]. Bands 3, 4 and 5 are newly discovered in this work.

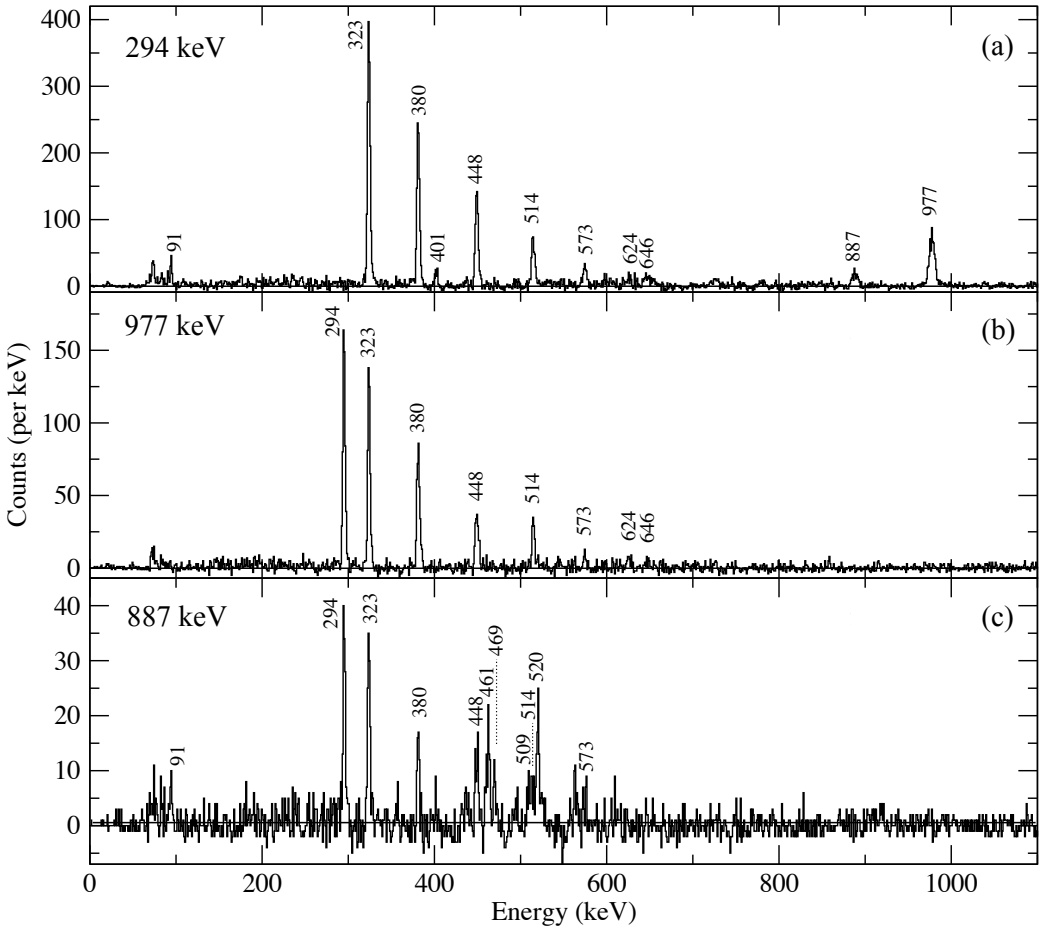

Figure 5.10: Gamma-ray spectra obtained from recoil-decay tagged $\gamma - \gamma$ coincidence matrix correlated with the isomer (E_α=6432 keV) α decay. (a) Gamma rays in coincidence with the 294-keV transition. (b) Gamma rays in coincidence with the 294-keV, 323-keV or 380-keV transitions. (c) Gamma rays in coincidence with the 887-keV transition.

The spectrum shown in Fig.5.10(c) shows several additional peaks that are not apparent in Fig 5.10(a) or 5.10(b). The 461-keV, 469-keV, 509-keV and 520-keV γ-ray transitions form a cascade (band 2) that is in coincidence with the 887-keV transition. This sequence is also in coincidence with a 401-keV transition. The 401-keV γ ray is also seen in coincidence with the yrast band in Figure 5.10(a), and band 2. The 401-keV transition is not in coincidence with either the 887-keV or the 977-keV γ rays implying that it forms part of the new cascade and lies parallel to the 886-keV transition. There are no

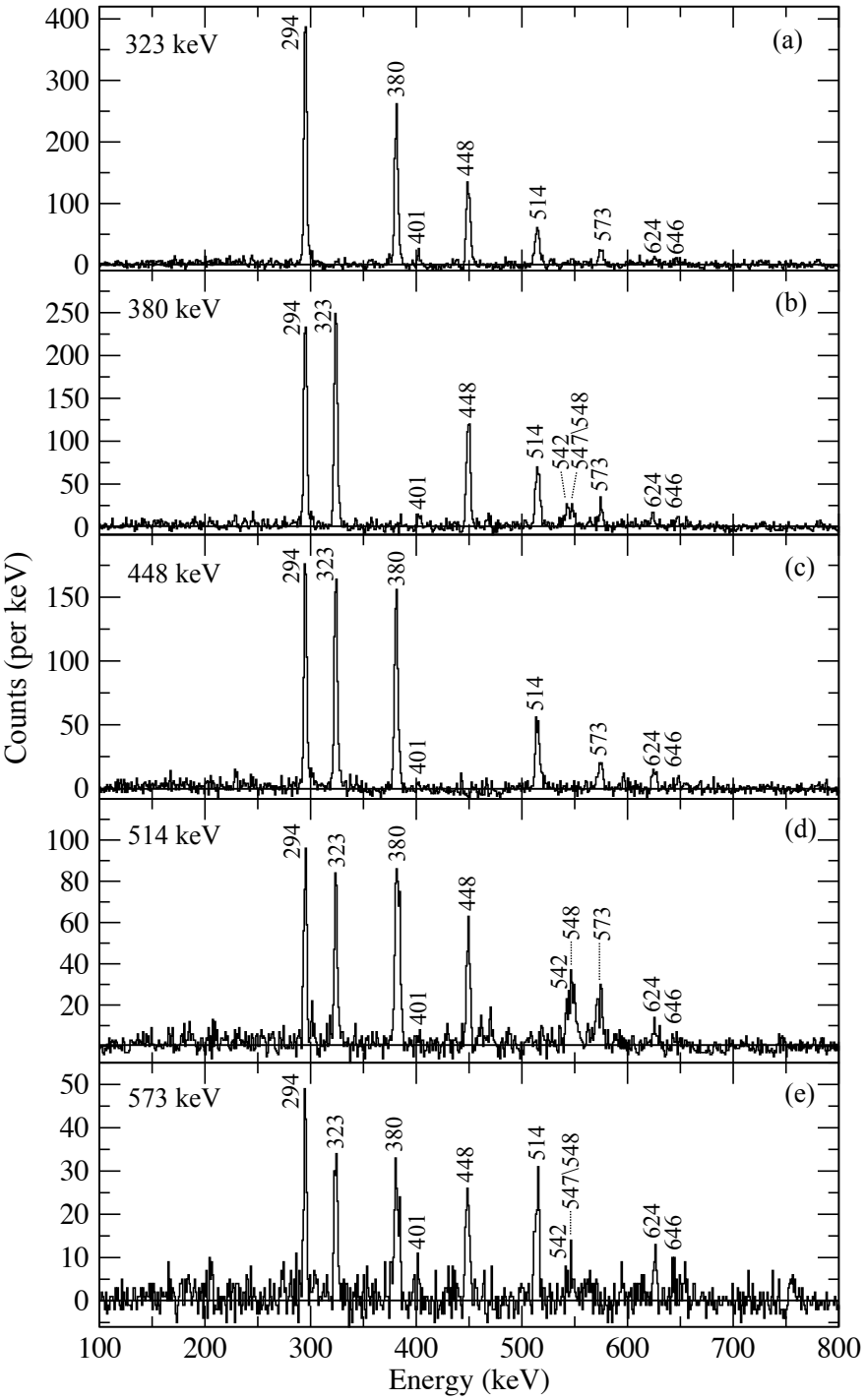

Figure 5.11: Gamma-ray spectra obtained from recoil-decay tagged $\gamma-\gamma$ coincidence matrix correlated with the isomer ($E_\alpha = 6432$ keV) α decay. Gamma rays in coincidence with γ-ray transitions at (a) 323 keV, (b) 380 keV, (c) 448 keV (d) 514 keV and (e) 573 keV.

discernible linking transitions from the state fed by the 401-keV transition to the $11/2^-$ isomer.

Figure 5.11 shows γ-ray spectra in coincidence with members of the $i_{13/2}$ yrast band. Coincidences with the 323-keV and 448-keV transitions, Fig. 5.11(a) and 5.11(c), show a narrow peak at 380 keV. However, when coincidences are demanded with the 514-keV and 573-keV transitions shown in Figure 5.11(d) and 5.11(e), the peak at 380 keV becomes broader suggesting the presence of a doublet at $\approx$ 380 keV. It is clear from Figure 5.11(b) that the 380-keV transition itself is not a self-coincident doublet.

Figures 5.11(b), 5.11(d)and 5.11(e) display additional γ rays with transition energies of 383 keV, 542 keV and 548 keV. The 547-keV transition is a self-coincident doublet and the proposed placement of these γ rays can be seen in Figure 5.9. The 547-keV γ ray has been tentatively assigned as a decay out of the yrast band, and the remaining γ rays are ordered into a new band (band 3) with the lowest-energy 383-keV transition at the bottom.

5.3.5 Band 4

The sequence of γ rays labelled as band 4 in Figure 5.9 is assigned to feed the α-decaying $11/2^-$ isomer on the basis of recoil-mother-daughter decay correlations. Figure 5.12 shows typical γ-ray coincidence spectra. The γ-ray coincidences in these spectra suggest that the intense 642-keV transition is the lowest-lying transition in this structure. It is also apparent that there are two parallel branches that feed the level depopulated by the 642-keV transition. One branch comprises the 204-keV and 753-keV transitions while the other features the 414-keV and 543-keV γ rays. Figure 5.12 shows γ rays at 173 keV, 281 keV, 286 keV and 457 keV that are common to both spectra. These transitions are ordered on the basis of coincidence relationships and

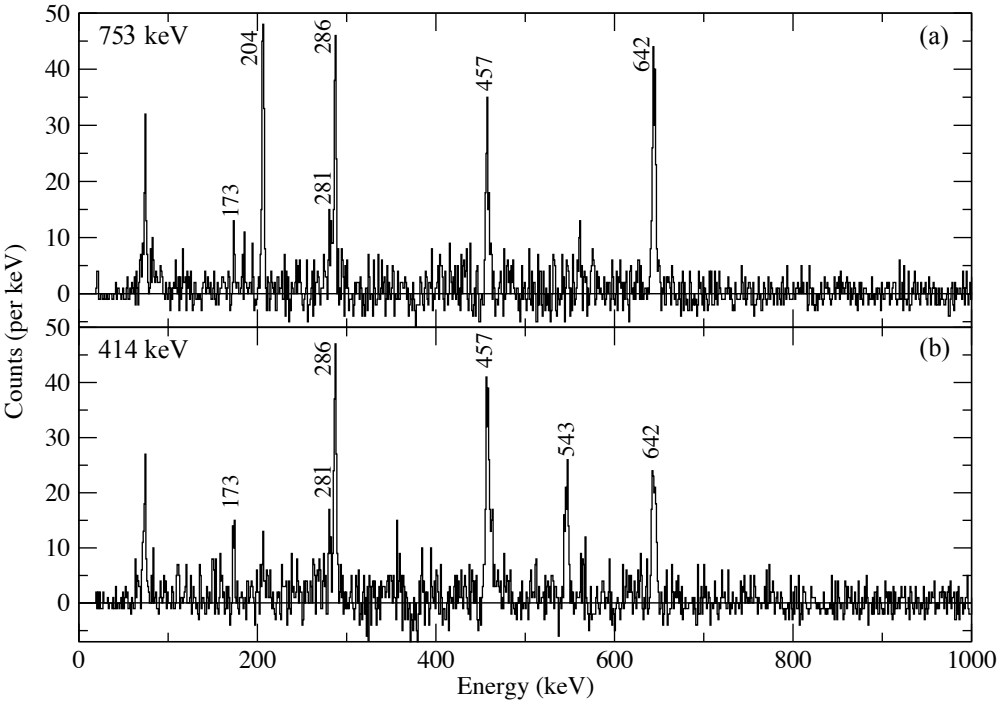

Figure 5.12: Gamma-ray spectra obtained from recoil-decay tagged $\gamma - \gamma$ coincidence matrix correlated with the isomer ($E_\alpha = 6432$ keV) α decay. (a) Gamma rays in coincidence with the 753-keV transition. (b) Gamma rays in coincidence with the 414-keV transition.

relative intensities and extend the excited states in this structure to high spin.

5.3.6 Band 5 and its Decay Path

Figure 5.13 shows the γ-ray coincidence spectra displaying transitions related to the structures labelled as band 5 in Figure 5.9. Figure 5.13(a) shows γ rays which are in coincidence with the 561-keV γ ray. This coincidence spectrum is rather complicated with many transitions noted across a broad energy range. There are three prominent high-energy transitions at 742 keV, 918 keV and 964 keV that feed the level depopulated by the 561-keV transition, in parallel.

Figure 5.13(b) shows γ-ray coincidences with the 918-keV transition. The 918-keV transition appears to decay out of the lowest observed state in a

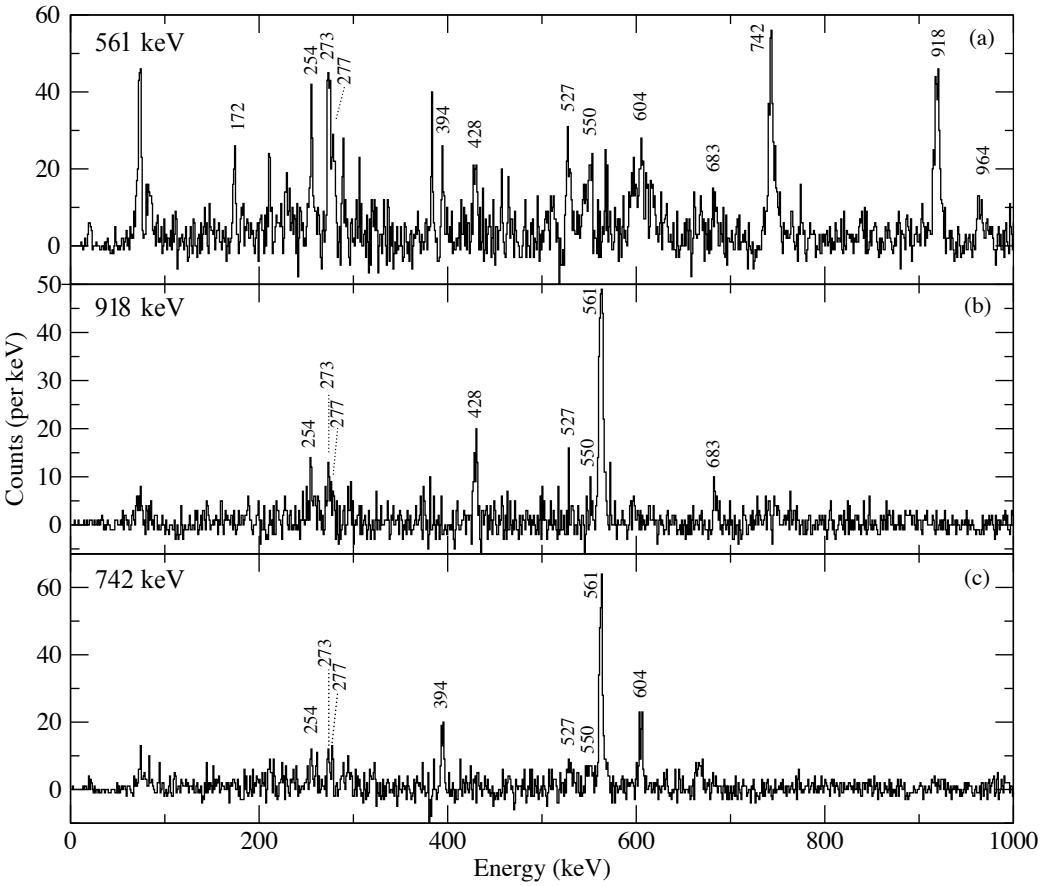

Figure 5.13: Gamma-ray spectra obtained from recoil-decay tagged $\gamma - \gamma$ coincidence matrix correlated with the isomer (E_α=6432 keV) α decay. (a) Gamma rays in coincidence with the 561-keV transition. (b) Gamma rays in coincidence with the 918-keV transition. (c) Gamma rays in coincidence with the 742-keV transition.

strongly coupled band. Figure 5.13(c) shows γ rays in coincidence with the 742-keV transition, which is in coincidence with some members of the same strongly coupled band. The 604-keV and 742-keV transitions form a parallel decay path from this band. It is apparent from Figures 5.13(b) and 5.13(c) that the 172-keV and 964-keV γ rays are absent indicating a third parallel decay path to the 561-keV transition.

5.4 Discussion

The proton-unbound nucleus ^{175}Au consists of 79 protons and 96 neutrons. The Nilsson diagram for protons in the Z $\approx$ 82 region is shown in figure 5.14. The proton Fermi surface lies close to the $3s_{1/2}$, $2d_{3/2}$ and $1h_{11/2}$ orbitals below the $Z = 82$ shell gap. The unpaired proton can be excited into vacant orbitals near the Fermi surface thereby forcing the nucleus to adopt differently deformed coexisting shapes. The Nilsson diagram shows that the odd proton can be excited into the $1h_{9/2}$, $1i_{13/2}$ and $2f_{7/2}$ orbitals above the shell gap. The odd proton or proton hole can also couple to excitations of the respective Pt and Hg cores thereby providing another mechanism for stabilising coexisting prolate and oblate shapes.

The neutron-deficient Au isotopes are expected to have $1/2^+$ ground states based on an odd proton occupying the $3s_{1/2}$ orbital. Recent laser spectroscopy measurements at the CERN-ISOLDE facility have established the ground-state spin and parity to be $1/2^+$ for ^{177}Au [59]. Kondev *et al.* noted that the configuration of the ground states in ^{173,175,177}Au are significantly different from those observed in ^{179,181,183,185}Au [60][61][54], in which ground states are assigned $I^\pi = 5/2^-$, built on a $\pi h_{9/2}$ intruder configuration. This was interpreted as a shape change within the Au isotopic chain similar to that seen in the even-even Pt core isotopes [49, 62, 63, 64].

The low-lying $11/2^-$ state is an yrast trap isomer based on an odd proton in the $1h_{11/2}$ state. Kondev *et al.* assigned the $11/2^-[505]$ Nilsson configuration to the isomer. The excitation energy is estimated to be 176(60) keV based on extrapolations of the proton and α-decay energy systematics reported in reference [52]. This estimate fits with the excitation energy trends for the $\pi h_{11/2}^{-1}$ band-head configuration, which remains almost constant as a function

of neutron number for the neutron-deficient isotopes. Figure 5.15 illustrates these trends across this region of gold.

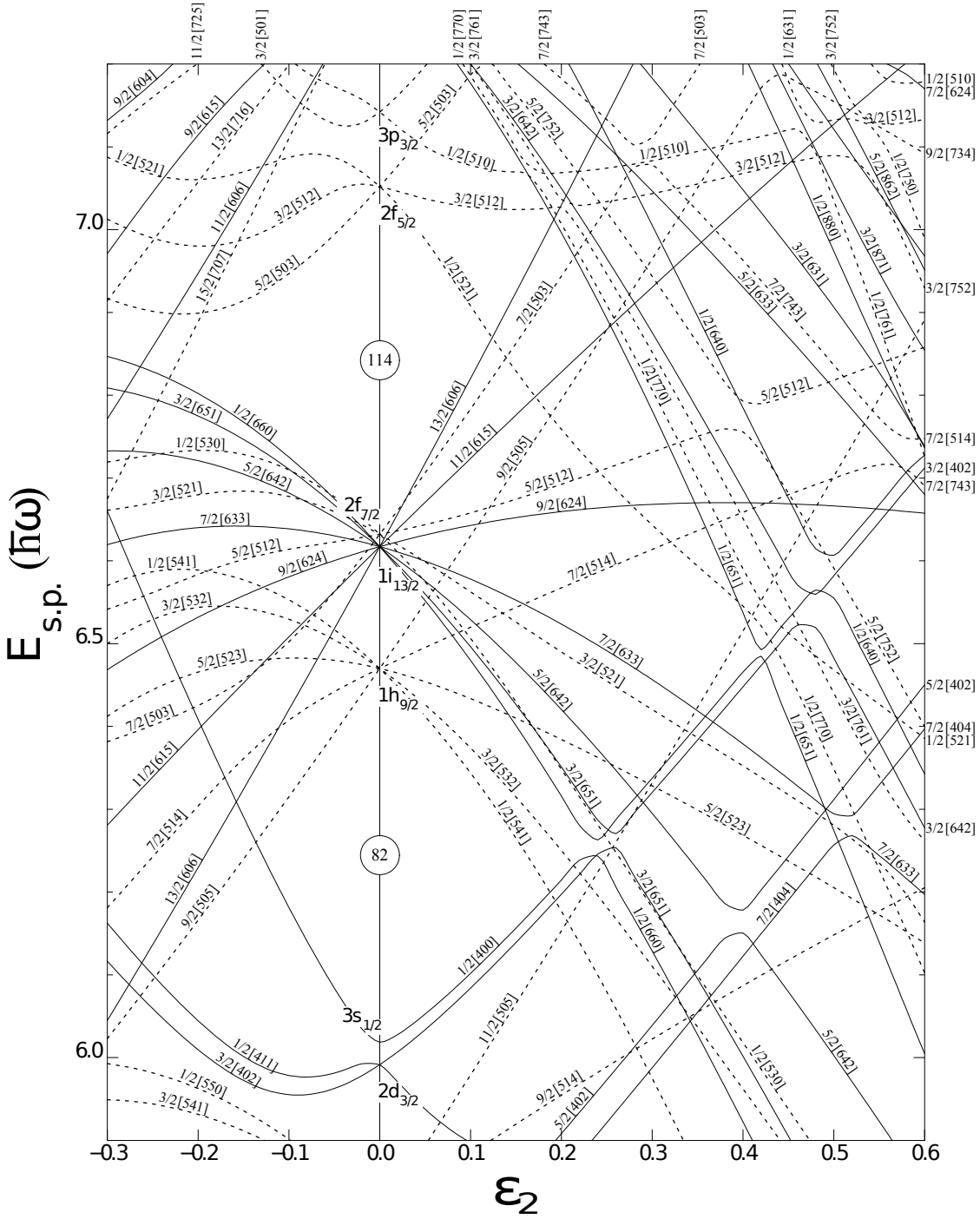

Figure 5.14: A Nilsson diagram showing single particle proton states in the $Z = 82$ region. The diagram shows how the degeneracy of the spherical shell model states is relieved as function of the quadrupole deformation ϵ_2.

5.4.1 Band 1 - The $\pi i_{13/2}$ Intruder Configuration.

Kondev *et al.* assigned band 1 in ^{175}Au to be a prolate $i_{13/2}$ proton intruder band that feeds an oblate $13/2^+$ band head. Further information concerning the shapes of these configurations was obtained in lifetime measurements of the low-lying states at the University of Jyväskylä by Watkins *et al.* This study used the Köln plunger device in conjunction with the recoil-decay tagging technique [50] to provide evidence to support the configuration assignments made by Kondev *et al.* and confirmed the presence of at least three coexisting nuclear shapes in ^{175}Au. Figure 5.2 illustrates the three observed shapes.

The high quadrupole moments extracted for the $25/2^+$ and $21/2^+$ states indicate a collective structure similar to those expected for similar structures observed in nearby nuclei [46]. Indeed, these data are consistent with the assignment of a prolate band based on an odd proton occupying a high-j, $i_{13/2}$ orbital as proposed by Kondev *et al.* [45]. Watkins *et al.* established that the $17/2^+$ state has a longer lifetime indicating a decrease in collectivity and a relatively low quadrupole moment. This was interpreted as arising from a change of shape from the prolate band to an oblate band-head configuration. A similar drop in collectivity in nearby ^{188}Pb and ^{180,182}Hg nuclei, has been interpreted as an intrinsic structural change from a prolate shape at higher spin to an oblate-deformed band [65][66][67]. Although only a limit for the lifetime of the $13/2^+$ could be established, the long lifetime of this state was interpreted as another hindered transition to a spherical $11/2^-$ configuration. In the work of Kondev *et al.*, the 977-keV transition from the $13/2^+$ state was measured to be an E1 transition with a reduced transition probability consistent with a non-collective single-proton transition from a mixed $13/2^+$ state to a near spherical $11/2^-$ state.

The excitation energy of the $13/2^+$ state is estimated to be 1153(60) keV

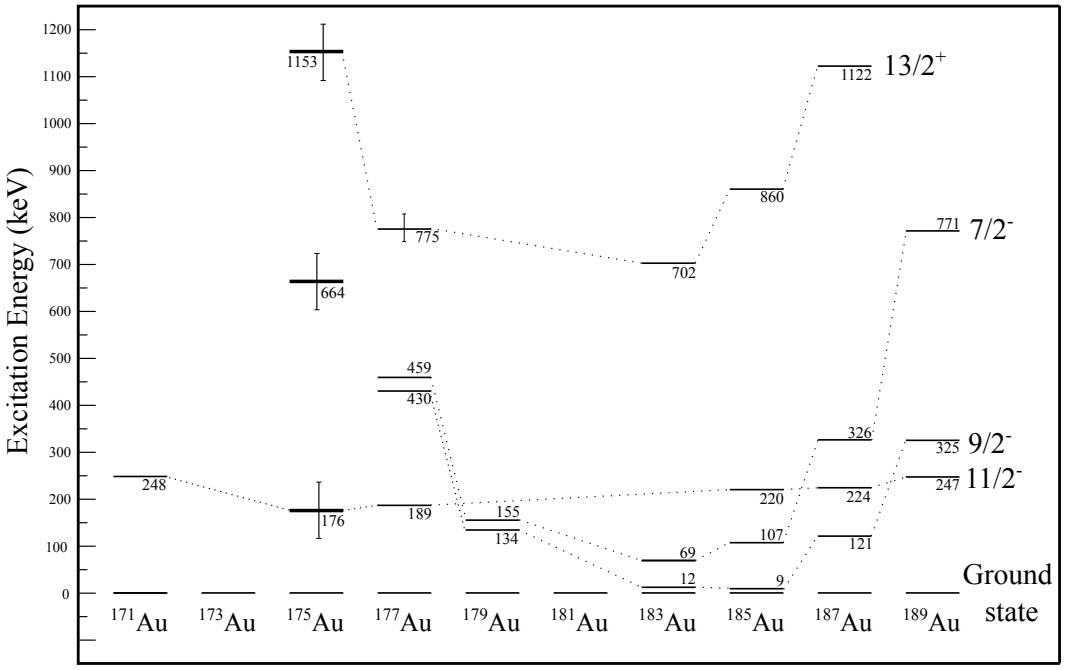

Figure 5.15: Variation of intruder band heads in the Au isotopes as a function of mass number. The measurements for ^{175}Au also include an estimate of 176(60) keV for the excitation energy of the $11/2^-$ isomer extrapolated from proton and α decay measurements [52].

assuming the $\pi h_{11/2}$ isomer excitation energy state extrapolated from decay systematics is 176(60) keV. Figure 5.15 shows the excitation of intruder band heads across the odd-A Au isotopes. The estimate for the $13/2^+$ state fits well with the smoothly varying parabola for $i_{13/2}$ states relative to the ground states across the Au isotopes. Although relative excitation energies are not known below ^{183}Au, a parabolic fit to these data suggests that the $\pi i_{13/2}$ configuration reaches a minimum at $N = 102$.

5.4.2 Bands 2 & 3: Candidates for the Negative-parity Intruder Bands.

If it is assumed that the 401-keV γ ray is an in-band transition of stretched E2 multipolarity, the spin and parity of the final state would be $9/2^-$. This could

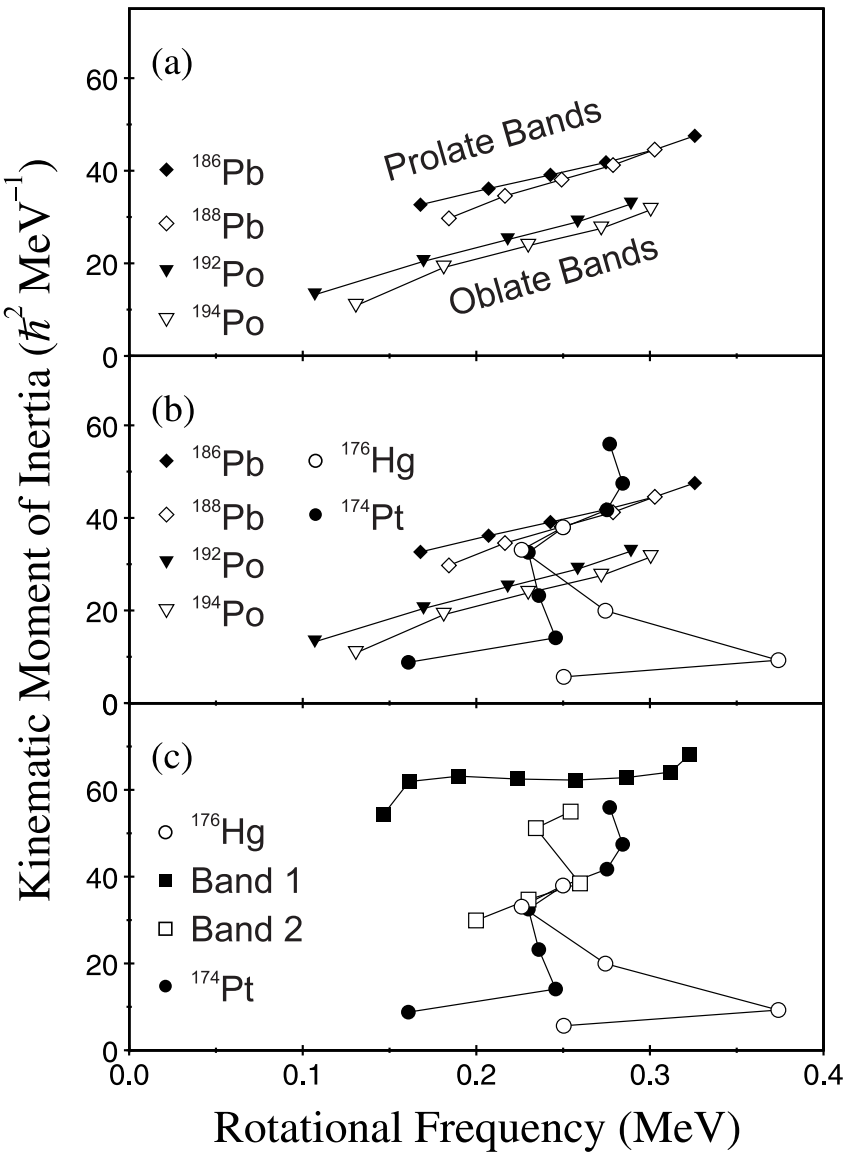

Figure 5.16: Kinematic moments of inertia ($\mathcal{J}^{(1)}$) as a function of rotational frequency. (a) Typical $\mathcal{J}^{(1)}$ values in this mass region for prolate bands exemplified by ^{186}Pb and ^{188}Pb and oblate bands exemplified by ^{192}Po and ^{194}Po. (b) Comparison of the $\mathcal{J}^{(1)}$ values for the oblate and prolate reference bands with the ^{174}Pt and ^{176}Hg cores. (c) Comparison of the $\mathcal{J}^{(1)}$ values for the intruder bands (bands 1 & 2) in ^{175}Au with the ^{174}Pt and ^{176}Hg core values.

be a candidate for the band head of the $\pi h_{9/2}$ intruder configuration. No γ-ray transitions have been identified that connect this level to the $11/2^-$ isomer. However, it is noted that the band-head configurations of the negative-parity

$\pi h_{9/2}$ and $\pi f_{7/2}$ intruder bands in the heavier neighbouring odd-A isotope ^{177}Au are short-lived isomeric states. Hence, short-lived isomeric band heads are possible and depopulating γ rays may decay in flight beyond JUROGAM and before GREAT thereby avoiding detection.

The excitation energy of the state fed by the 401-keV transition is 485 keV relative to the $11/2^-$ isomer. If the $11/2^-$ isomer has a excitation energy of 179(60) keV then the excitation energy of this state relative to the ground state would be 664(60) keV. This result would fit into the smooth parabolic trend of the $\pi h_{9/2}$ band head energies as a function of neutron number established for the Au isotopes above the neutron mid shell. Therefore band 2 is tentatively assigned to be the prolate $\pi h_{9/2}$ (1p-4h) intruder configuration.

Band 3 is a decay branch from the $29/2^+$ state in band 1. A complete decay path to the $11/2^-$ state was not identified however the lowest observed state is at an excitation energy of 400 keV relative to the $11/2^-$ isomer. There are too few transitions in this band and no information on their multipolarity to make a definitive configuration assignment for this structure. However, the lower average deformation of ^{175}Au ($N = 96$) compared with the heavier isotopes would favour the mixed $\pi f_{7/2}/\pi h_{9/2}$ negative-parity orbitals. Indeed, the $\pi f_{7/2}$ and $\pi h_{9/2}$ intruders already have lower excitation energies than the positive-parity $\pi i_{13/2}$ intruder in heavier isotopes, ^{177}Au and ^{179}Au. It is possible to speculate that this structure might be another negative-parity intruder band such as the $\pi f_{7/2}$ configuration.

The level scheme can be used to extract kinematic moments of inertia, $\mathcal{J}^{(1)}$, which can provide information indicative of deformation. Figure 5.16 compares the kinematic moments of inertia for prolate bands in ^{186}Pb and ^{188}Pb and oblate bands in ^{192}Po and ^{194}Po. These bands provide a reference for comparison with the intruder bands in ^{175}Au and their underlying cores.

The bands in ^{175}Au can be considered as a proton coupled to the ^{174}Pt core or a proton hole coupled to a ^{176}Hg core. Figure 5.16(b) compares the cores to these reference bands shown in Fig. 5.16(a). Both cores have oblate ground states that are crossed by a prolate band at low spin. The core configurations are prolate at spins $I \geq 6$. Figure 5.16(c) shows the kinematic moments of inertia of the intruder bands in ^{175}Au with those of their core configurations. Band 1 has the highest moment of inertia characteristic of a well-deformed prolate shape, which is consistent with the expectations for the $\pi i_{13/2}$ configuration. Band 2 has a kinematic moment of inertia that is very similar to the moments extracted for the prolate references, which supports the intruder assignment for this band.

5.4.3 The Hole States: Band 4.

The sequence labelled band 4 does not have an analogous structure in the heavier neighbouring odd-A isotope, ^{177}Au. Band 4 bears a remarkable similarity to the low-lying excited states of the core ^{176}Hg. Figure 5.17 shows band 4 in ^{175}Au alongside the analogous structure in ^{177}Au for comparison. This suggests that band 4 is based on a proton-hole configuration that couples to the ^{176}Hg core. The ^{176}Hg core is anticipated to have an oblate deformation at low spin, which is crossed by a deformed $2p$-$4h$ prolate intruder configuration at $I \sim 6\hbar$. The similarity of the level schemes indicates that the odd proton hole must be decoupled from the core, which is indicative of a weakly deformed core and/or the odd-proton hole occupying a low-Ω orbital.

It may be possible to promote a proton from the $\pi h_{11/2}$ ($\Omega = 9/2$) orbital to form a coupled pair in the $\pi h_{11/2}$ ($\Omega = 11/2$) orbital. This would leave a hole in the $\pi^{-1} h_{11/2}$ ($\Omega = 9/2$) state that could couple to the excitations of the ^{176}Hg core. This would suggest the 642-keV and 753-keV transitions are

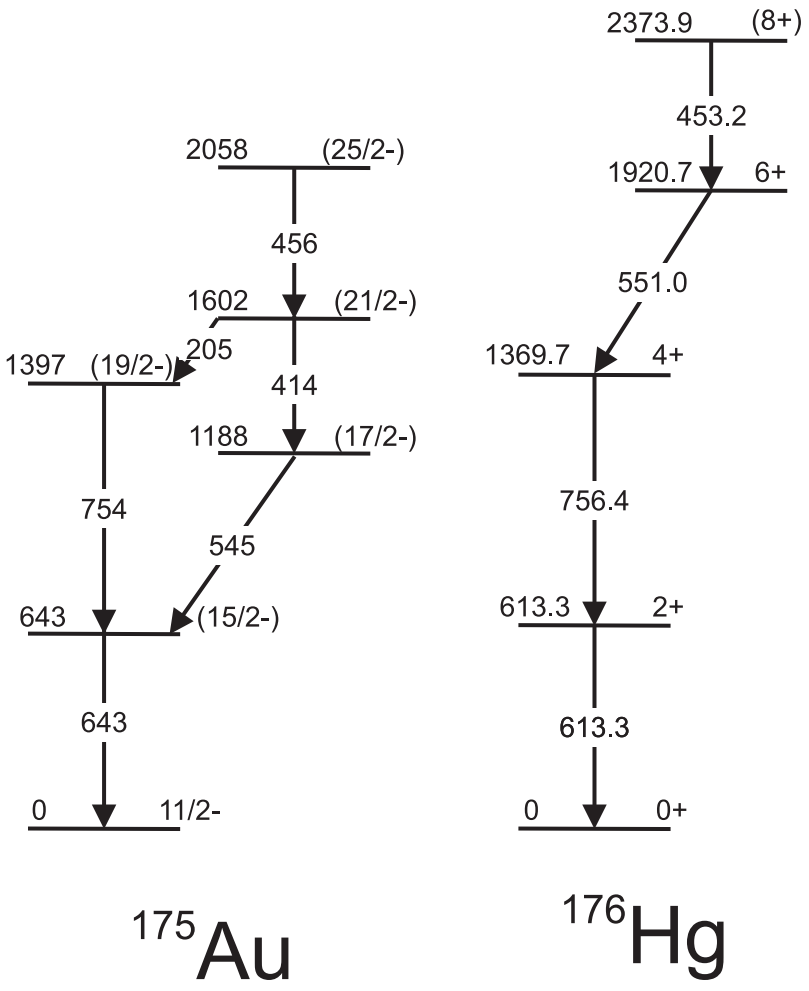

Figure 5.17: A comparison of levels associated with band 4 in ^{175}Au and the yrast band in the neighbouring even-even core ^{176}Hg.

associated with the $\pi h_{11/2}^{-1}$ $[\Omega = 9/2] \otimes^{176}\mathrm{Hg}_{[0+,2+]}$ oblate configuration, which, when looking at the Nilsson diagram, is crossed at higher spins by the $\pi h_{11/2}^{-1}$ $[\Omega = 9/2] \otimes^{176}$Hg prolate configuration based on a $1p$-$4h$ excitation.

It is also possible that band 4 might be a more exotic structure formed by coupling the $\pi^{-1}h_{11/2}$ hole to a multiparticle excitation. For example, a similar pattern of γ rays is observed in ^{191}Au based on the $31/2^+$ isomer based on the $\pi^{-1}h_{11/2} \otimes \nu^{-1}i_{13/2}\nu^{-1}h_{9/2}$ configuration [68].

5.4.4 The Holes States: Band 5.

The structures labelled band 5 in Figure 5.9 comprise a strongly coupled band and its associated decay paths to the α-decaying $11/2^-$ isomer. Strongly coupled bands are observed in several heavier Au isotopes but either have few or no transitions linking them to the low-spin level schemes resulting in indeterminate spins and excitation energies.

The strongly coupled band in ^{175}Au is observed to decay to the $11/2^-$ isomer via two decay paths. There is a two-step decay from the lowest observed level in the strongly coupled band via the 918-keV and 561-keV γ rays. A further three-step decay path proceeds from a higher-spin state via the 604-keV, 742-keV and 561-keV transitions. The 561-keV transition is common to both decay paths and is assigned to feed the $11/2^-$ isomer directly.

The strongly coupled band in ^{175}Au has a number of remarkable similarities to the band in ^{177}Au shown in Figure 5.18. The case of ^{177}Au is the best characterised strongly coupled band below the neutron midshell. In a recent recoil-decay tagging study [56], the strongly coupled band in ^{177}Au was observed to high spin and linked to the α-decaying $11/2^-$ isomer via several well-defined decay paths. The 561-keV γ-ray transition in ^{175}Au is assumed to be analogous to the transitions at 521 keV and 525 keV in ^{177}Au, which were assigned to be a configuration formed by coupling the $1h_{11/2}$ proton holes to the weakly oblate Hg core. The assignation in ^{177}Au was made on the basis of similarities with the 558 keV ($2_1^+ \rightarrow 0_1^+$) transition energy in ^{178}Hg.

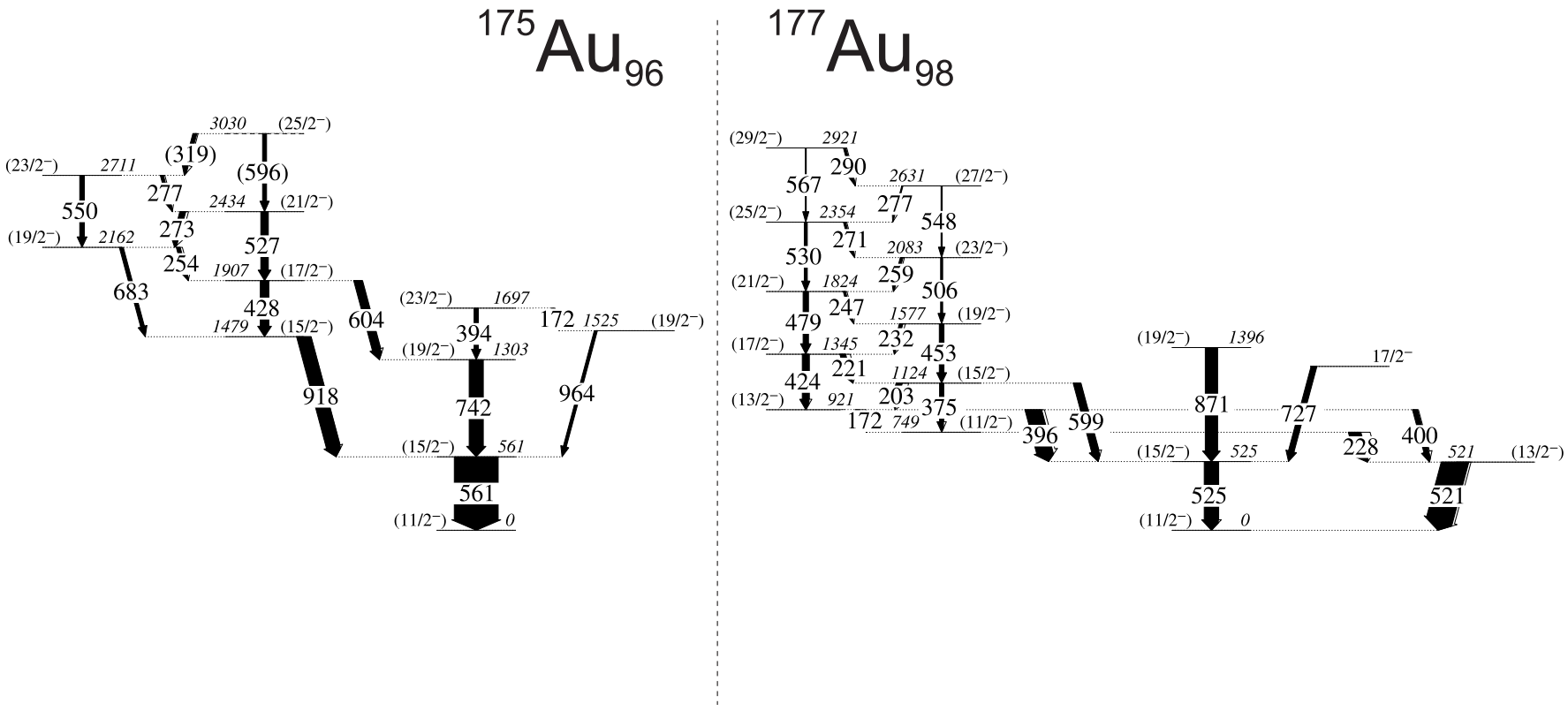

Figure 5.18: A comparison of the strongly coupled bands in ^{175}Au and ^{177}Au. The level scheme for ^{177}Au is reproduced from reference [55].

The level depopulated by the 561-keV transition is fed by three high-energy transitions at 742 keV, 918 keV and 964 keV. This is a similar feeding pattern to that observed in the heavier isotopes where high-energy γ rays depopulating the $17/2^-$ and $19/2^-$ weakly deformed states feed the $15/2^-$ state intensely. Multipolarities could not be extracted for these transitions experimentally and so the 561-keV transition is assigned a spin and parity of $15/2^-$ while the 742-keV and 964-keV transitions are assumed to be the $19/2^-$ and $17/2^-$ levels, respectively, on the basis of similarities with structures in the heavier Au isotopes.

The $15/2^-$ state is assigned to be $1h_{11/2}\otimes^{176}\mathrm{Hg}(2_1^+)$ configuration. The level excitation energies for the $1h_{11/2}\otimes^{A+1}\mathrm{Hg}$ configurations are established from beyond the proton drip line to the line of stability and vary smoothly as a function of neutron number. The higher transition energy of the $15/2^-$ state relative the $11/2^-$ isomer in ^{175}Au reflects the lower deformation of the ^{176}Hg core, which is closer to the $N = 82$ closed shell. This is also indicated by the higher $2_1^+ \rightarrow 0_1^+$ transition energy in ^{176}Hg (613 keV) compared with the heavier isotopes.

The strongly coupled band must be formed by coupling the odd proton or proton hole in a deformation-aligned orbital to an excited configuration in the core. Figure 5.19(a) compares the variation of γ-ray transition energies as a function of the initial state angular momentum for the strongly coupled band in ^{175}Au with its ^{176}Hg and ^{174}Pt cores. The ^{176}Hg core is interpreted as having an oblate shape at low spin that is crossed at $I \sim 6\hbar$ by a prolate $2p$-$4h$ intruder configuration. The ^{174}Pt core has a mixed yrast structure at low spin and becomes a well-deformed prolate configuration at higher spins. The high-spin prolate configurations for both cores are degenerate. The decay sequence from the strongly coupled band to the $11/2^-$ isomer suggests that the

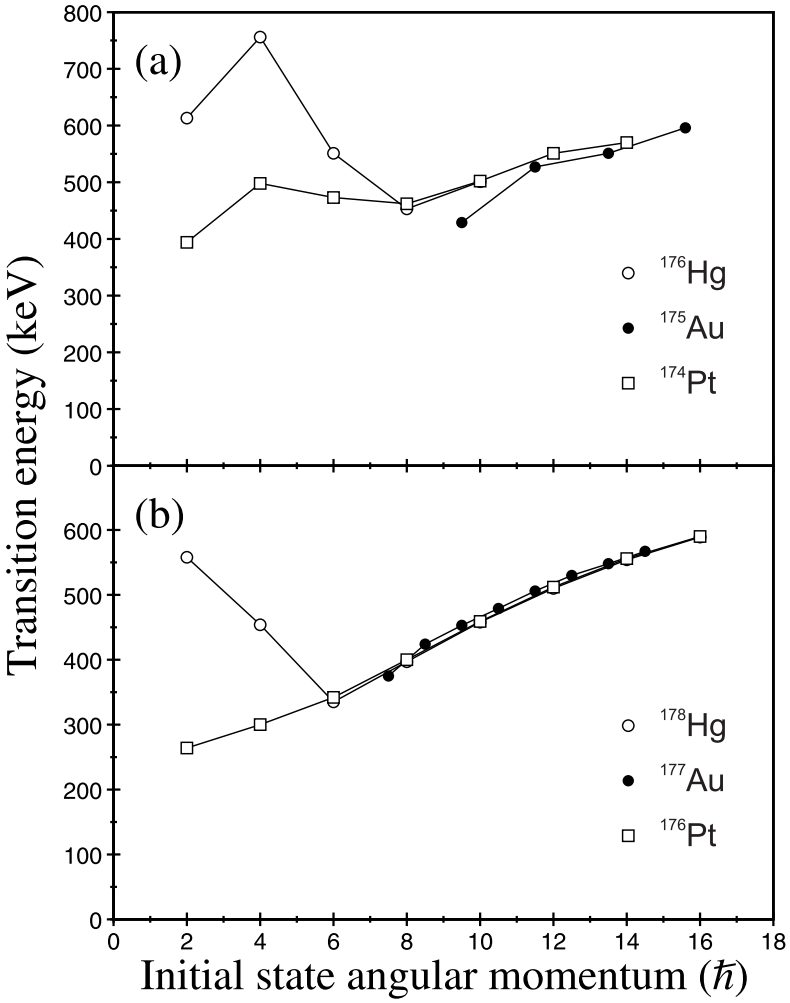

Figure 5.19: Variation of γ-ray transition energy as a function of initial state angular momentum for the strongly coupled bands in the Au isotopes and their respective cores.

lowest observed state is unlikely to be the excited $11/2^-$ band head. If the 918-keV transition is assigned to be an unstretched E2 transition that de-excites a $15/2^-$ level, the strongly coupled in ^{175}Au band close to zero alignment relative to the core configurations. Figure 5.19(b) compares the variation of γ-ray transition energies as a function of the initial state angular momentum for the strongly coupled band in ^{177}Au with its cores. A similar behaviour for ^{177}Au can be seen to that in ^{175}Au assuming the lowest observed level in the

strongly coupled band is the $11/2^-$ band head. The strongly coupled bands in ^{175}Au and ^{177}Au are likely to have the same origin and are assigned to be formed by coupling $1h_{11/2}$ proton hole to the ^{176}Hg(0_2^+) intruder configuration. The small signature splitting and close overlap to the cores are indicative of a well-deformed prolate shape.

Chapter 6

A New Isomeric State in ^{179}Au

Excited states in the neutron-deficient nucleus ^{179}Au have been populated following the ^{100}Ru(^{82}Kr, p2n) reaction in an experiment performed at the University of Jyväskylä Accelerator Laboratory. The SAGE spectrometer detected γ rays and conversion electrons emitted promptly at the target position. Transitions were correlated with recoil implantations detected in the GREAT focal-plane spectrometer that were followed by the characteristic α decay of ^{179}Au using the recoil-decay tagging technique. Two new isomer-delayed γ rays have been identified and the isomer half-life has been measured to be $t_{1/2}$=262(20) ns. Structural assignments for the new isomer are discussed.

6.1 Motivation and Previous Studies

The neutron-deficient nucleus ^{179}Au was first discovered at the Lawrence Radiation Laboratory in 1968 by Siivola who assigned a 5848(5)-keV α decay to ^{179}Au and deduced the half life to be 7.2(0.5) s [69]. Mueller *et al.* made the first identification of excited states in ^{179}Au in 2004. The experiment used the ^{78}Kr(^{104}Ru,1p2n) and ^{90}Zr(^{104}Zr,1p) fusion-evaporation reactions at the Argonne Tandem Linac Accelerator System (ATLAS) [60]. Mueller *et al.* provided important insights into the high-spin structure of ^{179}Au and collected enough data to unambiguously assign γ rays with the characteristic ^{179}Au α decay using the recoil-decay tagging technique. Figure 6.1 shows the level scheme deduced in that work where the collective bands are labelled 1-4 to aid further discussion.

Mueller *et al.* assigned the yrast band, band 1, as a $\pi i_{13/2}$ intruder band due to its similarities with bands in odd-A Au isotopes between $175 \leqslant A \leqslant 187$ [45][54][70][61]. Additionally, the yrast bands in ^{181}Au, ^{183}Au and ^{185}Au are observed to decay to $13/2^-$ and $11/2^-$ levels in $\pi h_{9/2}$ and $\pi f_{7/2}$ configurations. Therefore the analogous states in ^{179}Au were assigned the same spin and parity. The two transitions feeding out of the bottom of the yrast band with energies 351 keV and 371 keV, labelled (1b) in figure 6.1, are unusual since similar transitions have not been observed in other Au nuclei. Mueller *et al.* suggested the possibility that the Coriolis coupling of the valence proton to the core is weakened and the $9/2^+$ state of the $\pi i_{13/2}$ is lowered in energy such that it is below the $13/2^+$ level. In this case the 371-keV γ ray is assigned as the decay from the $13/2^+$ band directly and the 351-keV γ ray from the $9/2^+$ state.

Mueller *et al.* concluded that the most likely spin and parity for the band head of band 2 in Figure 6.1 is $5/2^-$ based on correlations with the favoured

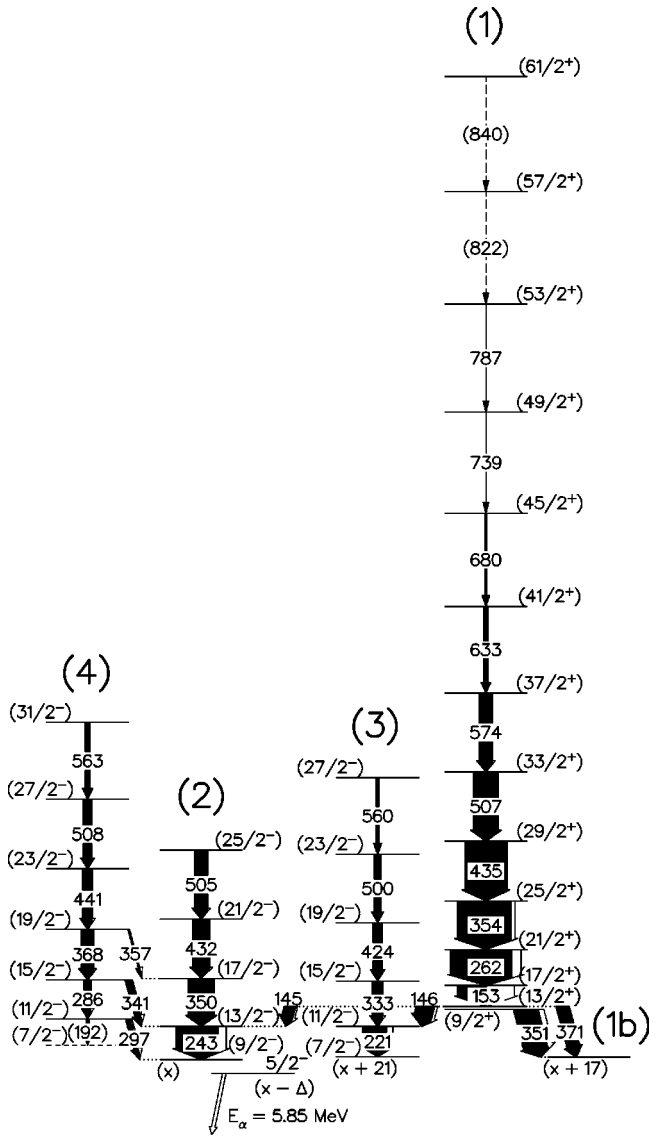

Figure 6.1: Level scheme for ^{179}Au reproduced from reference [60].

α decay to the $5/2^-$ state in the daughter nucleus ^{175}Ir. A transition between the $9/2^-$ and $5/2^-$ states in band 2 was not observed in that work, which was attributed to the small energy difference between the states. Bands 3 and 4 are interpreted as being based on mixed configurations of the $\pi h_{9/2}$ and $\pi f_{7/2}$ orbitals.

Figure 6.2 illustrates the outcome of a later study by Venhart *et al.* which

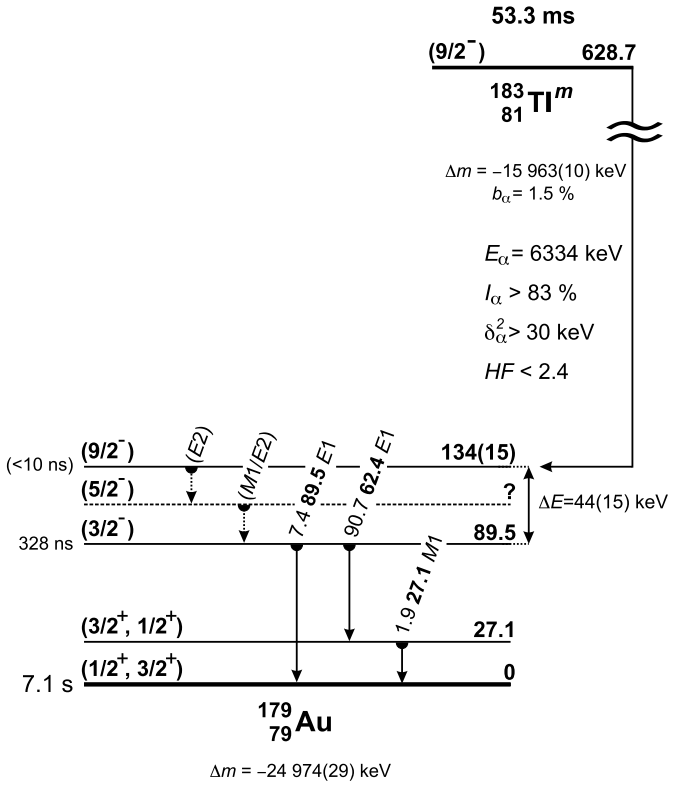

Figure 6.2: Isomeric transitions identified by Venhart *et al.* This figure is reproduced from reference [44]

investigated γ-ray transitions in ^{179}Au populated by the α decay of ^{183}Tl [44]. The unhindered α decay was assigned to connect the $9/2^-$ states in the parent and daughter nuclides.

The proposed $9/2^-$ isomeric state in the ^{179}Au daughter was deduced to have an unseen decay path to a $3/2^-$ isomer, which was measured to have a half life of 328 ns. Venhart *et al.* estimated the half-life of the $9/2^-$ isomer to be < 10 *ns* on the basis of the measured decay curve for the $3/2^-$ isomer. The isomer decays to the α-decaying $1/2^+$ ground state via a cascade of γ-ray transitions, which fixed the excitation energy of the $3/2^-$ isomer to be 89.5 keV.

The 89.5-keV transition connecting the $3/2^-$ isomer to the $1/2^+$ ground state was deduced to be an E1 transition by determining conversion coefficients

from X-ray yields and γ-ray intensities. A parallel decay path comprising the 27.1-keV and 62.4-keV transitions was also observed. The 27.1-keV γ ray was suggested to have an M1 multipolarity by comparing the experimental and simulated γ-ray intensities. The 62.4-keV transition has been assigned an E1 character by lifetime and parity considerations. The ground state and first excited states have been assigned as $\pi s_{1/2}^{-1}$ and $\pi d_{3/2}^{-1}$ configurations, although it is noted in reference [44] that it is impossible to establish the order of these two states.

6.2 The Experiment

This experiment was performed at the University of Jyväskylä Accelerator Laboratory where the K130 cyclotron accelerated a beam of ^{82}Kr ions to 352 MeV, which were then directed onto a ^{100}Ru target of nominal thickness 350 μg/cm^2 and 97.42% enrichment. A compound nucleus of ^{182}Hg was formed in the reaction and ^{179}Au was produced in an excited state via the $p2n$ evaporation channel. The reaction cross section was estimated to be $\approx$ 5 mb. Gamma rays emitted at the target position were detected by the SAGE γ-ray and electron spectrometer and the fusion products were transported via the RITU gas-filled spectrometer to the GREAT focal plane spectrometer [35]. RITU separated the reaction products (recoils), from unreacted beam and fission products. The recoils were then implanted into the GREAT DSSDs. Recoils were separated from any remaining unreacted beam by observing their energy loss in the GREAT multiwire proportional counter in conjunction with time of flight measurements. Total data readout (TDR) [37] was used and signals from all detectors were read out independently and analysed using the Grain software package [38].

6.3 Results

6.3.1 Recoil-decay Tagging Analysis

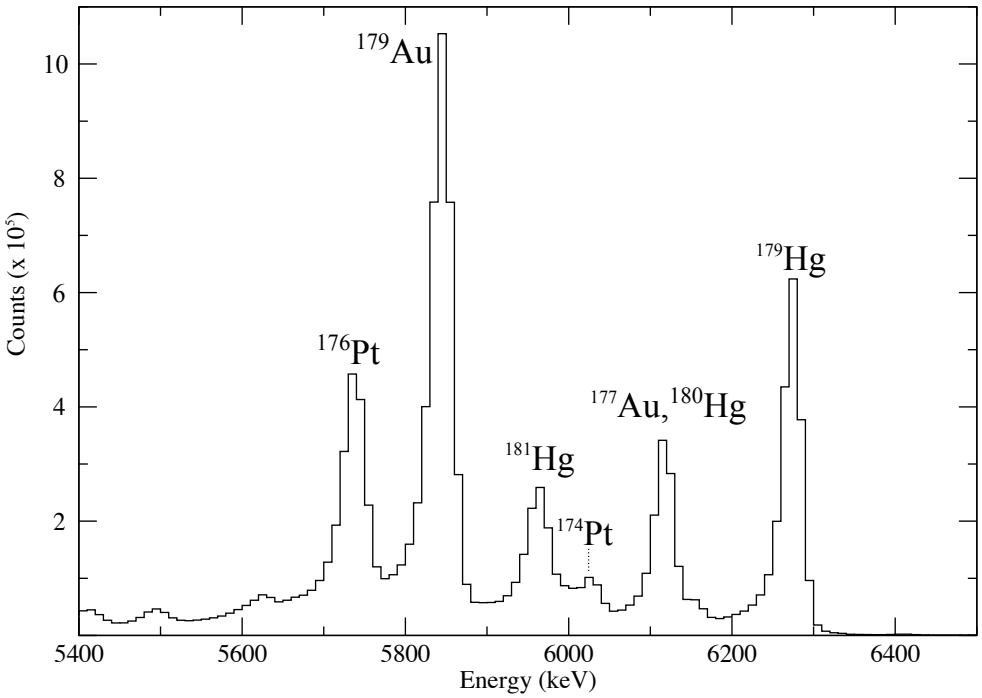

Figure 6.3: Decay particle spectrum collected with the GREAT DSSD detector and in anti-coincidence with the GREAT multiwire proportional counter. The spectrum shows radioactive decays occurring up to 14 s after a recoil implantation in the same DSSD pixel.

The RDT technique (described in section 4.4.3) is used to distinguish γ rays from specific reaction channels by reducing the large γ-ray background arising from the emissions of other fusion products and fission fragments. The RDT technique significantly reduces the level of background counts and due to the relatively high production of ^{179}Au in this experiment and the clear separation between α peaks shown in figure 6.3, the technique provided an excellent way to reveal γ rays belonging to ^{179}Au that were otherwise lost among the background. Some contamination will remain due to correlations with escaping α particles arising from the radioactive decays of the lighter Au

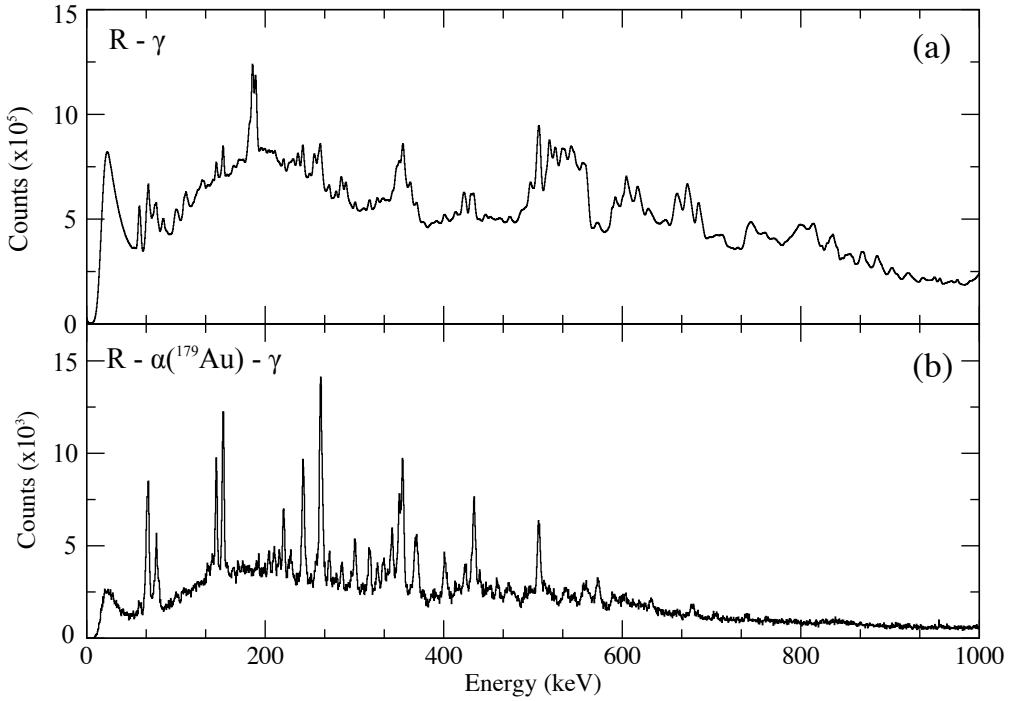

Figure 6.4: Spectra showing the effectiveness of the recoil-decay tagging technique. (a) A γ-ray spectrum measured at the target position and in delayed coincidence with implanted fusion products detected in the GREAT DSSD. (b) A γ-ray spectrum from the target position showing γ rays that are in delayed coincidence with recoil implantations followed by the characteristic α decay of ^{179}Au in the same pixel within 14 s. The yrast band of ^{179}Au is clearly seen.

isotopes and ^{180,181}Hg.

Figure 6.4 shows the effectiveness of the recoil-decay tagging technique. Figure 6.4(a) shows all γ rays in delayed coincidence with fusion products implanted in the GREAT DSSD. Figure 6.4(b) shows γ rays that are in delayed coincidence with recoil implantations followed by the characteristic α decay of ^{179}Au in the same pixel within 14 s. The correlation time is relatively long to accommodate the long α-decay half-life of 7.1 s. The spectrum in Figure 6.4(b) shows γ-ray transitions associated with the yrast band in ^{179}Au, which are only visible due to the reduction in γ-ray background arising from other channels..

A two-dimensional $\gamma - \gamma$ coincidence matrix was created from the recoil-decay correlated data. The γ rays had to be detected within 130 ns of each

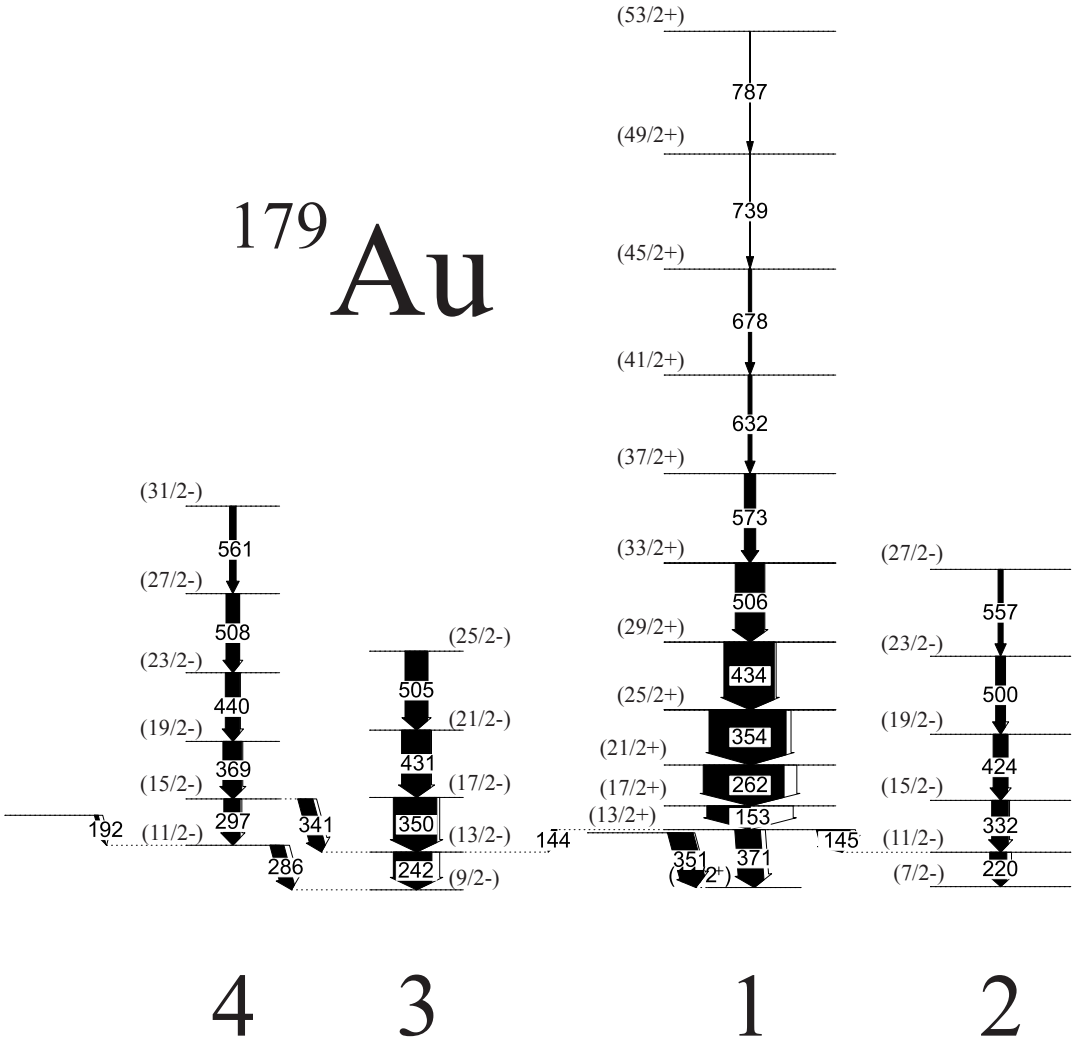

Figure 6.5: The level scheme for ^{179}Au deduced in this work. The width of the arrows is proportional to the measured intensity of the transition.

other to satisfy the coincidence condition and be incremented into the matrix. The level scheme deduced in this work is shown in Figure 6.5. The level scheme shows four rotational bands, which are labelled band 1 to band 4. The level scheme is in agreement with the previously known level scheme identified by Mueller *et al.* [60], which can be seen in Figure 6.1. A new 341-keV transition linking band 4 to band 3 and the position of the 192-keV γ ray has been revised on the basis of γ-ray coincidences. The logic of the level scheme will be described in the following section.

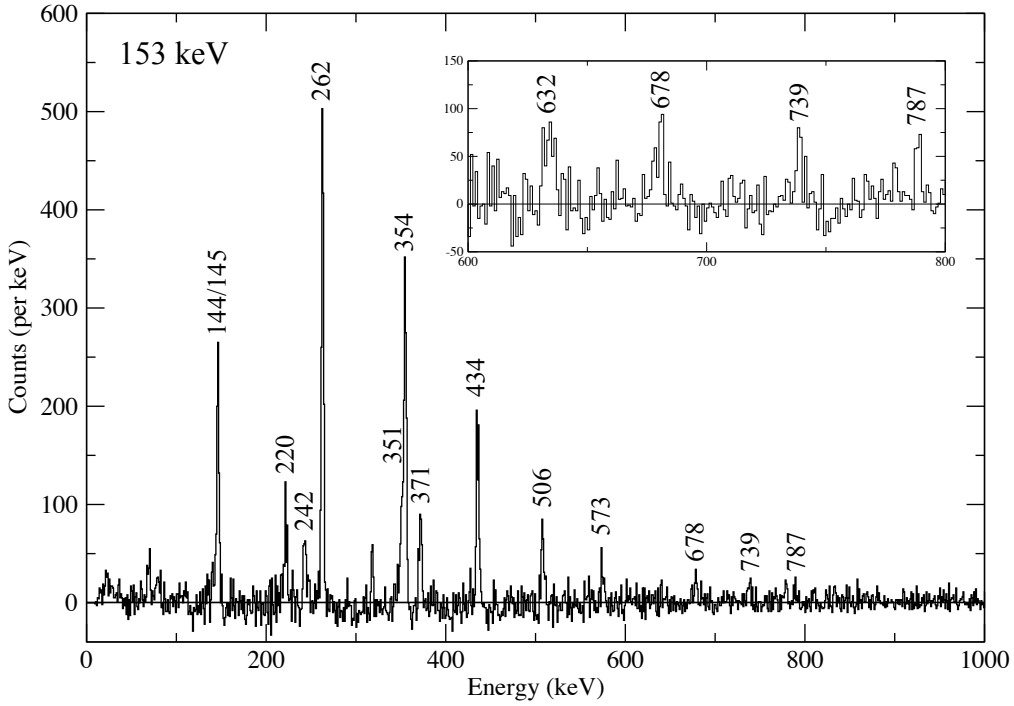

Figure 6.6: Gamma rays in coincidence with the 153-keV transition. The inset shows a γ-ray spectrum in coincidence with the 153-keV, 262-keV or 354-keV transitions to better illustrate the higher-energy transitions of band 1.

Figure 6.6 shows γ rays in coincidence with the 153-keV γ transition. This spectrum shows the γ rays that comprise the yrast band and its decay paths to lower-energy states. The inset in Figure 6.6 shows a γ-ray spectrum gated on the 153, 262-keV or 354-keV transitions to better show the higher energy decays in the yrast band. The state fed by the 153-keV transition was assigned a spin of $13/2^+$ by Mueller *et al.* based on systematic comparisons with band structures in the heavier odd-mass Au nuclei [60].

The decay out of the yrast band is fairly complicated since it involves four separate γ rays, two of which form a doublet. Figure 6.7 demonstrates that a peak at $\approx$ 144 keV is seen when demanding coincidences with both the 220-

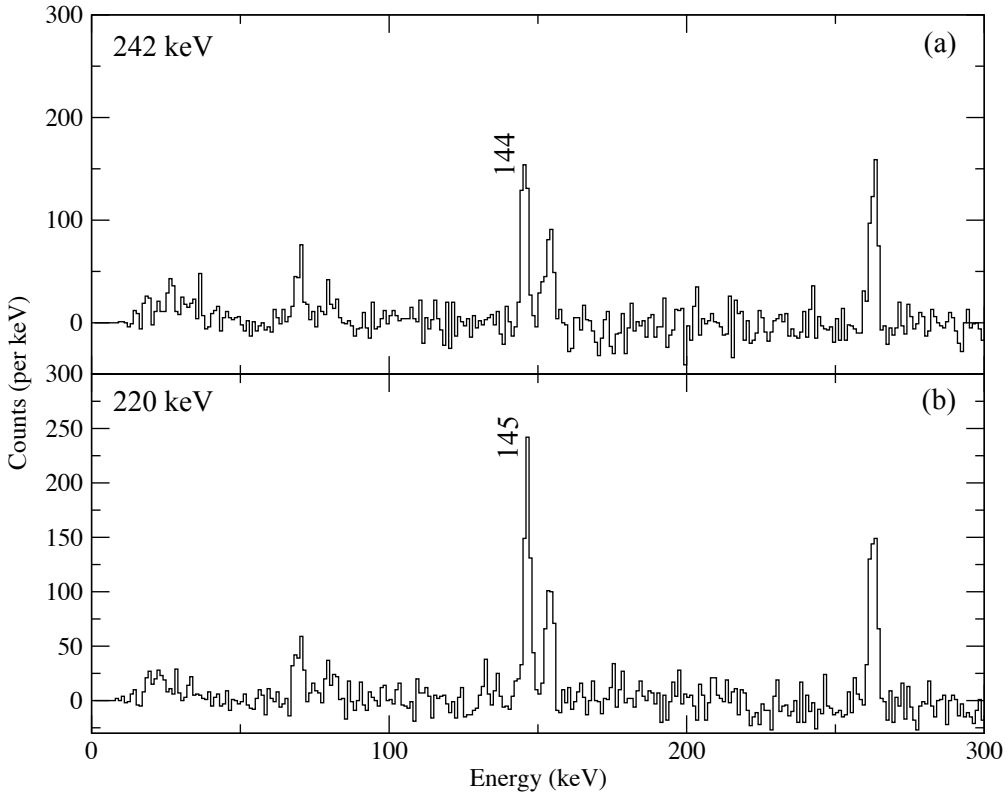

Figure 6.7: γ-ray spectra in coincidence with (a) the 242-keV and (b) the 220-keV transition. There is a subtle shift in energy of the peak at ≈ 144 keV.

and 242-keV γ rays. A closer inspection reveals that the peaks are offset by a channel, which represents a 1 keV difference and suggests that these are two distinct γ rays that feed into the low-spin states of band 2 and band 3.

Peaks at 351 keV and 371 keV can be seen in Figure 6.6. These transitions are not present in the spectra demanded in coincidence with the 220-keV and 242-keV γ rays shown in Figure 6.8 and Figure 6.9, respectively. This suggests that they form parallel decay paths from the $13/2^+$ state of the yrast band. It was suggested in the previous study by Mueller *et al.* that there are two possible scenarios for the placement of the 351-keV and 371-keV γ rays [60]. In the first scenario both γ rays decay out of the yrast band into two different states. In the second scenario these γ rays feed the same state but the 351-

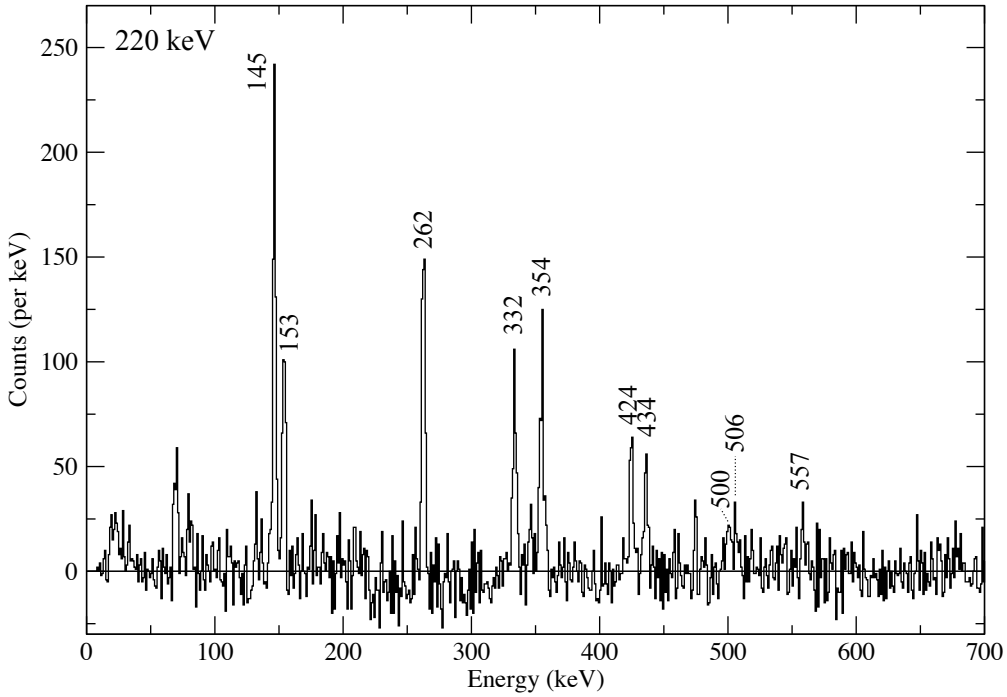

Figure 6.8: Gamma rays in coincidence with the 220-keV transition.

keV γ ray depopulates a state $\approx$ 20 keV below the $13/2^+$ in the yrast band. Mueller *et al.* assumed the latter scenario is preferable based on a comparison with the decay of the neighbouring isotope ^{177}Au, which shows a similar decay out of the yrast band [45].

Figure 6.8 shows a γ-ray spectrum generated by demanding coincidences with the 220-keV transition. The prominent γ rays in band 1 are present in this spectrum with additional γ-ray peaks at 332 keV, 424 keV, 500 keV and 557 keV. These peaks form a band on top of the 220-keV γ ray (band 2), which decays in parallel to the yrast band as seen in figure 6.5. The 145-keV γ ray is a linking transition to band 1.

Figure 6.9 shows γ rays in coincidence with the 242-keV transition, the other component of the 144-keV doublet can be seen. This spectrum shows the yrast transitions (band 1) however, the peaks at 354 keV, 434 keV and 506 keV

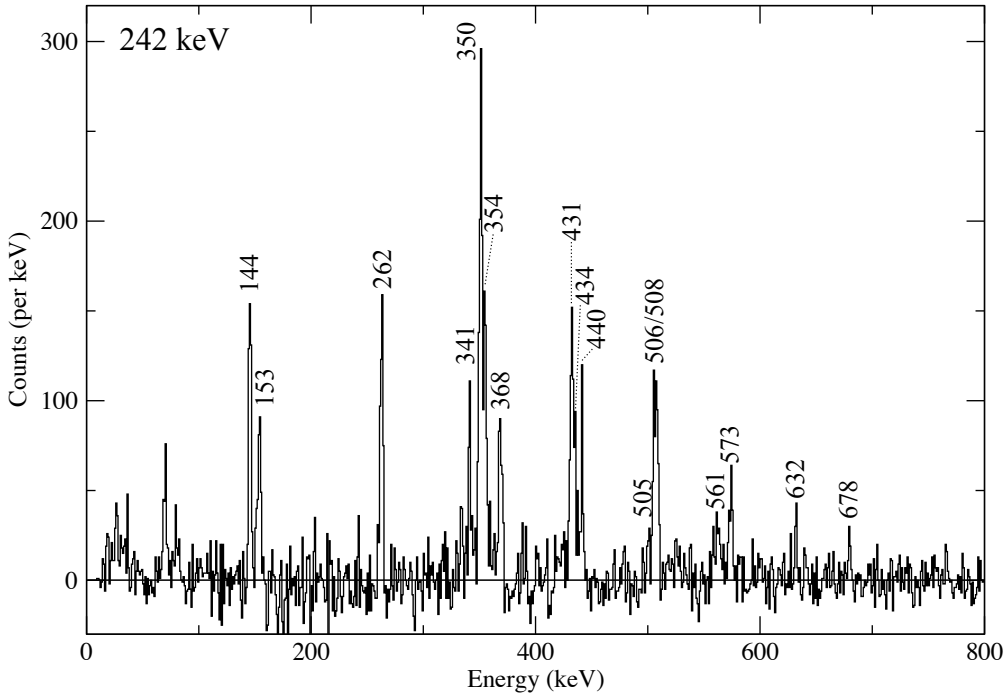

Figure 6.9: γ rays in coincidence with the 242-keV transition.

are broader than observed in previous spectra. An analysis of coincidence spectra reveals a band, band 3, built above the 242-keV transition with each γ ray in the cascade having an energy only a few keV different to the yrast transitions. Figure 6.9 also shows peaks at 341 keV, 368 keV, 440 keV, 508 keV and 561 keV. Figure 6.10 shows γ rays in coincidence with the 286-keV γ ray. The 368-keV, 440-keV, 508-keV and 561-keV γ rays are common to both spectra, while the 341-keV transition is not apparent in Figure 6.10. These transitions are ordered into a cascade labelled band 4 in Figure 6.5. The 286-keV transition is assigned to feed the $9/2^-$ band head directly on the basis of these coincidence spectra while the 341-keV transition feeds the $13/2^-$ state in band 3.

Figure 6.10 indicates that the 192-keV transition is also in coincidence with the 286-keV γ ray. In the previous work of Mueller *et al.* it was proposed that

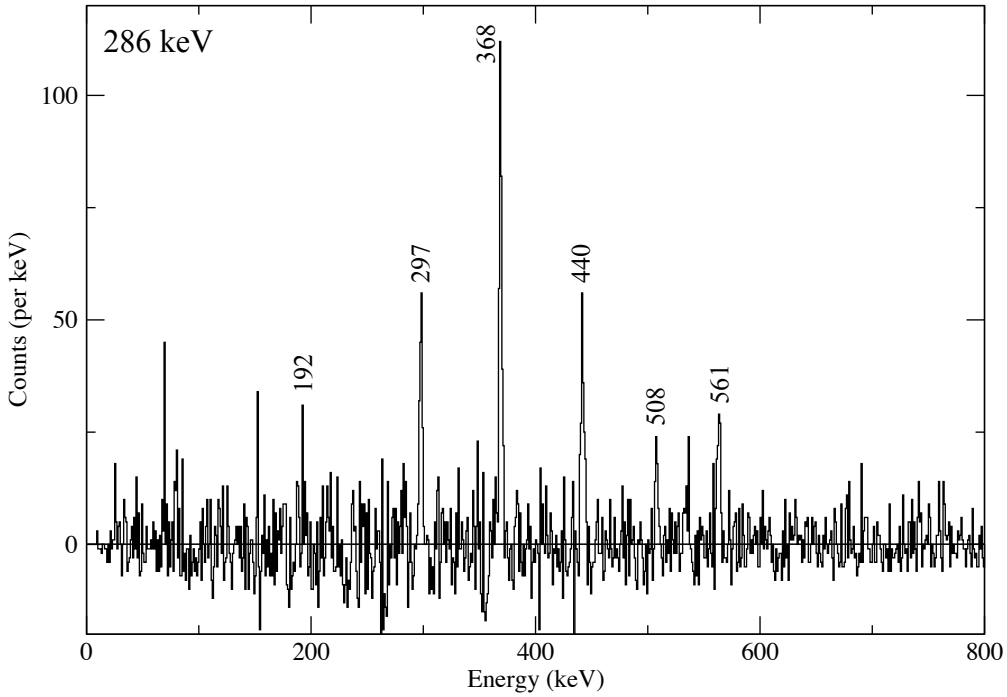

Figure 6.10: γ rays in coincidence with the 286-keV transition.

the 192-keV transition depopulated band 4 [60]. In this work, the 192-keV peak is not seen in coincidence with any of the transitions in band 4. Moreover the 192-keV γ ray itself is only seen to be in coincidence with the 286-keV γ ray. Therefore, the 192-keV γ ray has been placed feeding the state depopulated by the 286-keV transition.

Electron-Gamma Coincidence Analysis

The use of SAGE in this analysis was thoroughly investigated, however too much background combined with a low number of counts meant that the data collected using the SAGE silicon detector was not used in this work. Figure 6.11 shows sample spectra to illustrate why electron-γ coincidences were not examined. Figure 6.11(a) shows the electrons detected using the SAGE silicon detector that are in coincidence with a recoil in the GREAT DSSD detectors. There appears to be a peak at 313 keV. Figure 6.11 shows a spectrum

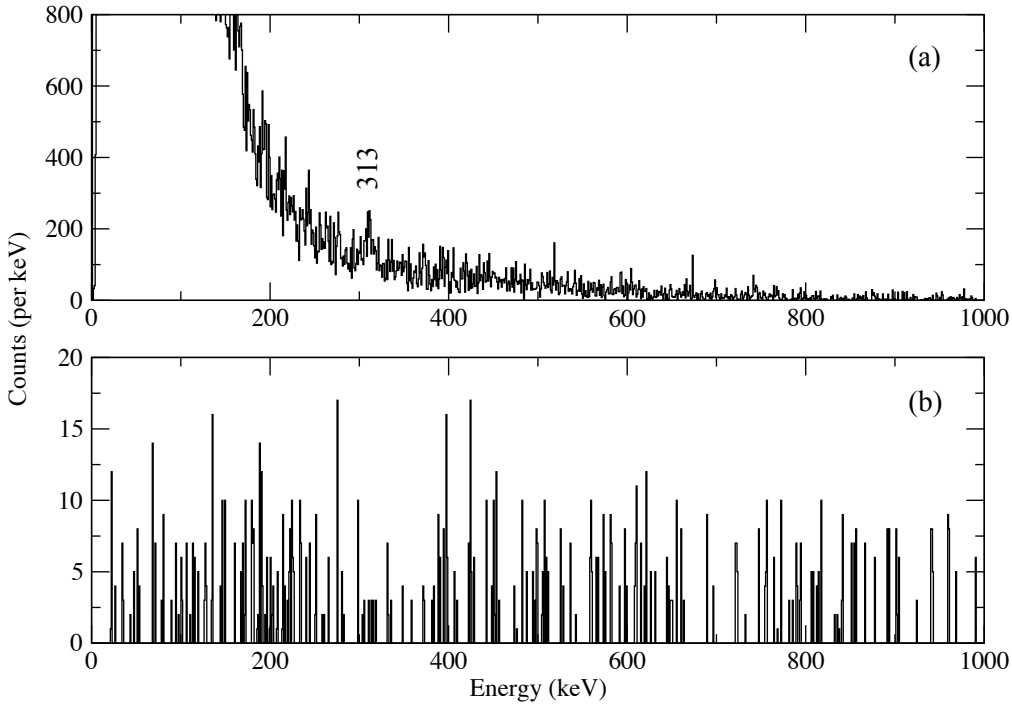

Figure 6.11: Spectra from an electron-γ coincidence matrix using SAGE which are in coincidence with a recoil in the DSSD detectors. (a) shows the full electron projection. (b) shows γ-rays in coincidence with a 313-keV electron.

of γ rays in coincidence with the 313 keV electron that indicates there are very few counts for a useful analysis.

6.3.2 Isomeric States in ^{179}Au

Isomeric states are expected in this region of the nuclear chart and may have lifetimes that are too long to be detected at the target position. The GREAT spectrometer located at the separator focal plane allowed isomer-delayed γ rays to be identified. The flight time through the gas-filled separator RITU is ≈ 0.5 μs so any states with a lifetime greater than this will be observed in the GREAT focal-plane spectrometer. Figure 6.12 shows γ rays detected by the focal-plane Clover detectors that are preceded up to 10 μs by a recoil implantation in the GREAT DSSDs. The spectrum contains some unavoidable contamination

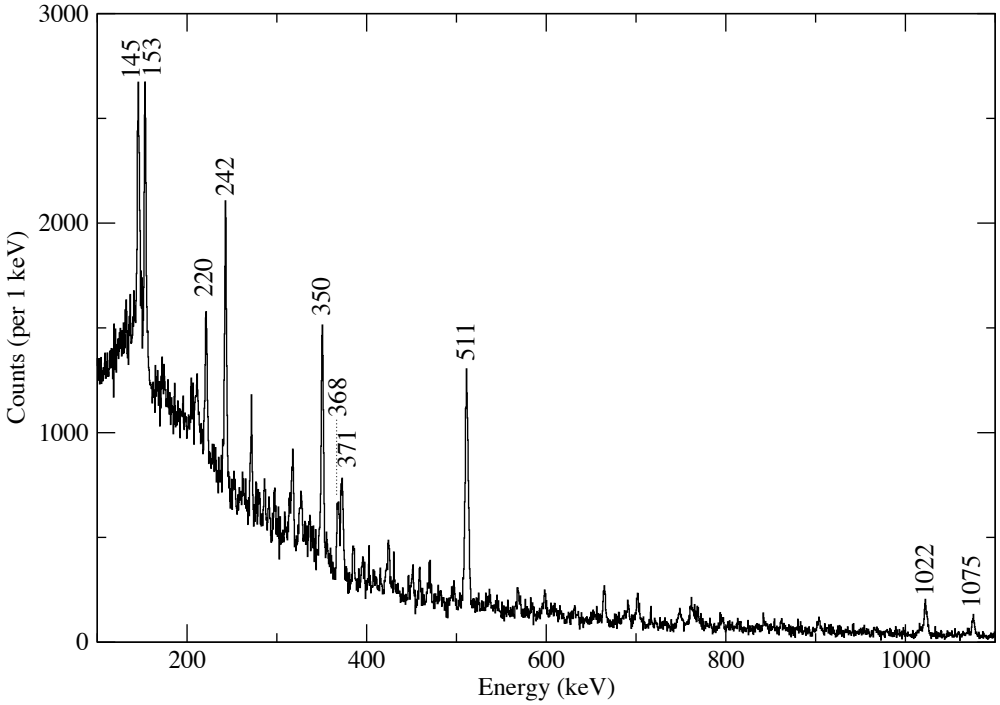

Figure 6.12: Spectrum showing γ rays detected in the GREAT Clover detectors at the separator focal plane. Gamma rays in this spectrum are preceded by recoil implantations in the GREAT DSSDs up to 10μs earlier. The large peak at 511 keV is annihilation radiation from pair production in the surroundings.

since no further correlations were demanded with a characteristic α decay. The labelled γ rays ($E_\gamma < 600$ keV) in Figure 6.12 have already been identified in the RDT analysis of ^{179}Au. However their appearance in the delayed spectra suggests that they have been delayed by the presence of an isomeric state.

In addition to the known ^{179}Au γ rays there are two previously unidentified γ rays at 1022 keV and 1075 keV, which are labelled in Figure 6.12. A recoil-tagged Clover-planar γ-γ matrix was produced to determine the relationship of these high-energy transitions to the low-lying γ-ray transitions in ^{179}Au scheme. Figure 6.13 shows γ-ray coincidence spectra extracted from this matrix. Figure 6.13(a) shows γ rays detected in the GREAT planar detectors that are in coincidence with a 1022-keV γ ray detected in the GREAT Clover detectors. The 242-keV and 350-keV γ-ray transitions in band 3 are

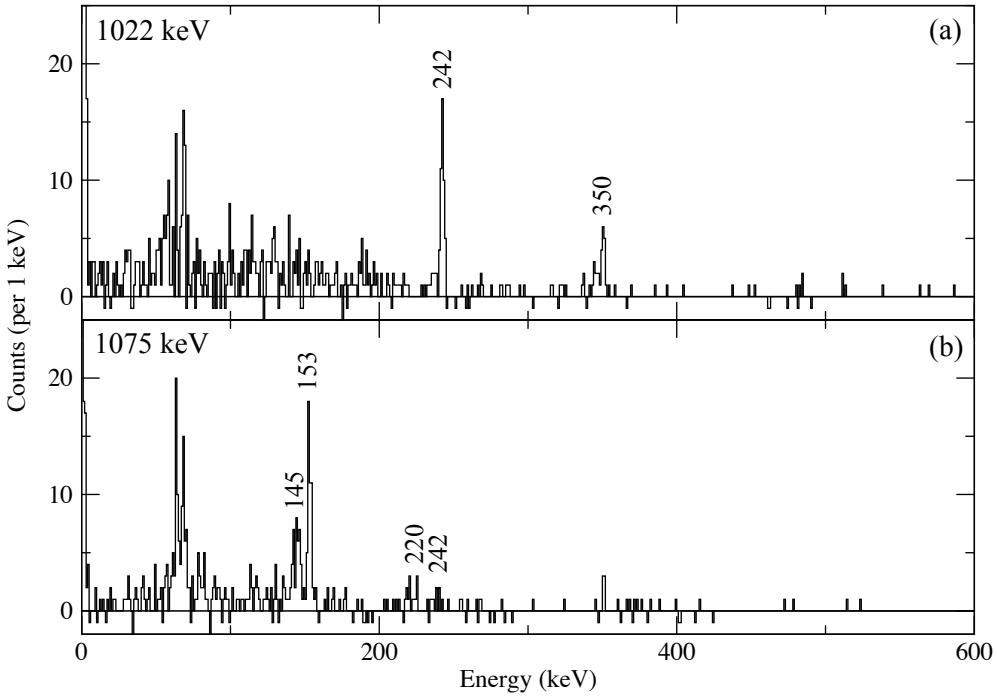

Figure 6.13: Gamma rays detected in the GREAT planar detector and in delayed coincidence with (a) the 1022-keV transition and (b) the 1075-keV transition detected in the GREAT Clover detectors. Gamma rays in this spectrum are preceded by recoil implantations in the GREAT DSSDs up to 10 μs earlier.

clearly seen in the coincidence spectrum. Therefore the 1022-keV transition is assigned to feed the $17/2^-$ level in band 3. Consideration was given to the 1022 keV potentially arising from two 511-keV peaks being summed in code by the add-back technique. This was checked by removing the add-back section of the code and analysing the resulting spectra. The ratio of the 511-keV peak to the 1022-keV peak remained the same indicating that the 1022-keV peak is a genuine γ ray and not an artefact created in the sort code.

Figure 6.13(b) shows γ rays detected in the GREAT planar detectors in coincidence with the 1075-keV transition detected in the GREAT Clover detectors. Coincidences can be seen with γ rays of energies 145 keV, 153 keV, 220 keV and 242 keV. All of the coincident γ rays identified in Figure 6.13 were assigned to ^{179}Au in the previous section using the RDT technique. This

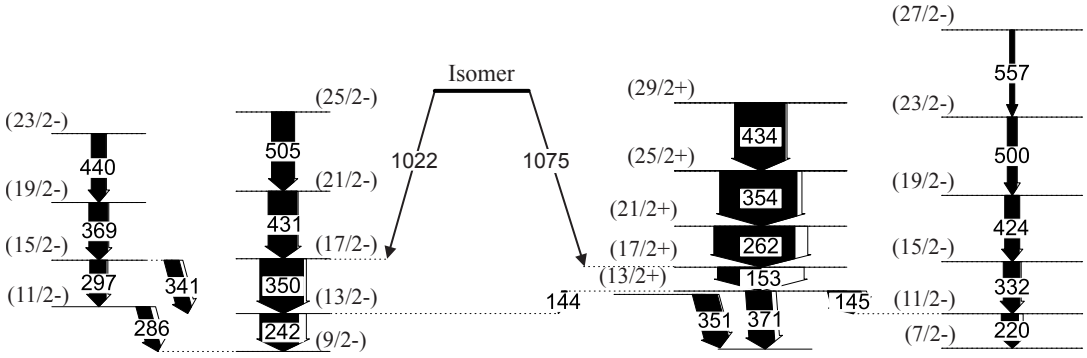

Figure 6.14: A partial level scheme showing the placement of the two new isomer-delayed γ-ray transitions.

indicates that the 1022-keV and 1075-keV γ rays originate from ^{179}Au and gives a clear indication where they feed into the established level scheme. The placement of these γ rays can be seen in Figure 6.14.

The half-life of the isomer was measured using the time differences between recoil implantations in the DSSDs and detection of the isomer-delayed γ rays in the focal-plane Clover detectors. The decay curves extracted for each transition can be seen in Figure 6.15. These figures show exponential decays with a background component arising from false correlations between recoils and γ rays. The decay curves were fitted by two exponential functions summed together; one to fit the half-life of the background and another to fit the decay of the isomer. The fitting method revealed the 1022-keV and 1075-keV isomers have half lives 250(20) ns and 290(40) ns respectively. This yields an error-weighted mean half-life of $t_{1/2}$=262(20) ns.

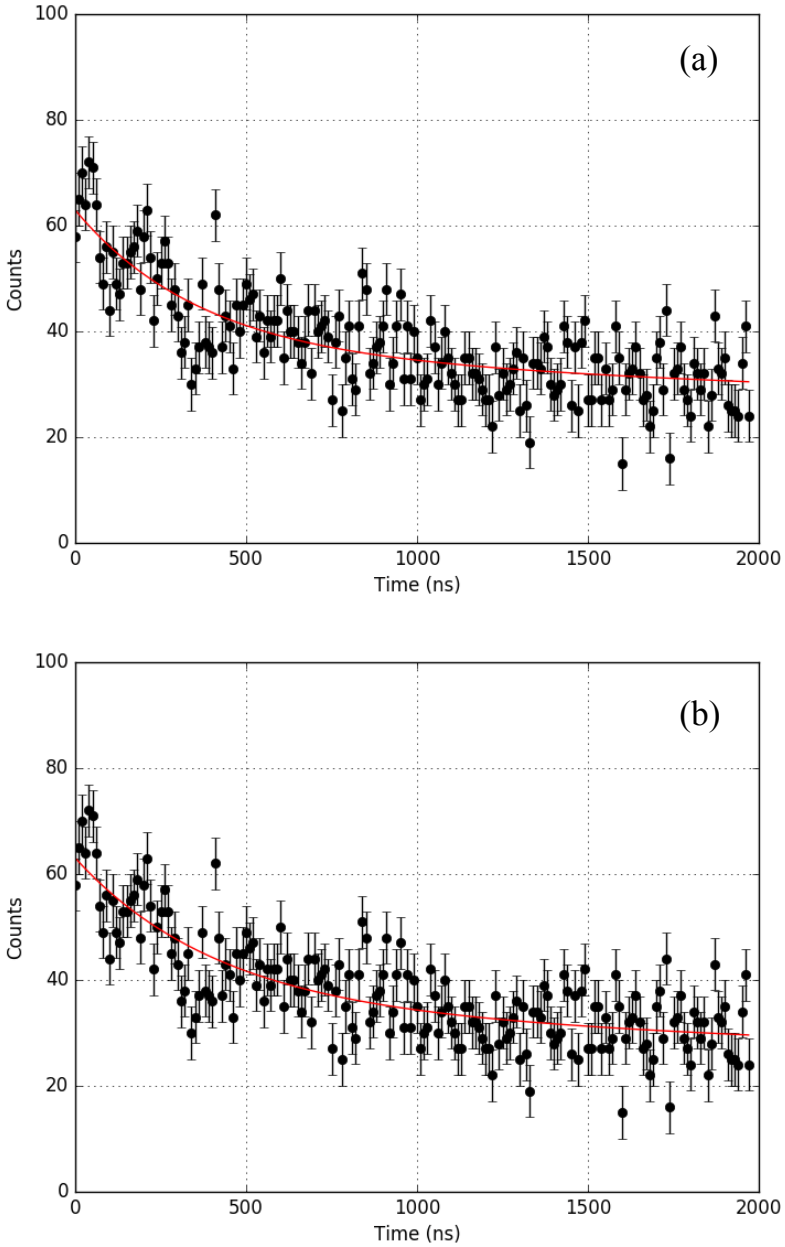

Figure 6.15: The time difference between a recoil implantation in the DSSDs and the detection of (a) the 1022-keV isomer and (b) the 1075-keV isomer. The isomer-delayed γ rays were detected in the GREAT Clover detectors.

6.4 Discussion

6.4.1 The Intruder Configurations

The neutron-deficient nucleus ^{179}Au has an unpaired proton that can be excited across the $Z = 82$ shell gap to form $1p$-$4h$ intruder excitations. The configuration assignments made for this nucleus by Mueller *et al.* have been discussed in section 6.1. This work employed the RDT method to assign unambiguously ≈ 30 γ rays to ^{179}Au resulting in minor revisions of the level scheme published by Mueller *et al.*[60]. Mueller *et al.* interpreted band 1 to be the $\pi i_{13/2}$ intruder band based on comparisons with yrast sequences in other odd-Au isotopes [45][54][61][70]. In those nuclei the $13/2^+$ state is observed to be the oblate band head which decays into coexisting $\pi h_{9/2}$ and $\pi f_{7/2}$ intruder configurations. Bands 2 and 4 were interpreted as mixed configurations of the unfavoured $\pi h_{9/2}$ and favoured $\pi f_{7/2}$ orbitals.

6.4.2 The $t_{1/2}$=262(20) ns Isomer

In addition to the γ rays detected at the target position, two new γ rays associated with ^{179}Au have been identified using the GREAT focal-plane spectrometer. These γ rays have energies of 1022 keV and 1075 keV. It is presumed that both γ rays form decay paths from the same isomeric state on the basis of transition energy sums and the similarities of the measured half-lives within experimental uncertainties.

The likely multipolarities for each transition has been estimated using the Weisskopf estimates for the half-lives defined in section 2.4.1. The half-life estimates for different multipolarities at the 1022-keV and 1075-keV transitions are listed in Table 6.1 and Table 6.2, respectively. The closest values to those measured indicate that both the 1022-keV and the 1075-keV γ rays are likely

L	T_{EL} (s)	T_{ML} (s)
1	1.98×10^{-15}	2.10×10^{-14}
2	8.48×10^{-6}	8.81×10^{-10}
3	5.31×10^{-7}	5.62×10^{-5}
4	5.09×10^{-10}	5.39
5	6.89×10^{3}	7.29×10^{5}

Table 6.1: Weisskopf estimates for the half-lives of the 1022-keV γ ray. T_{EL} and T_{ML} are the half-lives of electric and magnetic transitions with different multipolarities, respectively. Half lives are presented in units of s.

L	T_{EL}(s)	T_{ML}(s)
1	1.71×10^{-15}	1.80×10^{-14}
2	6.58×10^{-6}	6.84×10^{-10}
3	3.72×10^{-7}	3.94×10^{-5}
4	3.23×10^{-10}	3.42
5	3.95×10^{3}	4.18×10^{5}

Table 6.2: Weisskopf estimates for the half-lives of the 1075-keV γ ray. T_{EL} and T_{ML} are the half-lives of electric and magnetic transitions with different multipolarities, respectively. Half lives are presented in units of s.

to have E3 multipolarity. The assignment of E3 multipolarity to both the 1022-keV and 1075-keV γ rays is problematic if both γ rays originate from the same state since the coincidence analysis indicates that they feed states with different parity. This could imply that some of the spin and parity assignments in the level scheme of ^{179}Au discovered by Mueller *et al.* are incorrect. This is deemed to be unlikely since the band structures fit in with the systematic trends expected for the Au isotopes.

In an alternative scenario, the 1022-keV and the 1075-keV γ rays could de-excite different isomers at the same excitation energy. The measured half-lives have large errors which reflects the difficulty in fitting an exponential decay to a spectrum with few counts and a relatively high background. Therefore, the possibility of two different isomers with an accidental degeneracy cannot be excluded with these data.

Isomers with a spin-parity assignment of $31/2^-$ have been identified in ^{189}Au, ^{191}Au and ^{193}Au [71][72][73]. If the γ rays detected in this work decay from the $31/2^-$ state then the transitions would be $31/2^- \rightarrow 17/2^+$ or $31/2^- \rightarrow 17/2^-$. According to γ decay selection rules, neither of these transitions are allowed to proceed via an E3 transition. Therefore, the $31/2^-$ state has been ruled out as a candidate for the isomer.

Isomers with spin and parity $21/2^+$ have been observed in ^{191}Au, ^{193}Au, ^{195}Au and ^{197}Au [73][72][74]. A transition from $21/2^+ \rightarrow 17/2^+$ would be allowed to proceed via an E2 γ ray and a transition between $21/2^+ \rightarrow 17/2^-$ would be allowed to decay via an E3 γ ray. Therefore the $21/2^+$ is a candidate for the isomeric state from which the two new γ rays decay (assuming the Weisskopf estimates for the half lives are reliable). If both the 1022-keV and the 1075-keV γ rays decay from the $21/2^+$ state it would be unlikely for one decay to be parity changing and one to be parity conserving. If it is the case that both γ rays are either parity changing or conserving, then the spins and parities of the levels they feed into, as reported by Mueller *et al.*, must be incorrect.

The half-lives measured in this work have large errors arising from the low statistics available and the presence of a relatively high background. RDT was not used to analyse the data obtained from the focal plane detectors as the count rate was low, therefore recoil-tagging was the only option, which led to contamination in the spectra. For this reason the Weisskopf estimates for the half lives and thus the constraints on the multipolarities of the decays must be considered critically. There is also the possibility that the two γ rays decay from two different states which form an accidental degeneracy. It is not possible to say which scenario is correct with the information available, however there is certainly room for further work to identify the origin of these two γ rays.

Chapter 7

Summary

This work reports the analysis of two experiments that took place at the University of Jyväskylä Accelerator Laboratory. The experiments made use of large germanium detector arrays coupled with the RITU gas-filled separator and the GREAT focal-plane spectrometer. This set-up allowed recoil-decay tagging (RDT) to be employed allowing for a very high degree of selectivity. Given that both experiments involved arrays of germanium detectors situated at varying angles with respect to the target position, attempts were made at measuring the angular distributions of the detected γ rays. However the number of counts in both experiments was insufficient and angular distribution measurements have not been completed at this time.

Careful γ-γ coincidence analysis revealed several new collective structures in the proton-unbound nucleus ^{175}Au. These have been interpreted as structures built upon excitations of the unpaired proton in ^{175}Au across the Z = 82 shell gap. In addition to the previously known $\pi i_{13/2}$ intruder configuration, structures built on $\pi h_{9/2}$ and $\pi f_{7/2}$ have been identified. Excited states arising from the $\pi h_{11/2}$ proton hole coupled to the ^{176}Hg core have been identified by comparison with a similar structure in nearby ^{177}Au. For the first time γ rays

that are thought to feed the ground-state band of ^{175}Au have been observed via mother-daughter α correlations with the ground-state α decay of ^{171}Ir.

The neutron-deficient isotope ^{179}Au was also examined using RDT analysis to build up a level scheme of four collective bands. The bands have been assigned to being based on $\pi i_{13/2}$, $\pi h_{9/2}$ and $\pi f_{7/2} \otimes h_{9/2}$ intruder orbitals. This work confirms an earlier study by Mueller *et al.* Additionally two new γ rays at 1022 keV and 1075 keV have been identified decaying from isomeric states. The half lives of the states from which the 1022-keV and 1075-keV γ rays decay have been measured to be 250$\pm$20 ns and 290$\pm$40 ns. The information available has prevented a firm multipolarity assignment for these γ rays however their existence may call previous spin assignments in the previously assigned $\pi i_{13/2}$ and $\pi h_{9/2}$ band structures into question.

This work adds to the information known about nuclei exhibiting shape coexistence. This is useful because, as mentioned in the introduction to this work, shape coexistence is thought to arise from the excitation of valence nucleon being excited into vacant orbitals, thereby driving the nucleus into a deformed shape. Nuclear physics experiments such as those described here allow observation of the nuclear structure arising from these deformed configurations. These measurements in conjunction with knowledge of the smoothly varying systematics across isotopic chains elucidates the evolution of the underlying valence nucleon excitations as a function of neutron number. This, in turn, augments the known nuclear structure information and provides constraints on nuclear structure theories.

Bibliography

[1] J. Bonn, G. Huber, H.-J. Kluge, L. Kugler, and E. Otten, Phys. Lett. B. **38**, 308 (1972).

[2] K. Heyde and J. L. Wood, Rev. Mod. Phys. **83**, 1467 (2011).

[3] N. Bree *et al.*, Phys. Rev. Lett. **112**, 162701 (2014).

[4] K. Heyde, *Basic Ideas and Concepts in Nuclear Physics* (Institute of Physics Publishing, 2004).

[5] C. Weizsäcker, Z. Phys. **96**, 431 (1935).

[6] H. Bethe and R. Bacher, Rev. Mod. Phys. **8**, 82 (1936).

[7] K. Krane, *Introductory Nuclear Physics* (John Wiley and Sons, Inc., 1988).

[8] W. Burcham, *Elements of Nuclear Physics* (Longman Inc., 1979).

[9] M. Mayer, Phys. Rev. **74**, 235 (1948).

[10] O. Haxel, J. Hans, D. Jensen, and H. Suess, Phys. Rev. **75**, 1766 (1949).

[11] R. Woods and D. Saxon, Phys. Rev. **95**, 577 (1954).

[12] Z. Szymanski, *Fast Nuclear Rotations* (Clarendon Press, 1983).

[13] S. Nilsson, Kgl. Danske. Videnskab. Selskab, Mat-fys. Medd. **29**, 16 (1954).

[14] G. Dracoulis *et al.*, Phys. Rev. C. **69**, 054318 (2004).

[15] A. Andreyev *et al.*, Nature **405**, 430 (2000).

[16] P. Davidson *et al.*, Nucl. Phys. A **657**, 219 (1999).

[17] P. Davidson *et al.*, Nucl. Phys. A **568**, 90 (1994).

[18] T. Kibédi, G. Dracoulis, A. Byrne, and P. Davidson, Nucl. Phys. A **567**, 183 (1994).

[19] V. Weisskopf, Phys. Rev. **83**, 1073 (1951).

[20] A. Wapstra, *Nuclear Spectroscopy Tables* (Amsterdam, 1959).

[21] G. F. Knoll, *Radiation Detection and Measurement, Third Edition* (John Wiley and Sons, Inc., 1999).

[22] K. Heyde and R. A. Meyer, Phys. Rev. C. **37**, 2170 (1988).

[23] G. Gamow, Z. Phys. **204** (1928).

[24] R. W. Gurney and E. U. Condon, Nature **122**, 439 (1928).

[25] C. Beausang and J. Simpson, J. Phys. G: Nucl. Part. Phys **22**, 527 (1996).

[26] P. Greenlees *et al.*, AIP Conf. Proc. **764**, 237 (2005).

[27] P. Nolan, F. Beck, and D. Fossan, Annu. Rev. Nucl. Part. Sci. **45**, 561 (1994).

[28] J. Pakarinen *et al.*, Eur. Phys. J. A **50**, 53 (2014).

[29] J. Sorri *et al.*, Nucl. Inst. Meth. Phys. Res. A **812**, 24 (2016).

[30] P. Papadakis *et al.*, Jour. Phys.: Conf. Ser. **312** (2010).

[31] C. Beausang *et al.*, Nucl. Inst. Meth. Phys. Res. A **313**, 37 (1992).

[32] S. Shepherd *et al.*, Nucl. Inst. Meth. Phys. Res. A **434**, 373 (1999).

[33] M. Leino *et al.*, Nucl. Inst. Meth. Phys. Res. B **99**, 653 (1995).

[34] P. Papadakis, PhD thesis, University of Liverpool.

[35] R. Page *et al.*, Nucl. Inst. Meth. Phys. Res. B **204**, 634 (2003).

[36] A. Andreyev *et al.*, Nucl. Inst. Meth. Phys. Res. A **533**, 422 (2004).

[37] I. Lazarus *et al.*, IEEE Transactions on Nuclear Science **48** (2001).

[38] P. Rahkila, Nucl. Inst. Meth. Phys. Res. A **595**, 637 (2008).

[39] W. Trzaska, Nucl. Inst. Meth. Phys. Res. A **297**, 223 (1990).

[40] D. Radford, Nucl. Inst. Meth. Phys. Res. A **361**, 297 (1995).

[41] Y. Khazov and A. Rodionov, Nuclear Data Sheets **112**, 855 (2011).

[42] T. Kibédi, T. Burrows, M. Trzhaskovskaya, P. Davidson, and C. N. Jr., Nucl. Inst. and Meth. A **589**, 202 (2008).

[43] E. Paul *et al.*, Phys. Rev. C. **51**, 78 (1995).

[44] M. Venhart *et al.*, Phys. Lett. B **695**, 82 (2011).

[45] F. Kondev *et al.*, Phys. Lett. B **512**, 268 (2001).

[46] T. Grahn *et al.*, J. Phys.: Conf. Ser. **420**, 012047 (2013).

[47] D. J. Rowe and J. L. Wood, *Fundamentals of Nuclear Models: Foundational Models* (World Scientific, 2010).

[48] C. Cabot *et al.*, Nucl. Phys. A **241**, 341 (1975).

[49] G. D. Dracoulis *et al.*, Phys. G: Nucl. Phys. **12**, L97 (1986).

[50] H. Watkins *et al.*, Phys. Rev. C. **84**, 051302 (2011).

[51] A. N. Andreyev *et al.*, Phys. Rev. C. **87**, 054311 (2013).

[52] R. D. Page, Phys. Rev. C. **83**, 014305 (2011).

[53] C. Davids *et al.*, Phys. Rev. C **55**, 2255 (1997).

[54] A. Larabee *et al.*, Phys. Lett. B **169**, 21 (1986).

[55] M. Venhart *et al.*, Phys. Rev. C. **95**, 061302(R) (2017).

[56] F. A. Ali, *Shape coexistence in the proton-unbound nucleus* ^{177}Au. (University of Liverpool, 2014).

[57] J. Yao, M. Bender, and P.-H. Heenan, Phys. Rev. C. **87**, 034322 (2013).

[58] R. B. Firestone, *Table of Isotopes* (Wiley, 1997).

[59] A. Andreyev, Private communication, 2016.

[60] W. Mueller *et al.*, Phys. Rev. C **69** (2004).

[61] W. Mueller *et al.*, Phys. Rev. C. **59**, 2009 (1999).

[62] B. Cederwall *et al.*, Physics Letters B **443**, 69 (1998).

[63] G. D. Dracoulis, Phys. Rev. C **49**, 3324 (1994).

[64] G. D. Dracoulis *et al.*, Phys. Rev. C **44**, R1246 (1991).

[65] T. Grahn *et al.*, Phys. Rev. Lett. **97**, 062501 (2006).

[66] T. Grahn *et al.*, Nuclear Physics A **801**, 83 (2008).

[67] M. Scheck *et al.*, Phys. Rev. C **81**, 014310 (2010).

[68] E. Gueorguieva *et al.*, Phys. Rev. C **68**, 054308 (2003).

[69] A. Siivola, Nucl. Phys. A. **109**, 231 (1968).

[70] J. K. Johansson *et al.*, Phys. Rev. C. **40**, 132 (1989).

[71] N. Perrin *et al.*, Z. Phys. A **359**, 373 (1997).

[72] G. D. Dracoulis *et al.*, Phys. Rev. C. **87**, 014326 (2013).

[73] Y. Gono, R. M. Lieder, M. Müller-Veggian, A. Neskakis, and C. Mayer-Böricke, Nucl. Phys. A **327**, 269 (1979).

[74] C. Wheldon *et al.*, Phys. Rev. C. **74**, 027303 (2006).